國 立 交 通 大 學
電信工程學系
博 士 論 文

單晶互補式金屬導線傳輸線
CMOS 主動濾波器設計

**Complementary-Conducting-Strips
Transmission Line CMOS Active Filter Design**

研 究 生：吳憲宏 (Hsien-Hung Wu)

指導教授：莊晴光 博士 (Dr. Ching-Kuang C. Tzuang)

中 華 民 國 九 十 五 年 七 月

單晶互補式金金屬導線傳輸線
CMOS 主動濾波器設計
Complementary-Conducting-Strips
Transmission Line CMOS Active Filter Design

研 究 生：吳憲宏   Student: Hsien-Hung Wu

指導教授：莊晴光 博士   Advisor: Dr. Ching-Kuang C. Tzuang

國 立 交 通 大 學

電信工程研究所

博 士 論 文

A Dissertation
Submitted to Institute of Communication Engineering
College of Engineering
National Chiao Tung University
In Partial Fulfillment of the Requirements
for the Degree of
Doctor of Philosophy
in
Communication Engineering
July 2006
Hsinchu, Taiwan, Republic of China

中 華 民 國 九 十 五 年 七 月

推 薦 函

一、事由：本校電信研究所博士班研究生 吳憲宏 提出論文以參加國立交通大學

　　博士班論文口試。

二、說明：本校電信研究所博士班研究生 吳憲宏 已完成本校電信研究所規定之

　　學科課程及論文研究之訓練。

　　有關學科部分，吳君已修滿十八學分之規定（請查閱學籍資料）並通過資格

　　考試。

　　有關論文部分，吳君已完成其論文初稿，相關之論文亦分別發表或即將發表

　　於國際期刊（請查閱附件）並滿足論文計點之要求。

　　總而言之，吳君已具備國立交通大學電信研究所應有之教育及訓練水準，因

　　此特推薦

　　吳君參加國立交通大學電信工程學系博士班論文口試。

交通大學電信工程學系教授

莊晴光

國 立 交 通 大 學

論 文 口 試 委 員 審 定 書

本校＿＿＿＿電 信 工 程＿＿＿＿學系博士班＿＿＿＿吳 憲 宏＿＿＿＿君

所提論文＿＿＿＿單晶互補式金屬導線傳輸線 CMOS 主動濾波器設計＿＿＿＿
＿＿＿＿Complementary-Conducting-Strips Transmission Line CMOS＿＿＿＿
＿＿＿＿Active Filer Design＿＿＿＿

合於博士資格水準、業經本委員會評審認可。

口試委員：＿＿＿＿＿＿＿＿＿＿＿　＿＿＿＿＿＿＿＿＿＿＿

指導教授：＿＿＿＿＿＿＿＿＿＿＿　＿＿＿＿＿＿＿＿＿＿＿

系 主 任：＿＿＿＿＿＿＿＿教授

中 華 民 國 九 十 五 年 七 月 二 十 七 日

Department of Communication Engineering
National Chiao Tung University
Hsinchu, Taiwan, R.O.C.

Date: July 27, 2006

We have carefully read the dissertation entitled

Complementary-Conducting-Strips Transmission Line

CMOS Active Filter Design

submitted by   Hsien-Hung Wu   in partial
fulfillment of the requirements of the degree of DOCTOR OF
PHILOSOPHY and recommend its acceptance.

Thesis Advisor: _____

Chairman

Department of Communication Engineering: _____

國 立 交 通 大 學

博碩士論文全文電子檔著作權授權書

（提供授權人裝訂於紙本論文書名頁之次頁用）

本授權書所授權之學位論文，為本人於國立交通大學電信工程系所
___電波___組， 94 學年度第_二_學期取得博士學位之論文。

論文題目：單晶互補式金屬導線傳輸線CMOS主動濾波器設計
指導教授：莊晴光

■ 同意

本人茲將本著作，以非專屬、無償授權國立交通大學與台灣聯合大學系統圖書館：基於推動讀者間「資源共享、互惠合作」之理念，與回饋社會與學術研究之目的，國立交通大學及台灣聯合大學系統圖書館得不限地域、時間與次數，以紙本、光碟或數位化等各種方法收錄、重製與利用；於著作權法合理使用範圍內，讀者得進行線上檢索、閱覽、下載或列印。

論文全文上載網路公開之範圍及時間：

本校及台灣聯合大學系統區域網路	■ 中華民國 96 年 8 月 28 日公開
校外網際網路	■ 中華民國 96 年 8 月 28 日公開

■ 全文電子檔送交國家圖書館

授 權 人：吳憲宏

親筆簽名：___吳憲宏___

中華民國　95 年　8 月　28 日

國 立 交 通 大 學

博碩士紙本論文著作權授權書

（提供授權人裝訂於全文電子檔授權書之次頁用）

本授權書所授權之學位論文，為本人於國立交通大學電信工程系所
___電波___組， 94 學年度第_二_學期取得博士學位之論文。

論文題目：單晶互補式金屬導線傳輸線CMOS主動濾波器設計
指導教授：莊晴光

■ 同意

本人茲將本著作，以非專屬、無償授權國立交通大學，基於推動讀者間「資源共享、互惠合作」之理念，與回饋社會與學術研究之目的，國立交通大學圖書館得以紙本收錄、重製與利用；於著作權法合理使用範圍內，讀者得進行閱覽或列印。

本論文為本人向經濟部智慧局申請專利(未申請者本條款請不予理會)的附件之一，申請文號為：_____，請將論文延至____年____月____日再公開。

授 權 人：吳憲宏

親筆簽名：___吳憲宏___

中華民國　95 年　8　月 28　日

國家圖書館
博碩士論文電子檔案上網授權書

（提供授權人裝訂於紙本論文本校授權書之後）

ID:GT009213808

本授權書所授權之論文為授權人在國立交通大學電信工程系所 94 學年度第　之　學期取得博士學位之論文。

論文題目：單晶互補式金屬導線傳輸線CMOS主動濾波器設計
指導教授：莊晴光

茲同意將授權人擁有著作權之上列論文全文（含摘要），非專屬、無償授權國家圖書館，不限地域、時間與次數，以微縮、光碟或其他各種數位化方式將上列論文重製，並得將數位化之上列論文及論文電子檔以上載網路方式，提供讀者基於個人非營利性質之線上檢索、閱覽、下載或列印。

※ 讀者基於非營利性質之線上檢索、閱覽、下載或列印上列論文，應依著作權法相關規定辦理。

授權人：吳憲宏

親筆簽名：＿＿吳憲宏＿＿＿＿

民國 95 年 8 月 28 日

單晶互補式金屬導線傳輸線 CMOS 主動濾波器設計

研究生 : 吳憲宏　　　　　　　　　　指導教授 : 莊晴光 博士

國立交通大學　電信工程學系

摘要

本篇論文係研究互補式金屬導線傳輸線 (complementary conducting strips transmission line) 在標準 0.18 μm CMOS 製程，實現單晶片 (monolithic) 主動濾波器的兩種新穎設計方法。第一種方法係利用負阻抗電路以分散補償的方式，改善互補式金屬導線傳輸線的傳播損耗 (propagation loss)。合成出的主動傳輸線在 1 GHz 至 5.5 GHz 頻段內展現出無損耗的特性，並且增加了傳輸線的慢波因子 (slow wave factor)。利用該主動傳輸線所設計出的 5.5 GHz 二階帶通濾波器，雖然在 10.1 MHz 產生了不穩定的情況，但反應出從架構層次設計損耗補償(loss compensation)的重要性。

第二種方法係利用品質因子提昇後的半波長互補式金屬導線傳輸線共震器 (resonator)，實現一個 C 頻段的主動濾波器。共震器的損耗補償只作用於主動濾波器的導通頻段內，並且介入損失 (insertion loss) 的調整並不影響到主動濾波器的中心頻率與 3-dB 頻寬。量測的結果顯示主動濾波器的中心頻率為 6.02 GHz，3-dB 頻寬為 1.14 GHz。當主動濾波器的介入損失與增益分別為 2.2 dB 與 0.56 dB 時，所消耗的功率分別為 5.4 mW 與 7.2 mW，均沒有震盪的情況發生。而對應 2.2-dB 介入損失時的雜訊指數與輸入端 1-dB 功率壓縮點，則分別為 11.4 dB 與 -15.2 dBm。該主動濾波器所需的電路面積為 1230 μm × 880 μm，趨近於同頻段內使用總集電感、電容元件之主動濾波器的電路面積。

Complementary-Conducting-Strips Transmission Line CMOS Active Filter Design

Student : **Hsien-Hung Wu**   Advisor : **Dr. Ching-Kuang C. Tzuang**

Institute of Communication Engineering
National Chiao Tung University

ABSTRACT

This dissertation presents two innovating design approaches of the monolithic active bandpass filter employing complementary-conducting-strips transmission lines (CCS TLs) in the standard 0.18 μm CMOS technology. The first approach utilizes the negative resistance circuit to distributed compensate the propagation loss within the passive CCS TL and successfully produce a loss-free active CCS TL from 1 GHz to 5.5 GHz with an enhanced slow wave property. Though the realized 5.5 GHz second-order active CCS TL bandpass filter had instability problem around 10.1 MHz, but reflected the fact that the loss compensation within an active filter need to be adequately designed in view of the architecture.

The second approach adopts the Q-enhanced half-wavelength CCS TL resonators for a C-Band second-order active bandpass filter design. The loss compensation is only activated at the filter's passband, and the insertion loss could be adjusted without affecting the filter's center frequency and 3-dB bandwidth. Measured results indicate that the filter's center frequency was 6.02 GHz with a 3-dB bandwidth of 1.14 GHz and this filter was free from oscillations with either a 2.2-dB insertion loss or 0.56-dB transmission gain. The corresponding power consumptions were 5.4 mW and 7.2 mW. Also a modest 11.4-dB noise figure and a modest -15.2-dBm input 1-dB compression point were measured when the insertion loss was 2.2 dB. The required chip area was 1230 μm × 880 μm which is comparable to those of monolithic active bandpass filters based on lump inductive and capacitive elements at C-Band.

誌　　謝

　　博士班的求學過程是一段充滿、挑戰、考驗、與驚喜的成長過程。所遭遇的每一個艱難絕非偶然，而每一個階段的成長也絕非僥倖。在此要特別感謝曾經責難過以及鼓勵過我的師長以及朋友。讓我清楚了解到，開始為別人而活的時候，才開使過有意義的日子。在面對壓力與挑戰的時候，不要被擊倒、壓垮，而要用冷靜清晰的思維來面對。

　　一併要感謝在這一千多個日子，曾經授課的師長，與陪我一同修課與考試的同學。在碩士班畢業四年之後，重溫學校生活，倍感溫馨，回味無窮。最讓我難以忘記的是在工程四館917實驗室的日子，雖然是兩年半多的驚鴻一瞥，但是那裡的人與事、一景一物都是我最珍貴的記憶，也是我引以為豪的經歷。特別感謝曾經在知識上有過切磋，與生活上互相照應的學長們。志強學長溫文的處事態度、毓喬學長細膩的行事風格、憲順學長樂於助人與人分享的胸懷、繼禾學長對於生活的關懷、勁融豁達的人生觀；而憲順與繼禾不僅給予我求學上的指引，更是研究過程上的好夥伴。雖然我們都來自不同的領域，有過不同的經歷，但我們共同的是對微波知識的熱情與深受老師的教誨與薰陶。此外惠玲、郁萍、玉琇、蘭雅、涵秦、美靜、與貞黛助理，對於求學過程中大小事情的叮嚀與、協助、與安排，也一併致上我的謝意。而在畢業準備工作上，郁萍與玉琇助理的義務幫忙，這一段過程讓我難以忘懷。

　　最後要感謝的是指導教授莊晴光博士、師母楊靜蘭女士、楊晃瑞教授、以及我親愛的家人。感謝他們永恆不變的關愛，是我最大的支持與動力的來源。另外工作上的長官吳文慶先生、張永嘉先生、與張敏敏女士，感謝他們在人生經驗與工作態度的分享，使我體驗到更多求學的樂趣。

　　一段詩句很適合描述過去的自己，

　　　　『落魄江湖載酒行　楚腰纖細掌中輕
　　　　　十年一覺揚州夢　贏得青慶薄倖名』　　杜牧　遣懷

接下來希望能如長風萬里般地行走出一片新的天地。

謝謝

<div align="right">
關門弟子
憲宏　于新竹交大
</div>

TABLE OF CONTENTS

LIST OF TABLES

LIST OF FIGURES

CHAPTER 1

Introduction

1.1 Background

Wireless building blocks including antenna, filter, baluns, and other devices are mostly in discrete forms or embedded into the SIP [1-6]. A complete solution for making a wireless device with a very small form factor is becoming a reality by combining advanced techniques of system-on-chip in CMOS technology owing to its low cost manufacturing and high volume integrating capabilities. Elimination of off-chip filters often means adding RF performance, improving selectivity requirements, reducing noise pick-up, and lowering overall RF power consumption [7-8]. Taking the conventional super-heterodyne receiver for an example, it is robust for avoiding DC offset and low frequency noise within the signal path by translating the radio frequency signal down to an intermediate frequency (IF) [9]. However it requires two off-chip filters for the purposes of band selection and image rejection. Thus radio architectures employing zero-IF and low-IF techniques requiring no off-chip image rejection filter is getting popular and some CMOS wireless chipset has already reached the commercial market with great success, such as WLAN, GSM, GPRS, Bluetooth, and DECT [10-17]. Nevertheless, the band selection filer is still needed and remained to be a challenge to be integrated. In order to comply with strict frequency regulations required by the communication systems, such as wide-band code-division multiple-access (WCDMA) receivers [7], and time-division-duplex (TDD) systems [8], and personal communications service (PCS) band [18], these filters have to be designed with high quality-factor (Q-factor) resonators.

The literature survey indicates that most CMOS active bandpass filters below the

C-band incorporate Q-enhanced inductors for resonator realization, e.g., actively Q-enhanced coupled inductors [7, 19], emulated coupled inductors [20], energy-recovered spiral inductors [21], and Q-enhanced LC bandpass biquads [22-23]. In view of integration, care should be taken as not to cause undesired magnetic coupling between these inductor-based resonators to deteriorate the filter response [23]. In addition, self resonance caused by parasitic capacitance and skin effects from process limitations further increase the design complexity for using spiral inductors in active LC filters [18, 23-24].

On-chip CMOS passive resonators formed of transmission lines typically have Quality-factors (Q-factors) proportional to the square root of the operating frequency. A carefully designed CMOS-bandpass filter at millimeter-wave frequency generally provides an adequate Q-factor. Passive bandpass filters at 30 GHz and 40 GHz have been found to perform reasonably well [25-26]. However the perception of server loss problem and large chip area for monolithic transmission lines limits further explorations in filter realization at low microwave frequency range. As an attempt has been made for fabricating passive element in highly resistive silicon (HRS) substrate, however, the area of the realized second-order bandpass filer at 6 GHz is still large [27]. In contrary, the meandered complementary conducting strips transmission line (CCS TL) has recently demonstrated its usefulness for an LC-free 5.2 GHz oscillator design with an area of only 500x600 μm^2 in standard 0.25μm CMOS technology [28]. Thus this dissertation focuses on the development of the CCS-TL based active bandpand filter at low microwave frequency range [29-30]. The approach adopting CCS-TL has been chosen for its consistent propagating characteristics, compactness in size, and applicable for general filter synthesis methods.

1.2 Organizations

The propagating characteristics of the meandered complementary-conducting-strips transmission line (CCS TL) in the standard CMOS 0.18 μm technology are studied in Chapter 2. The meandered CCS TL has a superior slow wave property than the meandered microstrip, thus it is suitable for the compact transmission-line based active filter design. Chapter 3 begins with a technical survey on active inductor, active LC resonator, and negative resistance commonly employed in monolithic microwave active filter designs reported in the literature. Then a preliminary experiment of a second-order 5.5 GHz dual-behavior resonator (DBR) bandpass filer based on active CCS TLs is described. Chapter 4 discusses the design and implementation of a second-order 6.02 GHz active bandpass filter based on Q-enhanced CCS TL based half-wavelength resonators. The newly proposed architecture is analyzed in detail with respect to loss compensation, noise property, linearity, and stability. Chapter 5 summarizes the contributions in this dissertation and recommends for the future researches.

CHAPTER 2

CMOS Synthetic Thin-Film Transmission Line

This chapter performs a comparative study of the meandered complementary conducting strips transmission line (CCS TL) against the meandered microstrip in a standard 0.18 μm CMOS technology. Before performing the study, the accuracy of the analysis method is verified in Section 2.1 by comparing measured and analyzed results of a meandered CCS TL test structure. Then the microstrip line width and the central patch of the CCS TL are used as controlling parameters to investigate the guiding properties in the meandered form. Meandered CCS TLs with unequal and equal central patch and connecting arms are also studied to illustrate the advantageous features for applications demanding high characteristic impedance. The results are presented in Section 2.2 and some of them are further applied to CCS active filter designs in Chapter 3 and 4.
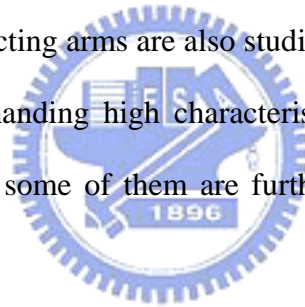
2.1 Validity Check of Software-Based Analysis Method

Meandered CCS TL is a two-dimensional guiding structure composed of straight and bend CCS unit cells with non-uniform cross sections as illustrated in Fig. 2.1(a). At the top layer of a CCS unit cell contains a central patch and two connecting arms for interconnections with widths of W and S, respectively. At the bottom layer of the unit cell is a mesh ground plan of a W_h x W_h opening with a periodicity of P. The photograph of the layout of the experimental meandered CCS TL in CMOS 0.18μm technology used for validity check is depicted in the right side of Fig. 2.1(b). This structure utilizes the topmost Metal-6 layer for central patches and connecting arms

and the Metal-2 layer for the mesh ground plan. The employed CCS unit cell has a periodicity of 34 μm, a central patch of 10 μm, a connecting arm of 10 μm, and a square opening in the mesh ground plan of 30 x 30 μm, respectively. At the outer border of the bottom layer, the metal width was enlarged to 34 μm to establish a physical connection between the mesh ground plan and the ground-reference pads at Metal-6 layer through VIA 1 to 5 layers. Notably, this CMOS monolithic CCS TL structure occupied an area of 919 x 701 μm^2 has 234 CCS unit cells with a total length of 7.956 mm.

The small-signal two-port scattering parameters were measured from 1 to 8 GHz after the on-wafer short-open-load-through (SOLT) procedures had been preceded. Effects introduced by the ground-signal-ground (G-S-G) probing pads had also been removed by the deembedment. Then the effective complex propagation constant and complex characteristic impedance were extracted from the equivalent complex ABCD matrix transferred from the measured two-port scattering parameters [31].

Validity checks of the software-based analysis method were conducted by comparing the extracted propagation characteristics and characteristic impedances from the EM simulation with those from the measurement. Theoretical two-port scattering parameters of a 6x3 two-dimension lattice CCS TL circuit with the same geometrical size of the unit CCS cell are obtained by applying an EM solver (Ansoft^{TM} HFSS v10.0), using the finite element method. Regarding the physical parameters including layer thickness, relative dielectric constant, and conductivities of the silicon substrate and alumina-metal layers of the particular CMOS 0.18μm technology used for theoretical analysis are shown in the left side of Fig. 2.1(b).

W

P

S

X

Y

W_h

A

B

Cross Section A   Cross Section B

(a)

t_{M6}

10.52μm/SiO$_2$ t_{M2}

482.6μm/Si

ρ =11 Ω · cm

t_{M6}=2.0 μm/Al
t_{M1}=0.55 μm/Al
σ_{Al}=3.33e^{+7} S/m
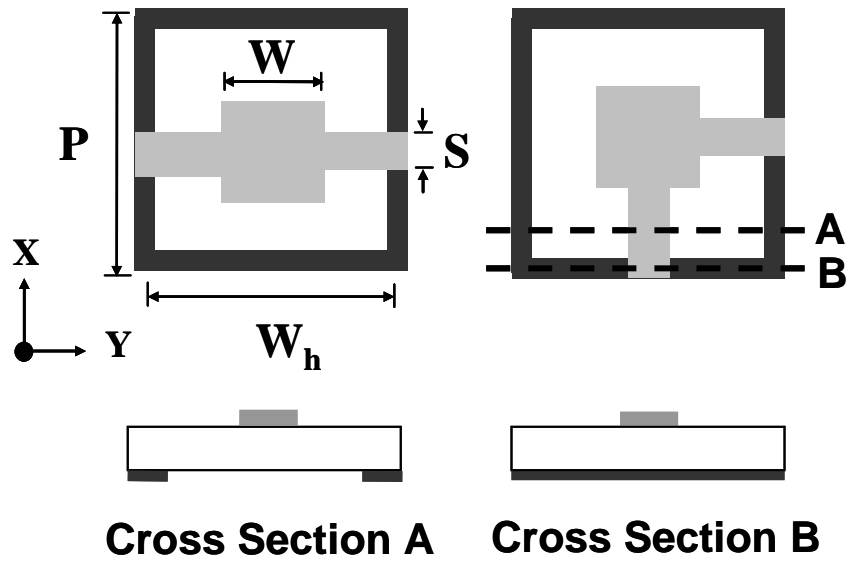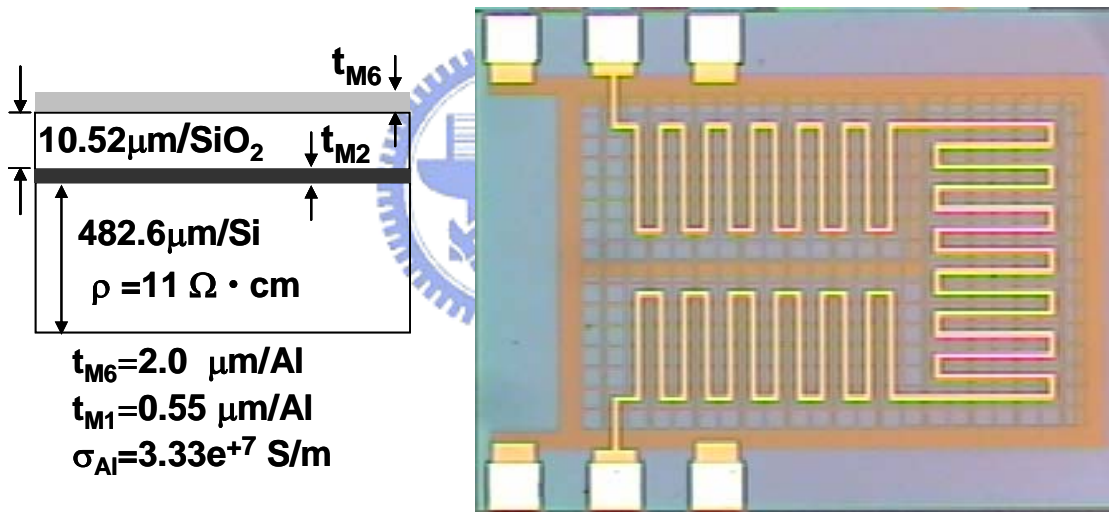
(b)

Fig. 2.1 CMOS monolithic 0.18 μm complementary conducting strip transmission line (CCS TL). (a) Straight and bend CCS unit cells. (b) Photograph of the 7.956 mm meandered CCS TL test structure with W equal to S. The right inset illustrates the material parameters.

The data derived form the measurement and simulation are show in solid and dotted lines in Fig. 2.2. For clearness, the complex propagation characteristics ($\gamma=\alpha+j\beta$) were illustrated as the normalized phase constant (β/k_0) and attenuation constant (α/k_0), respectively. Through the entire spectrum, the simulated propagation constants were in good agreement with the measured data, as shown in part (a) of Fig. 2.2. The maximum deviation of the normalized phase constant is 0.17 at 1.0 GHz and less than 0.03 from 4 to 8 GHz. Regarding the normalized attenuation constant, the maximum deviation is 0.34 at 1 GHz and continuously get smaller as frequency increased. For example, at 6 and 8 GHz the deviations are reduced to 0.05 and 0.02. Within the C-Band spectrum, from 4 to 8 GHz, the root-mean-square (RMS) values of the normalized phase constants derived from the measurement and simulation are 2.04 and 2.07. The corresponding values of the normalized attenuation constants are 0.36 and 0.42. Part (b) of Fig. 2.2 plots the real ($Re(Z_c)$) and imaginary ($Im(Z_c)$) parts of complex characteristics impedance (Z_c). The RMS values of real part characteristic impedances derived from the measurement and simulation are 64.86 and 66.78 Ω. The corresponding values of imaginary parts are 10.57 and 11.04 Ω, respectively. In summary, the relative RMS deviations of γ and Z_c are 2.65% and 2.99% across the C-Band. The data shown in Fig 2.2, therefore, have demonstrated the software-based analysis method could predict the guiding characteristics of meandered CCS TLs in CMOS 0.18μm technology with a reasonable confidence level, a deviation less than 3 percentages.
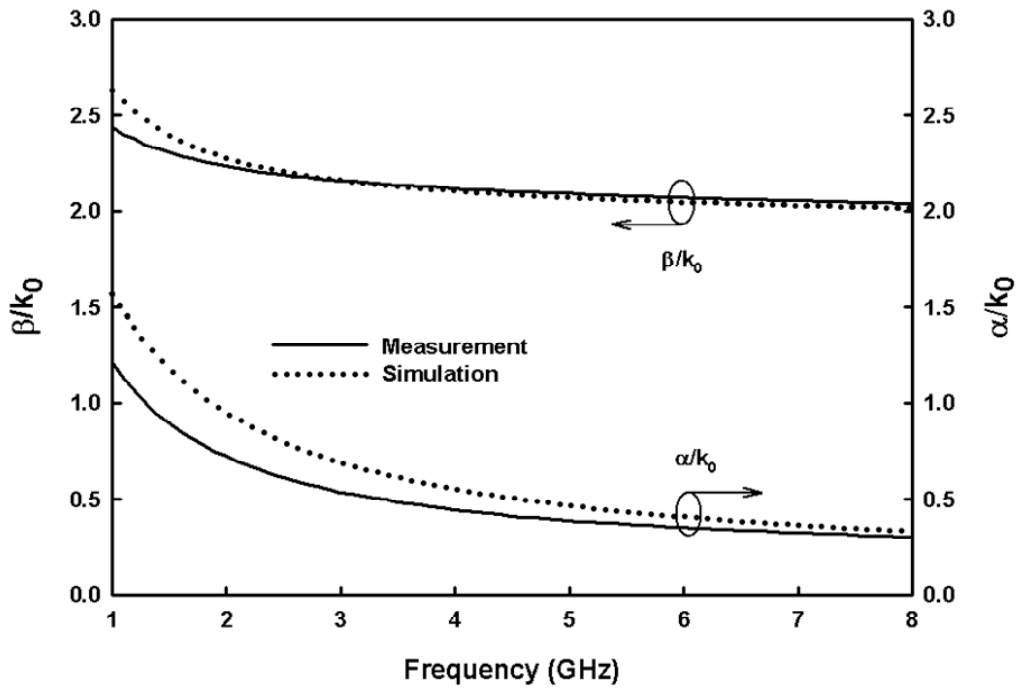
(a)
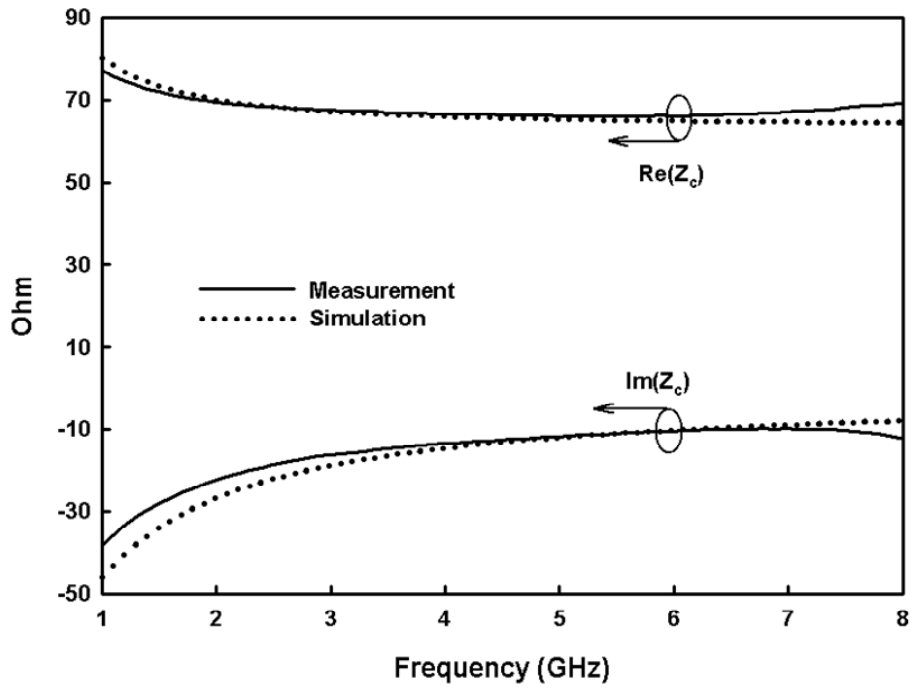
(b)

Fig. 2.2 Measurement and simulation results of equivalent transmission line characteristics of the meandered 0.18 μm CMOS CCS TL in Fig 2.2(b) from 1 to 8 GHz. (a) Normalized attenuation (α/k_0) and phase (β/k_0) constants. (b) Real ($Re(Z_c)$) and imaginary ($Im(Z_c)$) parts of characteristic impedance (Z_c).

2.2 Comparative Study of CCS TL against Microstrip in Meandered Configuration

Many observations of meandered CCS TLs against microstrips (MS) in printed circuit board (PCB) technology had been reported in [28, 32]. The comparative study performed in this section, rather, emphasized on CMOS monolithic technology for compact microwave integrated circuit integration and guiding properties of meandered CCS TLs with high characteristic impedances (Z_c). The particular 0.18 μm CMOS technology applied to this study was identical to that of the validity-check experiment in Section 2.1. In order to have enough impact on guiding properties of meandered CCS TLs, the ground plane opening and the periodicity were enlarged to 40 μm and 44 μm. The width of central patch was varied from 2 μm to 30 μm corresponding to the minimum and maximum permissible width of Metal-6 layer. In additional to the meandered CCS TL cases of equal connecting arm and central patch, the cases of S unequal to W with S = 6 μm and S = 15 μm are also included.   Part (a) of Fig. 2.3 indicates a 5 x 3 2D meandered CCS TL of S = 6 μm and W = 20 μm. For a fair comparison, the meandered layout pattern of the microstip is arranged the same as that of the meandered CCS TL, as demonstrated in Fig. 2.3(b). The line width of the microstrip is also set equal to the center patch (W) of the CCS TL. The software-based analysis method is applied to derive the guiding properties, real part of Z_c (Re(Z_c)), normalized phase constant (SWF), and loss per guiding wave length (dB/λ_g), of meandered CCS TLs and microstrips at 6.0 GHz. The analyzed results are summarized in Fig. 2.4 and 2.5.
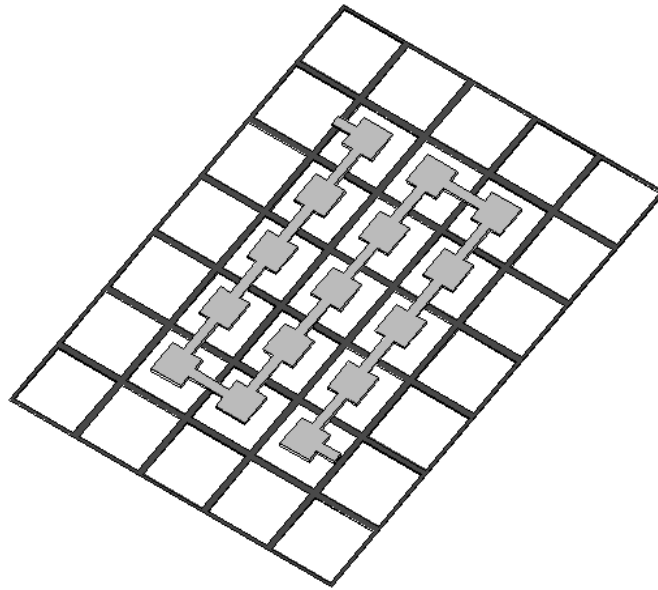
(a)
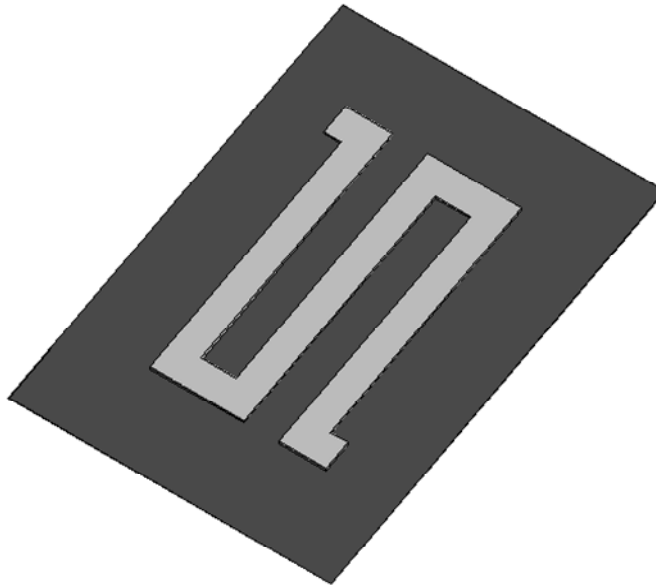
(b)

Fig. 2.3 Meandered test structures used at the comparative study of CCS TL anagist microstrip in standard CMOS 0.18 µm technology. (a) 5 x 3 2D meandered CCS TLs with W, S, W_h, and P equal to 20, 6, 40 and 44 µm. (b) Meandered microstrip with a 20-µm width.

When W is 2, 10 and 30 μm, the real part of characteristic impedance ($Re(Z_c)$) of the meandered CCS TL of S equal to W, plotted in the solid black square symbol in Fig. 2.4(a), illustrates a 20.95, 19.89, and 12.57 ohm increase of the corresponding meandered microstrips (MS), drawn in the hollow square one. This result shows that the meandered CCS TL of S equal to W possesses a higher characteristic impedance than that of the meandered MS. Compared the meandered CCS TLs of S unequal to W with S equal to W, the increase in $Re(Z_c)$ is average 12.32 and 6.12 ohm when S = 6 μm and S = 15 μm for W varying from 20 μm to 30 μm. As expected, a wider S would results in a wider MS section within the meandered CCS TL introducing a lower value of Z_c [28]. Nevertheless, the meandered CCS TL with non equal S and W is a more efficient guiding structure for designing high characteristic impedance and suitable for compact layout integration. Regarding the sensitivity on variations in W, the Zc for meandered CCS TL of S = 6 μm decreased 8.26 ohm when W increased from 8 μm to 15 μm and decreased 6.12 for S = 15 μm and W increased from 20 μm to 30 μm. However, the decreases of Z_c for the meandered microstrip against the same variations in W were 20.0 and 8.04 ohm, respectively. These observations indicate that the meandered CCS TL with non equal W and S is less sensitive in lowering Zc due to the meanderings than the meandered microstrip.

Part (b) of Fig. 2.4 plotted the slow wave factors (SWF) of meandered CCS TLs and microstrips against W. As could be observed easily, the SWFs of the meandered CCS TLs of S equal to W are almost insensitive to the change of W across the entire range of interest. The averaged SWF of the particular case is 2.085 with a maximum deviation of only 1.37%. Since a wider S or an equivalent wider MS section would cause a decrease in the effective series inductive component. But a wider W would also results an increase in the effective shut capacitive component (C). Therefore, the

resultant phase constant, proportional to $\sqrt{LC}$, has insignificant changes. However the

effective Z_c, proportional to $\sqrt{(R + j\omega L)/(G + j\omega C)}$, would be lowered which had

been observed in Part (a) of Fig. 2.4. Moreover, the meandered CCS TLs of S unequal

to W show even slower guiding properties than S equal to W. Since their effective

series inductive component (L) were not changed due to a fixed size of S. But the

effective shunt capacitive part (C) were enlarged with the increase of W. Thus the

resultant SWFs exhibit monotonically increases against W. On the contrary, SWFs of

the meandered microstrips fall from 1.995 to 1.797 with a decrease rate of 9.9% when

W increase from 2 μm to 30 μm. Therefore the meanderings of microstips cause a

significant reduction in the SWF. Which reflecting the fact the propagating

characteristics of meandering CCS TLs are less susceptible to the meanderings than

the meandered microstrips.

Figure 2.5 depicts the loss per guiding wavelength (dB/λg) against Re(Z_c). The size

of W employed in each structure was also shown beneath the corresponding symbol in

the same figure. When Re(Z_c) above 61.24 Ω, the meandered CCS TLs of S unequal

to W with S = 6 μm demonstrate lower loss properties than that of the meandered TLs

of S equal to W. Since the average metal strip of the first structure is averagely wider

than the second one. Besides the first structure also has a shorter guiding wavelength,

inversely proportional to the SWF, as explained before. Therefore a better loss

characteristic for high-impedance CCS TL of S unequal to W in meandered form

could be expected. Compared to meandered microstrips, either meandered CCS TLs

of S unequal to W or S equal to W demonstrates lower dB/λ_g at the same

high-characteristic-impedance region. The behind mechanism also relies on a wider

metal strip and superior slow wave property. When Re(Z_c) is about 80 ohm, for

example, compared to the meandered microstip the reduction ratios of dB/λ_g for CCS

TLs of S equal to W and S unequal to W are 30.89% and 44.74%, respectively.

For characteristic-impedance below 57.23 ohm, the meandered microstrip has the lowest loss property, but the corresponding SWF and $Re(Z_c)$ are much sensitive to the meanderings, as discussed previously. Base on an equal W, however, meandered CCS TLs of S unequal to W demonstrates not only higher $Re(Z_c)$, better SWF and lower dB/λ_g than those of meandered CCS TLs of S equal to W. The validity of these facts could be justified through comparing the performance among the first structure of S = 15 μm and the S equal to W cases when W varied from 20 to 30 μm. Following observations could be summarized according to Fig. 2.4 and 2.5: the averaged increase ratios on Z_c and SWF are 16.03% and 7.13%, and reduction ratio on dB/λ_g is 4.29%, respectively. The mechanism by which the dB/λ_g decrease by reducing S mainly involves an increase in the effective series inductive component, since the attenuation constant could be approximately expressed as $R\sqrt{C/L}$ when the effective shunt conductive component is negligible. Besides, the first structure also has a superior SWF property. It is evident that meandered CCS TL of S unequal to W has more advantages than the ones of S equal to W in terms of guiding properties.
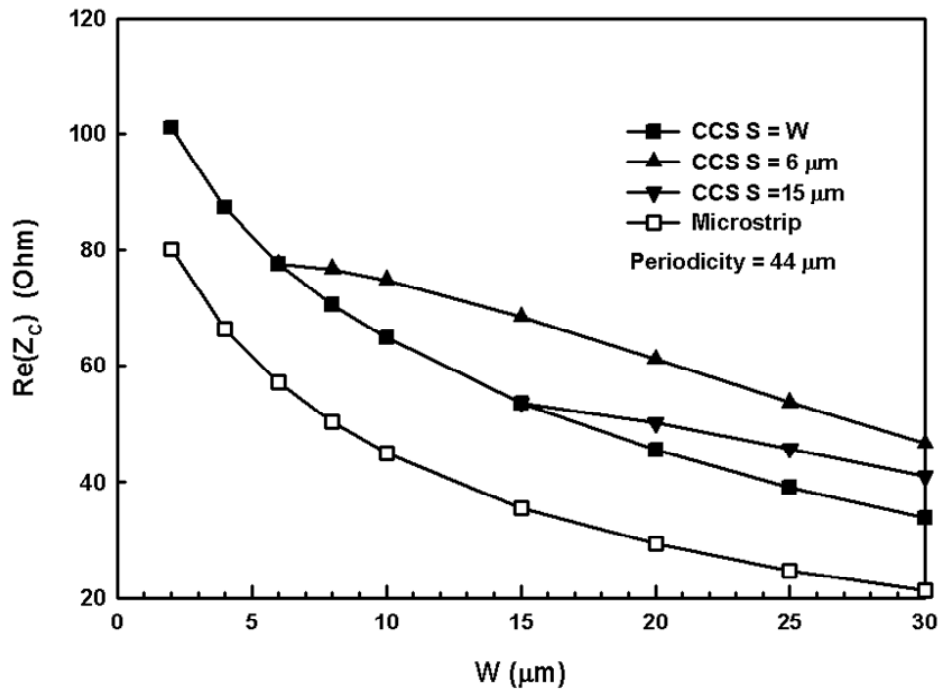
(a)
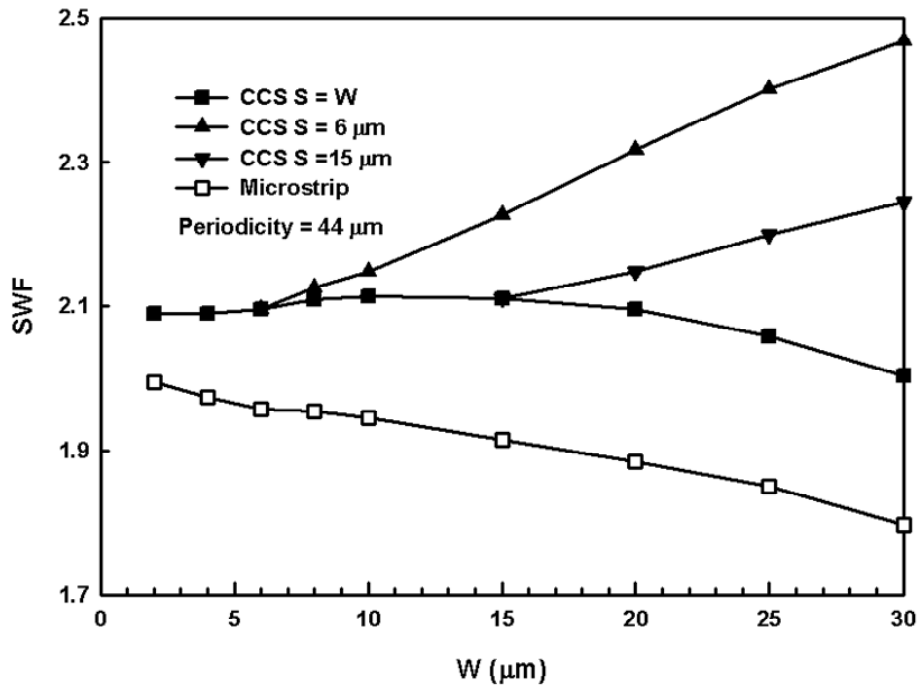
(b)

Fig. 2.4 Transmission line characteristics of meander CCS TL and meandered microstip derived from the software-based analysis method at 6.0 GHz. (a) Real part of characteristic impedance ($Re(Z_c)$), and (b) slow wave factor (SWF).
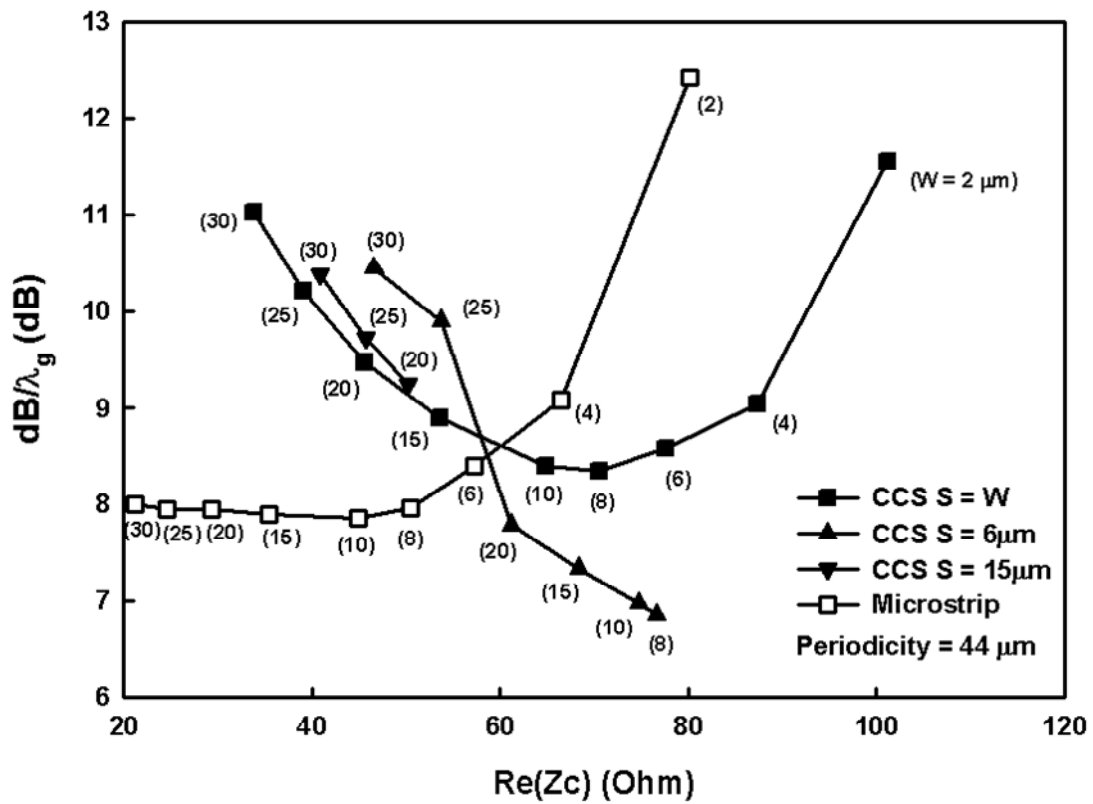
Fig. 2.5 Loss per guiding wavelength (dB/λ_g) of meandered CCS TL and meandered microstrip derived from the software-based analysis method at 6 GHz.

2.3 Discussion

In this chapter the guiding characteristics of CMOS 0.18 μm monolithic meandered CCS TL with non equal and equal connecting arm (S) and central patch (W) have been analyzed. The meandered CCS TL compared to the meandered microstrip has at least three advantageous points: (1) less sensitive to lowering characteristic impedance and slow wave factor by meanderings, (2) better loss characteristics for high-impedance lines, (3) higher characteristic impedance value for wide metal strip. Of more interest is the fact that the meandered CCS TL with non equal S and W even shows a better transmission line performance than the one with equal S and W on the same advantageous points.

CHAPTER 3
Approaches of Microwave Active Filters

This chapter investigates an innovating approach of fully monolithic CMOS active filters incorporating meandered complementary-conducting-strips transmission line aimed for filtering functions commonly required by the radio receiver front end. Conventionally these functions are performed by off-chip SAW filters. Recently, on-chip BAW filters had also been proposed to overcome this impediment with an additional payment of process modifications. However, by introducing integrated active elements compensating or emulating the on-chip passive components, active filters exhibiting good frequency selectivity, low passband attenuation, and small in size show considerable interest. Section 3.1 gives a general overview of active inductor and active resonator techniques traditionally employed in active filter deisgns. Then a preliminary experiment of a 5 GHz active bandpass filter based on active CCS transmission lines is introduced in Section 3.2.
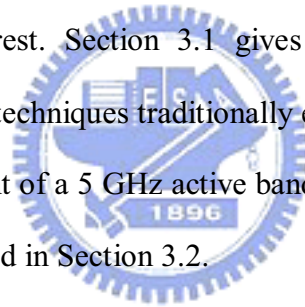
3.1 Overview on Active Inductor and Active Resonator Techniques

Analog LC-Ladder filter, in 1966, had been discovered to be highly insensitive to component variation [33]. In integrated circuit (IC) technology, planar or stacked spiral inductors are usually applied for implementing large inductances. However, several fundamental problems such as excess series resistance, high-frequency resonances, and mutual coupling limit its usefulness. Therefore, active inductors have been developed to replace the passive ones.

Since the gyrator network has an impedance inversion property. An active gyrator with a capacitive load, therefore, could simulate an active inductor and be

used in realizing inductorless active filters [34]. Monolithic active gyrators could also be constructed with op-amp or transconductor circuits [35]. Overlap capacitance between the input and output of the monolithic CMOS transconductor, however, normally introduces phase lag in the transconductance function and limits the maximum usable frequency of this active inductor [36]. Canceling of this overlap capacitance by a balanced gyrator topology had been successfully applied in the VHF (up to several hundreds of MHz) active filter design [37]. For the use of active gyrator in monolithic microwave integrated circuit, several active notch filter designs had been reported in GaAs technoloy [38-40].

Using a common-source cascode-FET with resistive feedback topology to implement a relatively lossy broadband monolithic GaAs active inductor had been report in [41]. A significant reduction in the series resistance of this active inductor with the use of common-gate cascode-FET feedback arrangement was lately published in [42]. To realize a broadband flat inductive response, however, either configuration requires the two C_{gs} capacitances of each FETs must be identical to cancel each other out. The required transconductance (g_m) of each FET must larger than $(\omega C_{gs})^{1.5}$, and the maximum operating frequency of this active inductor is ideally about one-half of the small-signal unity frequency ($f_t = g_m/2\pi C_{gs}$) of the FET. The related applications in monolithic GsAs tunable narrow-band active filters were reported in [43-46].

As a well-known approach, the negative resistance (-R) circuit could be used to compensate the loss in passive transmission line, lump inductor, or lump capacitor to realize an active filters. For an active LC resonator, the –R circuit is an integral part of the lumped LC resonator to cancel out the dissipative loss. This technique had been used in monolithic CMOS, SiGe, and GaAs technologies [7-8, 19-24, 47-54]. For monolithic CMOS and SiGe active LC resonators, however, the essential on-chip

spiral inductor usually has a lower resonance frequency and could not provide a broadband flat inductive response. Thus a Q factor tuning circuit has to be adopted within the filtering system [18, 23-24]. In contrary, transmission line is a distributed element and demonstrates a broader and much stable characteristic against frequency. Therefore monolithic CCS TL is applicable for active filter designs for its advantageous guiding property and less sensitive to meandering as discussed in Chapter 2. The remaining challenge is how to compensate its propagating loss in the CMOS monolithic approach. To date, several design techniques had been developed to integrate the negative resistance circuit with distributed transmission lines in hybrid and GaAs technologies [55-58]. For example, C. Y. Chang et al. had used coupled line resonators and coupled negative resistance to realize a hybrid tunable 200-MHz wide active bandpass filter at 10.5 GHz [55]. M. Ito at al. had implemented a monolithic 2.6-GHz wide active bandpass filter at 65 GHz by applying two CPW transmission line quarter-wave resonators terminated by negative resistances in GaAs technology [56]. To get a clear insight in the restrictions and feasibilities of the negative resistance circuits used both in active LC and transmission-line resonator, some negative resistance circuits commonly appeared in the literature would be surveyed in the following subsection.

Apart from the techniques mentioned above, some bandpass or notch amplifiers have been built by cascading a passive bandpass or notch segment with the low noise amplifier (LNA) [10, 59-61]. However, these filter have restricted frequency selectivity and not applicable for the general filter synthesis methods. Nevertheless, this approach is advantageous for its compactness and design simplicity. In contract, the transverse or recursive typed active bandpass filter usually requires 3-dB coupler, power combiner, and LNAs to perform analog signal processing [62-67]. The general filter synthesis methods could neither be applied to this filter.

3.1.1 Negative Resistance Circuits

In the circuit topologies requiring single active device, the circuit can be in common gate configuration with an inductive feedback, in common-source configuration with a capacitive feedback, or in common-source and common-drain inductive and capacitive series feedback, as shown in Fig. 3.1(a), (b) and (c). In the ideal case, the negative resistance circuit of Fig. 3.1(a) has an input impedance at the source terminal given by

$$Z_{in} = \frac{1 - \omega^2 L_f C_{gs}}{g_m + j\omega C_{gs}} \tag{1}$$

This circuitry is fist introduced in [68] and also called the active inductor. By considering the gate resistance and other parasitics of a real transistor, this circuit could not achieve negative resistance without introducing an additional inductance in the drain terminal. Another drawback is the requirement of large L_f resulted from the high frequency phase shift introduced by the transconductance of a real device [53, 69]. For the ideal case of Fig. 3.1(b), the input impedance at the gate terminal is expressed as

$$Z_{in} = -\frac{g_m}{\omega^2 C_{gs} C_f} - j\left(\frac{1}{\omega C_{gs}} + \frac{1}{\omega C_f}\right) \tag{2}$$

As can be observed, the higher frequency the more transconductance or power consumption is required to generative an equivalent negative resistance. Besides, the C_{gs} capacitance from the real device has a negative impact on the resulting negative resistance. Which could set inherent limitations for its usefulness in CMOS technology. The negative resistance circuit shown in Part (c) of Fig. 3.1 is also called the active capacitor. This circuit has demonstrated a superior noise performance in hybrid topology [70]. However, the bandwidth of negative resistance usually involves

a tradeoff between the value of Ld and parasitic resistance within the series feedback network at the drain terminal [71]. Which may enhance the design complexities and increase iteration times.

Part (d) of Fig.3.1 illustrates the coupled-inductor negative resistance circuit. The ideal effective input impedance seen at the primary inductor could be expressed as

$$Z_{in} = R_1 + j\omega L_1 + j\omega M \frac{i_1}{i_2} = R_1 + j\omega L_1 + j\omega M (Ae^{j\theta}) \qquad (3)$$

where $Ae^{j\theta}$ is the current ratio between the primary and secondary inductor, and M is the mutual inductance between the two inductors. When θ equals to 90^0 or 270^0, a negative resistance is generated and could be used to cancel the series resistance R_1 of the primary inductor L_1. This technique has been applied in CMOS technology for several active bandpass filters design [7, 19]. Notably, the capacitive coupling between the two inductors could cause phase difference in $Ae^{j\theta}$ and additional capacitive loss. Besides, CMOS on-chip transformer also suffers from the substrate loss [7]. In other words, this negative resistance circuit also has to compromise with the parasitic effects of on-chip inductive lump components.

In contrast, the small-signal resistance at the drain terminal of a Λ-type MOSFET, as illustrated in Fig. 3.2 (a), is inherently negative requiring no inductive component. Since under proper biasing conditions, the slop of its source-drain current (I_{DS}) is inversely proportional to the increase of the source-drain voltage (V_{DS}). The detailed physics of this voltage-controlled single-ended negative resistance device had been reported in [72]. For high frequency applications the bandwidth and tuning capability of a Λ-type MOSFET realized in a typical 0.18 μm CMOS technology is further investigated through circuit simulation. The transistor size (width/length) of N1, N2

and N2 NMOS are 0.5/0.18, 0.35/0.18, and 1.88/0.18 μm, and the VD potential of the Λ-type MOSFET is set at 1.05 volt. For clearness, the output impedance was transformed to equivalent shunt elements, as shown in Fig. 3.2(b). Both the magnitudes of negative conductance (-G) and intrinsic capacitance (C) were proportional to the DC potential at the gate terminal (V_G). The total power consumptions were 163.5 and 520.2 μW when VG is 1.4 and 1.8 volts, respectively. Besides, the negative conductance worked at least up to 10 GHz. Thus a Λ-type MOSFET has demonstrate its advantageous features in terms of requiring no passive component, low power, and low complexity and applicable to loss compensation in 0.18 μm CMOS technology.
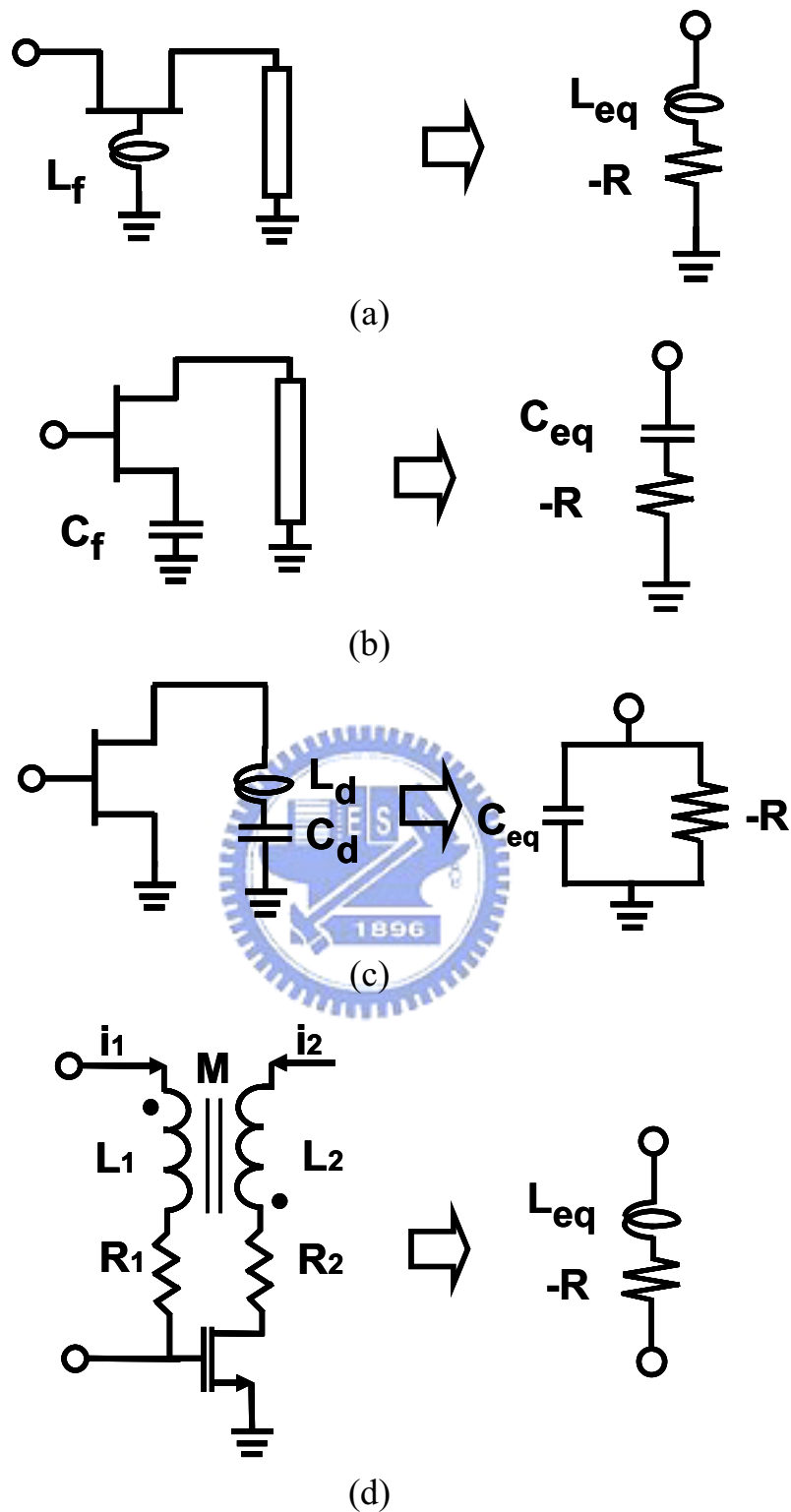
Fig. 3.1 Several circuit topologies of negative resistance circuit. (a) common-gate inductive feedback. (b) common-source capacitive feedback. (c) common-source and common-drain inductive and capacitive series feedback. (d) Coupled-inductor negative resistance generator.

(a)

(b)
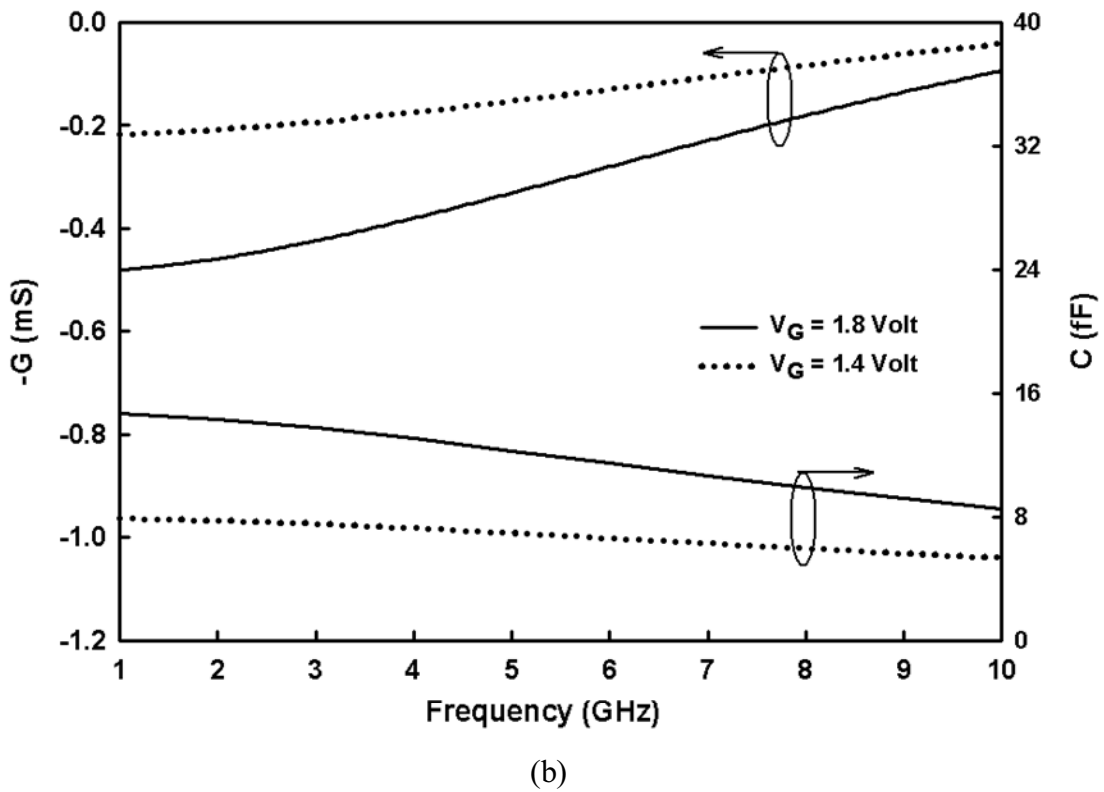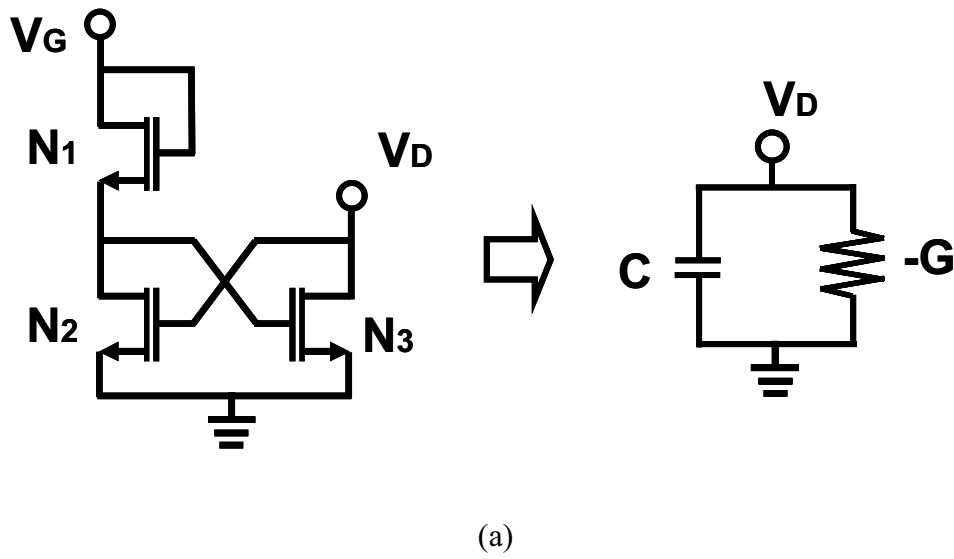
Fig 3.2 (a) The Λ-type MOSFET and its equivalent small signal circuit. (b) The input susceptance (Y=-G+jωC) of a typical 0.18 μm Λ-type MOSFET when V_D biased at 1.05 volt and V_G biased at 1.8 and 1.4 volt. The geometrical size (width/length) of N1, N2 and N2 NMOS transistors are 0.5/0.18, 0.35/0.18, and 1.88/0.18 μm, respectively.

3.2 CMOS Active CCS Transmission Line

To compensate the loss in a passive transmission line via negative resistance circuit, conventional approach is by using the negative resistance at the desired frequency band as introduced in Section 3.1. This section will explore the innovating approach of changing the transmission line characteristics fundamentally. At high frequency, as already known, the signal wavelength is comparable to the physical dimension of a transmission line. Thus one could utilize a negative resistance device to amplify the voltage and current along the lossy transmission line within periodic distance much smaller than the guided wavelength. Therefore the complete guiding structure is active in nature. The concept is illustrated in Fig. 3.3(a). The original per-unit-length shut conductance component within the distributed transmission line model is replaced by negative conductance. By using Λ-type MOSFETs as the negative resistance device, the complete schematic including biasing voltages and a passive transmission line is shown in Fig. 3.3(b). The DC potential V_D of all Λ-type MOSFETs is carried at the signal trace of the original passive transmission line. The negative resistance tuning mechanism of Λ-type MOSFET is used to adjust the gain of this active transmission line by set the DC potential of V_G.

The guided wavelengths of the particular CMOS meandered CCS TL analyzed in Section 2.1 range from 34.72 to 18.20 mm when frequency varies from 4 to 8 GHz. Using an negative resistance to distributed compensate the loss within this TL, therefore, the negative resistance device should be inserted along the TL in a periodic distance much smaller than the guided wavelength at the highest frequency. For the first active CCS TL design, the Λ-type MOSFET was attached in every 3 CCS unit cells, a periodic distance of 102 μm, approximately five-thousandths of the guided wavelength of the passive CCS TL at 8 GHz.
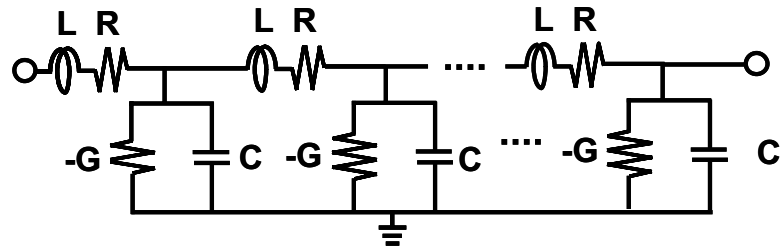
(a)
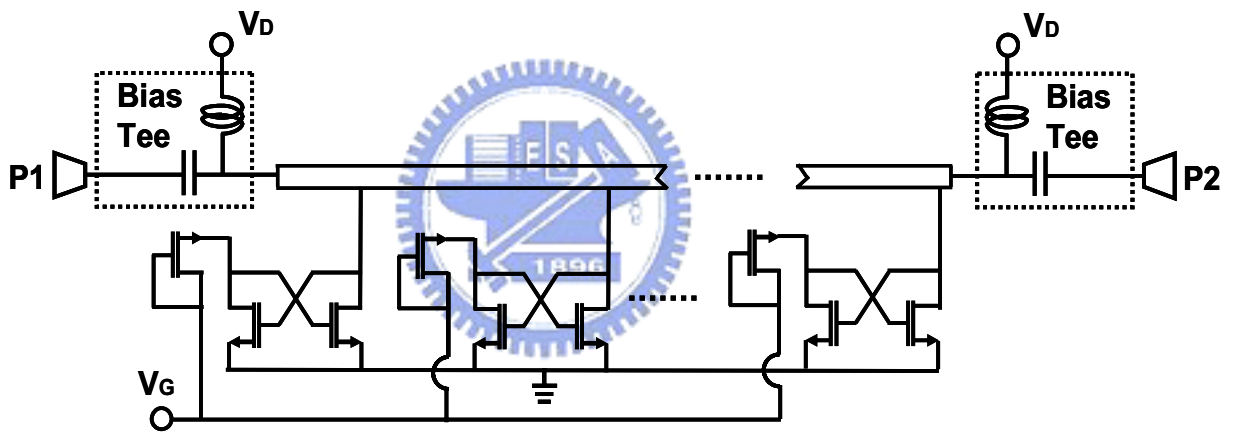
(b)

Fig 3.3 (a) The distributed transmission line model of the proposed active transmission line circuit. (b) The schematic of the proposed active transmission line adopting Λ-type MOSFETs.

The validity of this concept is checked by the same complex propagating characteristics and characteristic impedance extraction procedure from two-port scattering parameters described in Section 2.1. For clearness, the inductance (L), capacitance (C), resistance (R), and conductance (G) per unit length (mm) of the passive and active CCS transmission lines are illustrated in part (a) and (b) of Fig. 3.4. As expected, the series impedance (Z=R+jωL) per unit length of the transmission lines had not been changed, but the shunt susceptance (Y=G+jωL) element had been affected after the Λ-type MOSFETs are inserted. The sign of the unit-length conductance had been changed from positive to negative and the unit-length capacitance had also been increased. These observations match to the proposed concept of active transmission line. Apart from the lossless transmission line whose characteristic impedance is real and equal to $\sqrt{L/C}$, the unit-length resistance and conductance of this active transmission line could not be neglect after attaching the negative resistance device. As shown in Fig. 3.5(a), the resultant characteristic impedance still possesses an imaginary part, and the magnitude is dropped due to the increase of unit-length conductance and capacitance. Regarding propagating characteristics, illustrated in part (b) of Fig. 3.5, the slow wave factor was increased from 2.09 to 3.28 and the gain per guiding wavelength increased from -8.5 to 0.025 dB/λ_g around 5.5 GHz. The active transmission line now has gain from 1 to 6 GHz. Thus, this distributed loss compensation approach applied in monolithic CMOS technology had been theoretically validated and could be further applied to the active filter design.
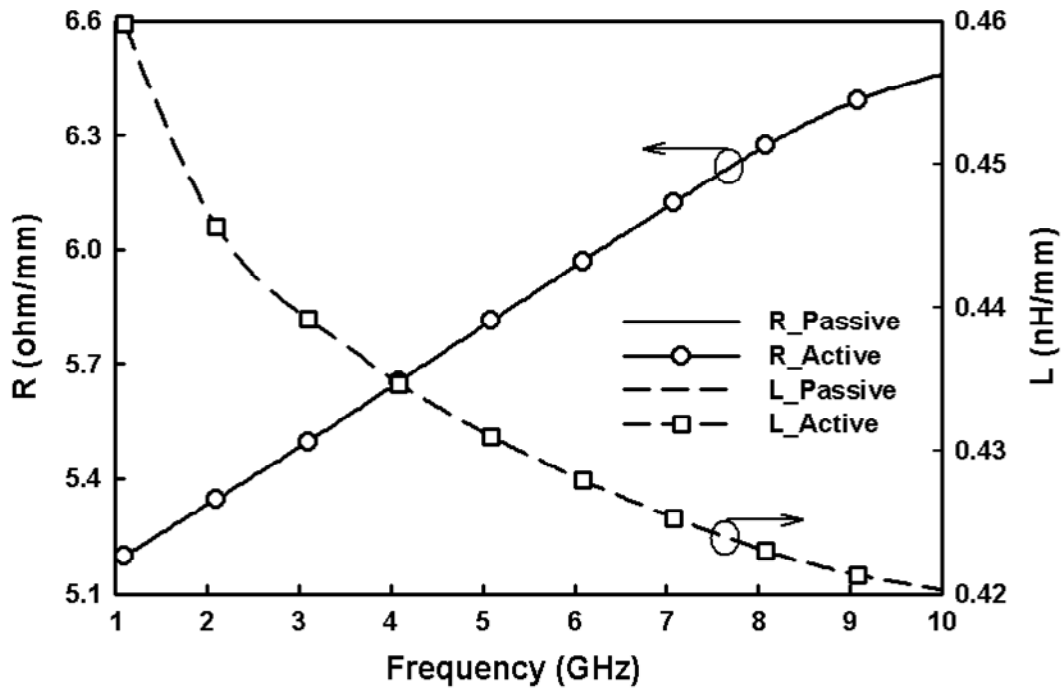
(a)
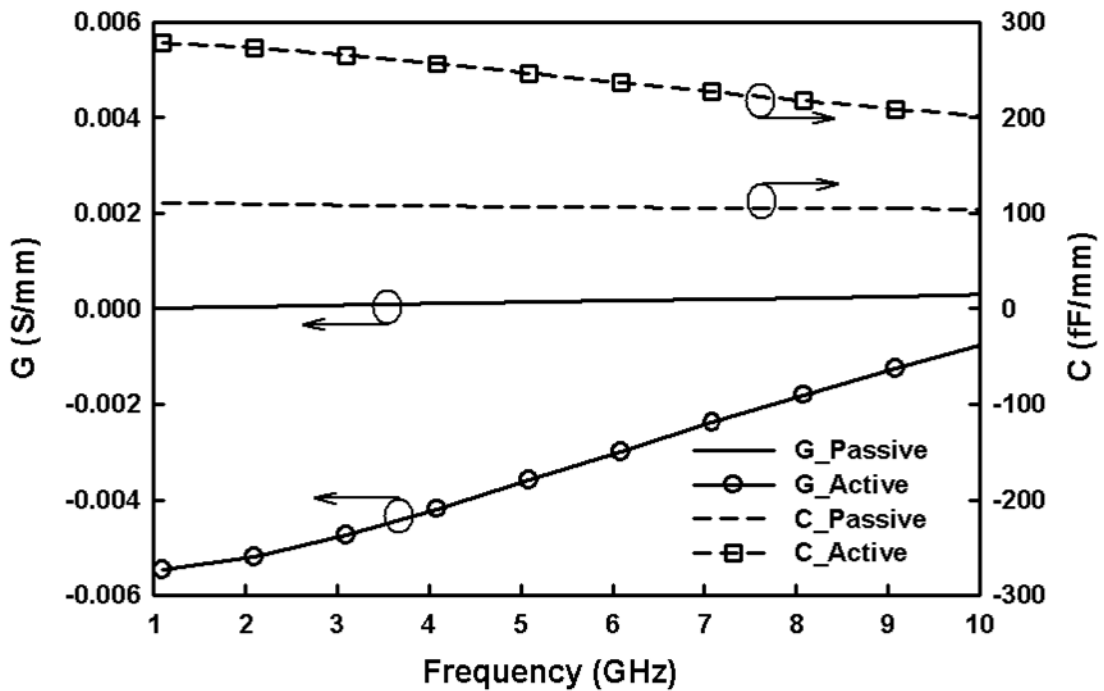
(b)

Fig. 3.4 The extracted distributed transmission line parameters of passive and active CCS TLs from 1 to 10 GHz. (a) Series resistance and inductance per millimeter. (b) Shunt conductance and capacitance per millimeter.

(a)
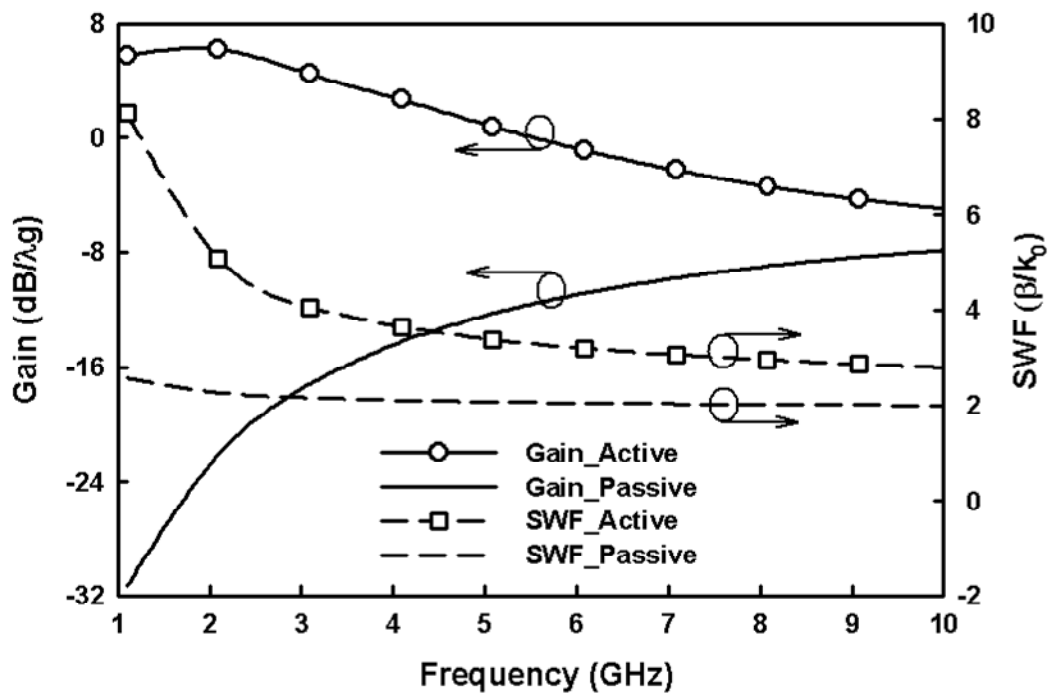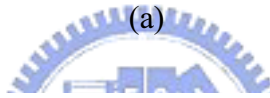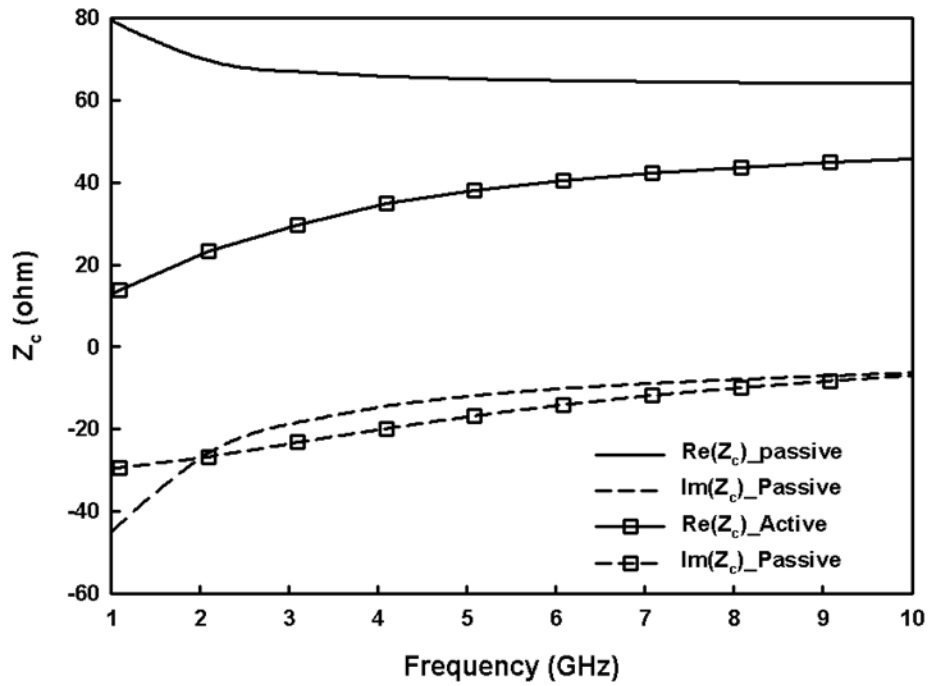
(b)

Fig. 3.5 The guiding characteristics of passive and active CCS TLs from 1 to 10 GHz. (a) Characteristic impedances (Z_c). (b) Gain per guiding wavelength (dB/λ_g) and slow wave factors (β/k_0).

3.3 A 5.5 GHz Active Bandpass Filter

Conventional transmission line based active bandpass filters either use passively coupled active resonators [55-58]. This section investigates the actively coupled active resonators approach based on the architecture of the so-called dual-behavior resonator (DBR) transmission line bandpass filter [32]. The active transmission lines presented in Section 3.2 are applied to realize the required DBRs and impedance inverters (J inverters) within the active bandpass filter.

The ideal equivalent circuit of a second-order 5.5 GHz DBR active transmission line (TL) bandpass filer is illustrated in Fig. 3.6(a). Each DBR is realized by one 90^0 active transmission line with Re(Zc) equal to 58 ohm at 8 GHz and another at 4.28 GHz. The series J inverter is realized by one 90^0 active transmission line with Re(Zc) equal to 46 ohm at 4.862 GHz. The size of periodicity, mesh ground plan, central path, and connecting arms for the CCS unit cell employed by all the CCS TLs are 34μm, 30μm, 6μm, and 6 μm, respectively. The Λ-type MOSFETs with the transistor size reported in Section 2.2.1 were attached to the CCS TL in every three CCS unit cells. Regarding the N_3 NMOS transistor used at the Λ-type MOSFET for the J inverter is 1.5 μm larger than those used at two DBRs to achieve the desired Re(Z_c). For simplicity, the DC potential required by drain terminals of Λ-type MOSFETs are all set to 1.0 volt and biased through the two ports of the prototype filter. The V_{G1} and V_{G2} voltages are 1.8 and 1.45 volt, respectively. The chip area is 1.19 x 1.19 mm^2 including right and left-side ground-signal-ground pads for the two ports of the prototype filter and up and lower-side ones for V_{G1} and V_{G2}.

$Z_1 = 58\Omega,\ \theta_1 = 90^0\ @\ 8\text{GHz}$
$Z_2 = 58\Omega,\ \theta_2 = 90^0\ @\ 4.28\text{GHz}$
$Z_3 = 46\Omega,\ \theta_3 = 90^0\ @\ 4.862\text{GHz}$
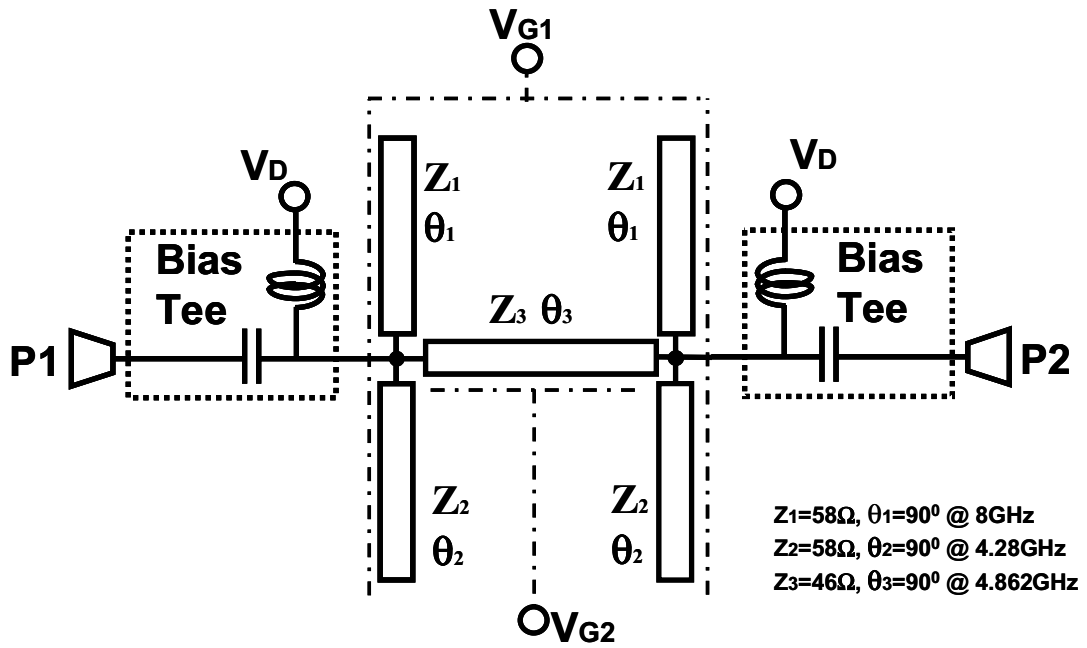
(a)
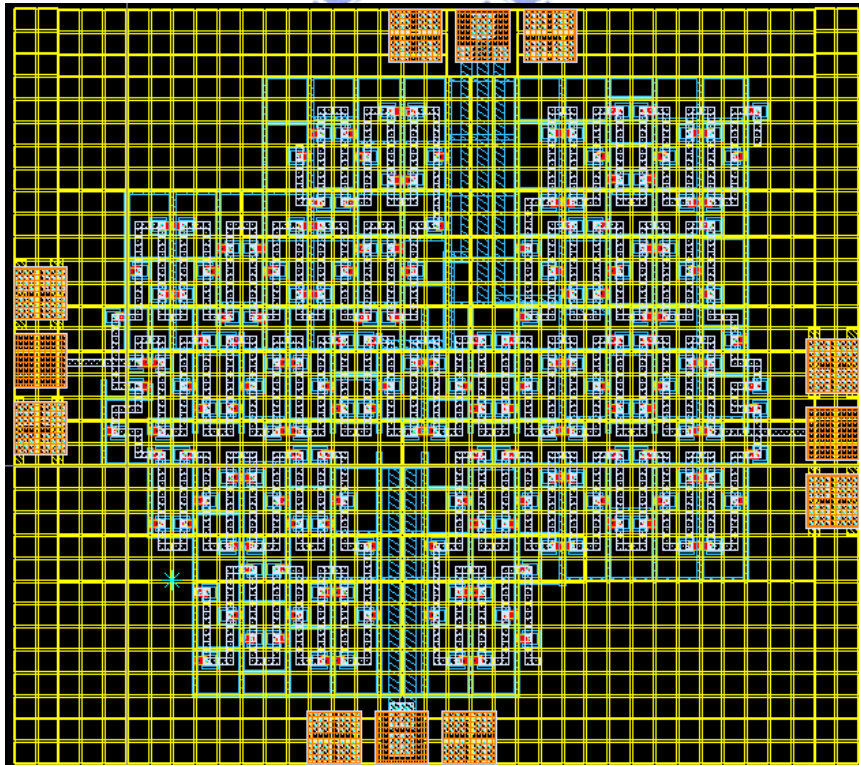
(b)

Fig. 3.6 (a) The schematic of the 5.5 GHz active bandpass filter based on the active CCS TLs. (b) The layout diagram of the 5.5 GHz active bandpass filter.

Figure 3.7(a) plots the simulated two-port scattering parameters based on 50 Ω reference impedance from 1 to 10 GHz. Two reflection zeros can be observed at 4.5 and 5.7 GHz. The central frequency is 5.5 GHz with a 3-dB bandwidth from 4.5 to 6.2 GHz and the simulated passband gain is 1.6 dB from 5.0 to 6.0 GHz. The return loss is below 9.0 dB from 4.3 to 5.7 GHz with an out-band rejection below 30 dB from 8 and 20 dB at 3.3 GHz. The total power consumption of this prototype active filter is about 35.70mW and the simulated input referred noise figure at the central frequency is 15.37 dB. However, the reflection coefficient is above zero dB from 1 to 1.8 GHz and from 6 to 8 GHz. Examining the real part of susceptance from the input of the prototype active filter, as illustrated in Fig. 3.7(b), an extremely large negative conductance is observed below 1 GHz. Further lowering the tuning voltages, V_{G1} and V_{G2}, could not totally remove the negative conductance from the input of the active filter unless the Λ-type MOSFET introduces no negative resistance anymore. Since the particular device generate more negative resistance at lower frequencies than at high-frequency band. Lowering VG does not change this trend against frequency but result in an overall decrease in the generated negative resistance and consequently deteriorating the filtering characteristics of the active CCS TL based filer.

After powering on the fabricated prototype active filter and performing on-wafer scattering parameter measurements with Agilent 8510C VNA, the measured results, as shown in Fig 3.8 (a), are not a filter responses but tremendous reflecting signals from the active filter. The measured input frequency spectrum from DC to 1 GHz is also shown in part (b) of Fig 3.8. The strongest oscillating signal is observed at 10.1 MHz with a power level of -8.3 dBm. Examining the inset of Fig 3.7 (b), one could easily recognize that the most negative input conductance of the active filter is -46 mS at 40 MHz. This frequency shift is caused by the parasitic within the measurement system including the Bias Tee, cable, RF probe, and connectors.

(a)
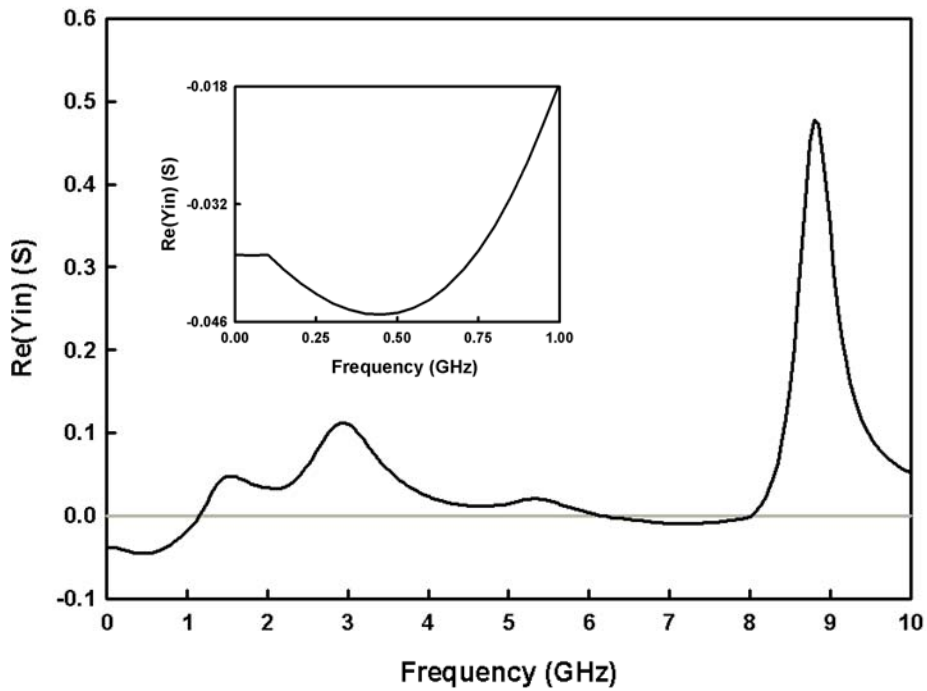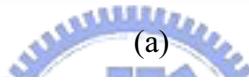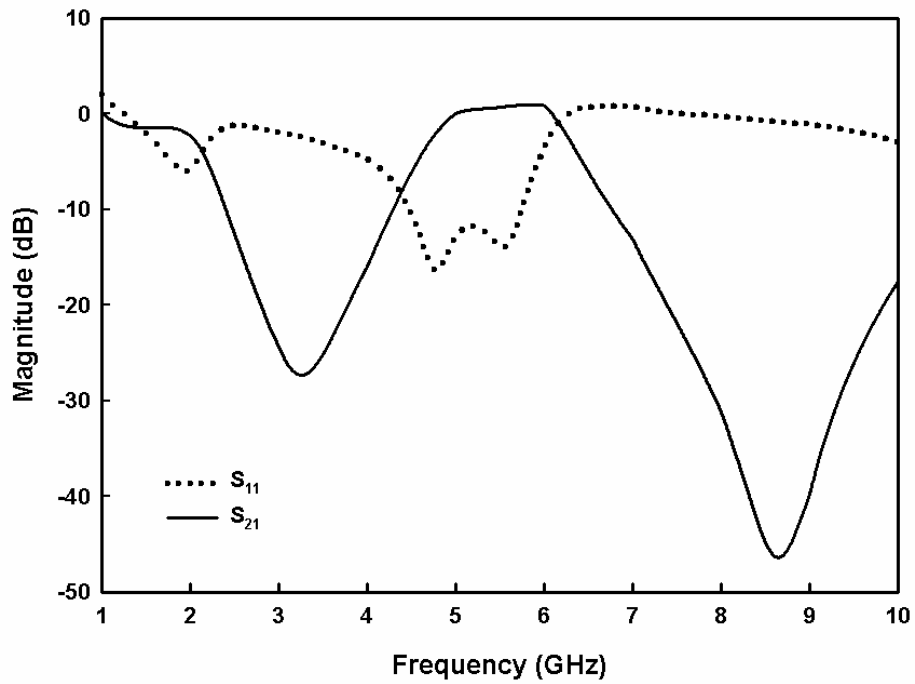
(b)

Fig. 3.7 The small signal characteristics of the 5.5 GHz second-order DBR bandpass filter based on active CCS TLs incorporating Λ-type MOSFETs. (a) Two-port scattering parameters from 1 to 10 GHz. (b). Real part on input susceptance (Re(Yin)) at P1 from DC to 10 GHz.
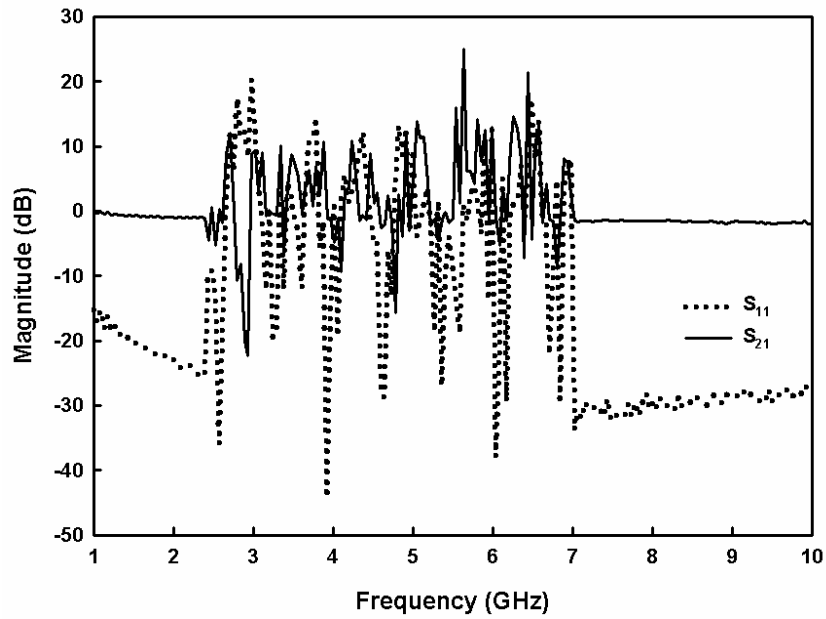
(a)
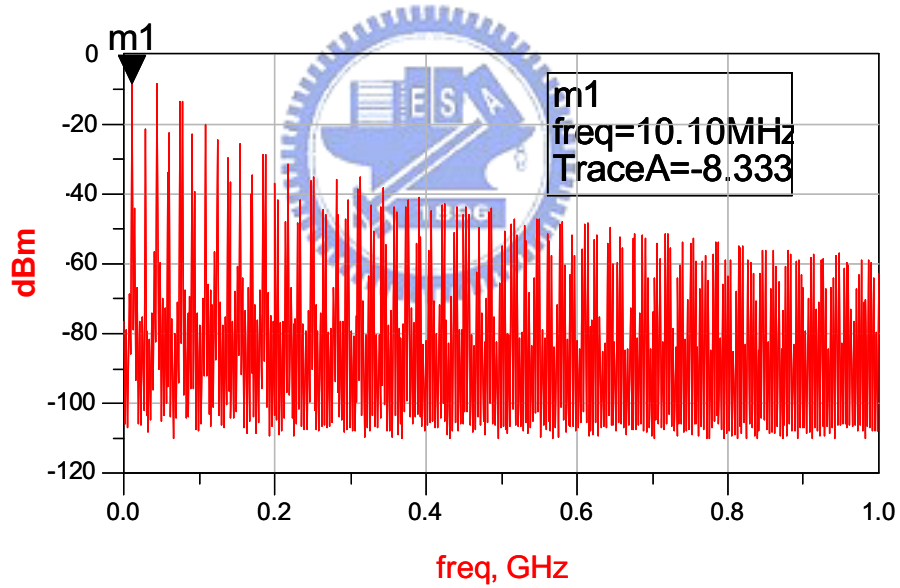
(b)

Fig. 3.8 Measured results of the 5.5 GHz second-order active bandpass filter. (a) Small-signal scattering parameter from 1 to 10 GHz. (b) The frequency spectrum at P1 from DC to 1 GHz.

3.4 Discussion

In this chapter several microwave active filter techniques employing the active inductor and the active resonator have been reviewed. Conventionally these techniques rely on the active transistor with low intrinsic capacitance (C_{gs}), high quality inductively feedback network, good transconductance efficiency, or good matching properties. To make monolithic CMOS active filters without these restrictions, an active CCS TL based approach had been chosen for its favorable lossless guiding characteristics and low complexity so that general filter synthesis methods could be used. However, the preliminary experiment was failed for instability issues at 10.1 MHz. Therefore the design philosophy must apply adequate loss compensation in order to make the active filter stable through the entire frequency spectrum. This strategy will be explored in Chapter 4 in view of the filter's architecture.

CHAPTER 4

Miniaturized C-Band Active Bandpass Filter

This chapter presents a C-Band monolithic active bandpass filter based on Q-enhanced half-wavelength resonators in a standard CMOS 0.18 μm technology. The quality factor of the complementary-conducting-strips transmission line (CCS TL) based half-wavelength resonator is reported in Section 4.1. Section 4.2 describes the design philosophy of the composite Q-enhanced resonator incorporating the cross-coupled pair circuit with the CCS-TLs based half-wavelength resonator. Within this novel architecture, the loss-composition mechanism could be well controlled both in architecture level and circuitry level. The two operation modes of the Q-enhanced resonator are theoretically investigated. Section 4.3 presents the realization of the second-order prototype bandpas filter based on the proposed Q-enhanced resonator in great detail. When consumes 3.0 mA from a 1.8 V supply, the active filter demonstrates a 2.2-dB insertion loss. Theoretically analyzed two-port scattering parameters are in good agreements with the measured results. The trend of the active bandpass filter with a 0.56-dB transmission gain is also theoretical and experimentally investigated. For this particular case, however, the reflection coefficient is greater than 0 dB from 6.5 GHz to 7.9 GHz. Based on a set of 50-Ω terminations, the noise and nonlinear properties of the prototype filter with a 2.2-dB insertion loss are further analyzed in Section 4.4 and 4.5. The stability analysis of the proposed active filter is performed in Section 4.6. Section 4.7 compares the filter performance with other published works and indicates the direction for further improvements.

4.1 CCS TL Half-Wavelength Resonator

In view of miniaturizing the size of complementary-conducting-strips transmission line (CCS TL) based half-wavelength resonator, the meandered CCS TL of the largest slow wave factor (SWF) should be employed. But there will be both DC and microwave signals carried in the top layer strip of the meandered CCS TL. Therefore the one with equal W and S of 30 μm is the best candidate for lowering the power dissipation introduced by the DC resistance. Base on the studies performed in Section 2.2, one can quickly estimate the physical length of a half-wavelength resonator by using CCS unit cells of W = S = 30 μm, P = 44.0 μm, and W_h = 40 μm at 6.0 GHz to be 12,480 μm and such meandered transmission line can be compacted in an chip area of 748 x 748 $μm^2$. In contract, if the similar meandered microstip of a 30-μm width is applied, there will be an additional length requirement of 1.42 mm corresponding to a 12.1 % increase in the chip area. Though the loss property of meander microstrip is about 1.5 dB lower than the meandered CCS TL for a half-wavelength resonator at 6.0 GHz. But it would be clearer in Section 4.2 that this impediment could be easily overcome by applying negative resistance circuit.

However, for example, the meandered CCS TL of W=30 μm and S = 15 μm posses a better loss characteristic, better slow property, and modest average width in the top layer strip compared to the one of W = S = 30 μm. With the CCS TL of unequal W and S, a passive half-wavelength resonator could be further optimized in respect to the DC-resistance, high-frequency loss, and chip area. But for simplicity and for the same reason about the loss issue, the meandered CCS TL of S = W = 30 μm is employed for designing the prototype active bandpass filter.

For clearness, the guiding characteristics of CCS TL of S = W = 30 μm from 1 GHz to 8 GHz is derived by using the same software-based analysis method described in Chapter 2. Figure 4.1 illustrates the extracted results of the particular CCS-TL design example. From 1.0 GHz to 8.0 GHz, the real part of the characteristics impedance (Z_c), which is the solid line plotted in Fig. 4.1(a), nearly keeps at a constant value of 34.2 Ω. The imaginary part of Z_c is capacitive, ranging from -11.7 Ω to -2.04 Ω. The normalized phase constant shown in solid line in Fig. 4.1(b) illustrates the value of 2.0 at the desired operating frequency. The normalized attenuation constant, which is plotted by the dotted symbol in Fig. 4.1(b), however, shows relatively high loss aspect of the transmission line. In the low frequency limit (1 GHz), the metal thickness employed in the CCS-TL is smaller than the skin depth, thus we observe larger attenuation losses. Figure 4.2 plots the Q-factor of CCS-TL against frequency, showing 2.19, 2.94, and 3.40 at 3.0GHz, 5.0GHz, and 6.53GHz, respectively. Therefore the Q-factors our resonator design are comparable but smaller than those of inductor-based design in [18-20, 22-24].

(a)

(b)
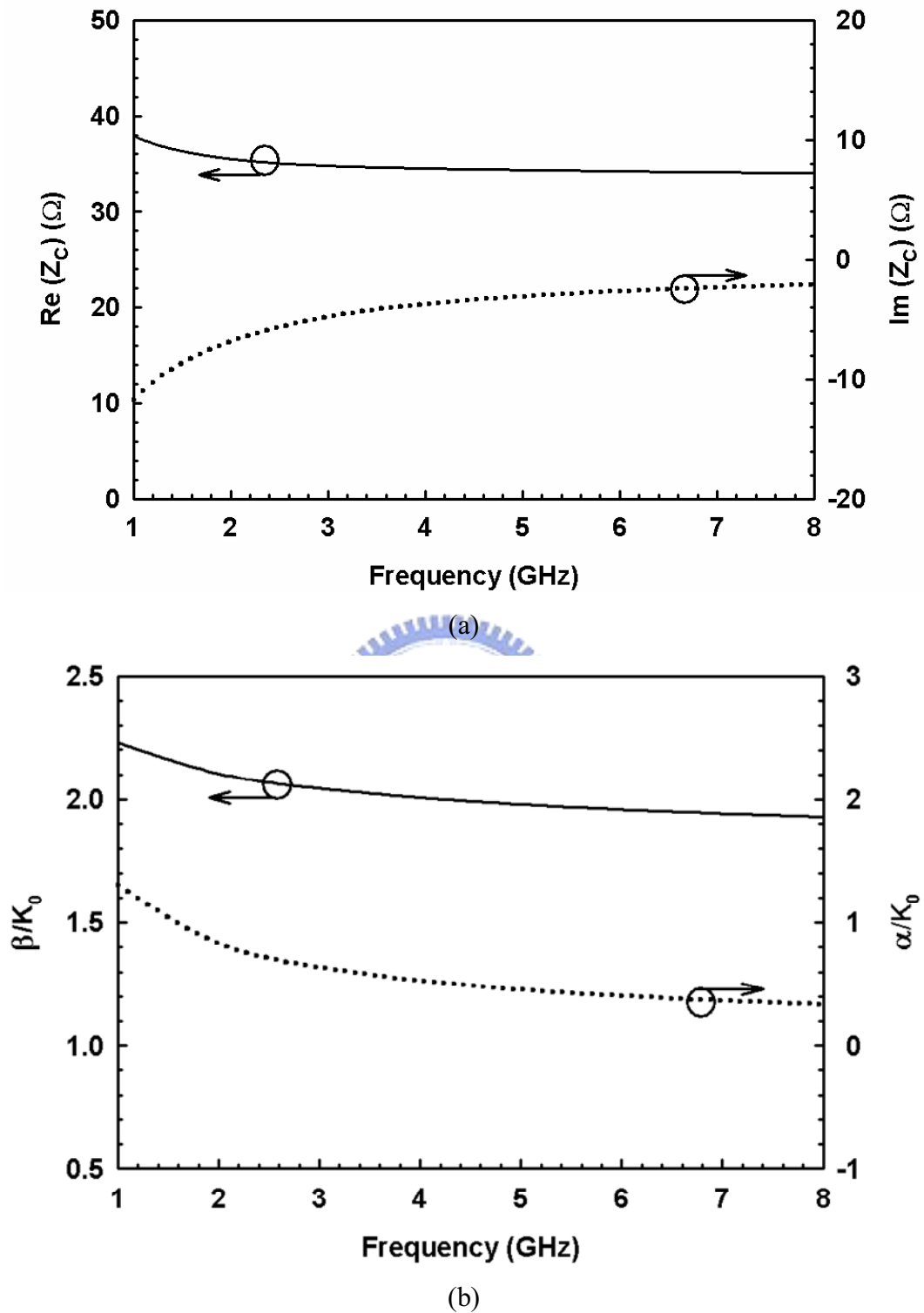
Fig. 4.1 Guiding characteristics of the meandered CMOS CCS TL with W = S = 30 μm, P = 44 μm, and W_h = 40 μm from 1 to 8 GHz. (a) Complex characteristic impedance. (b) Normalized complex propagation constant.
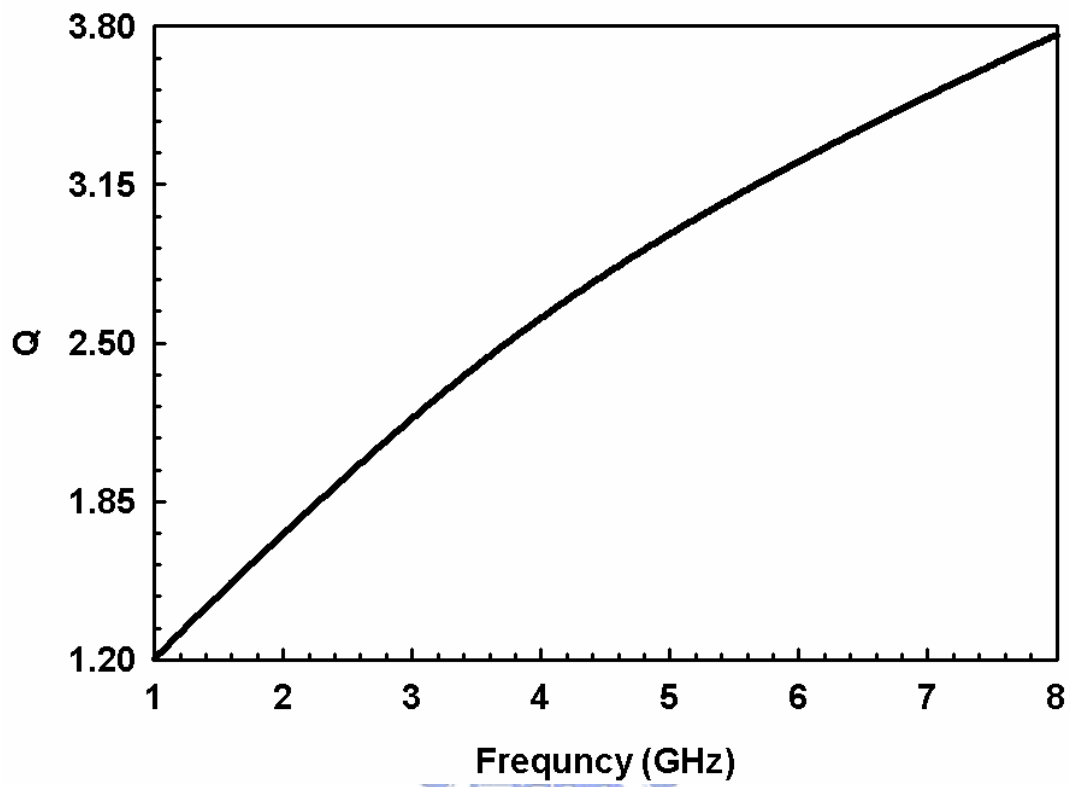
Fig. 4.2 The Q-factor of the CCS TL-based half-wavelength resonator from 1 to 8 GHz.

4.2 Q-Enhanced Monolithic Half-Wavelength Resonator

Figure 4.3 illustrated the concept of a Q-enhanced complementary-conducting-strips (CCS) half-wavelength resonator. A cross-coupled pair, which consists of two identical NMOS transistors, is integrated into a passive CCS-TL based half-wavelength resonator. The Drain terminal of N1 is directly connected to the Gate terminal of N2 and vise versa. Two transistors are biased at the same DC potential (V_G), and the Drain terminals of both N1 and N2 are directly loaded with CCS half-wavelength resonator, forming a new composite resonator.
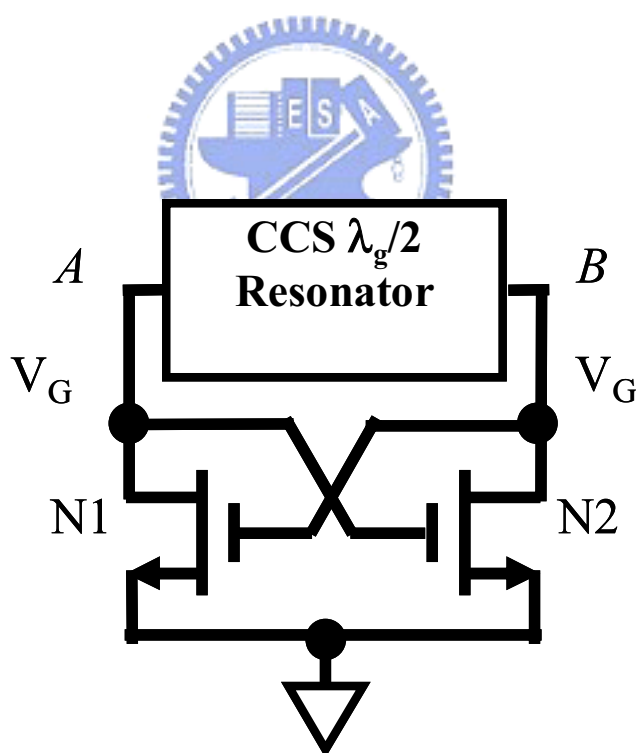
Fig. 4.3 Q-enhanced CCS half-wavelength resonator incorporating a NMOS cross-coupled pair.

Applying to conventional filter synthesis flow, the active resonator will be excited single-endedly, not differentially, both common-mode and differential-mode signals will excite in the active resonator structure. Part (a) and (b) of Fig. 4.4 illustrate the equivalent circuits for differential-mode and common-mode excitations, respectively. When a differential-mode signal transmits into a cross-coupled NMOS transistors pair and establishes a positive feedback, a virtual ground is formed at the symmetric plane rendering a negative differential resistance –Rd in Fig. 4.4(a) with magnitude approximately equal to the inverse of transconductance of the cross-coupled pair [73]. On the other hand, the capacitance across the resonator is approximately half of the combined capacitance ($C_{gs}+C_{gd}$).

Since the potentials on the Drain and Gate terminals of the NMOS are equal under a common-mode excitation, the NMOS acts as a Gate-Drain-connected diode. Therefore two parallel RC networks are loaded with both sides of the half-wavelength resonator. The shunt resistance R_c shown in Fig. 4.4(b) represents the small signal resistive loss of the transistor operated in the saturation region. To make proper operation of active bandpass filter, the differential-mode must prevail over the common-mode in the passband. Since the cross-coupled pair can amplify the differential-mode signal and attenuate the common-mode signal, such circuit characteristic can increase the common-mode rejection of the proposed Q-enhanced resonator, and relax the issue on symmetrical layout of the resonator during the filter integration.
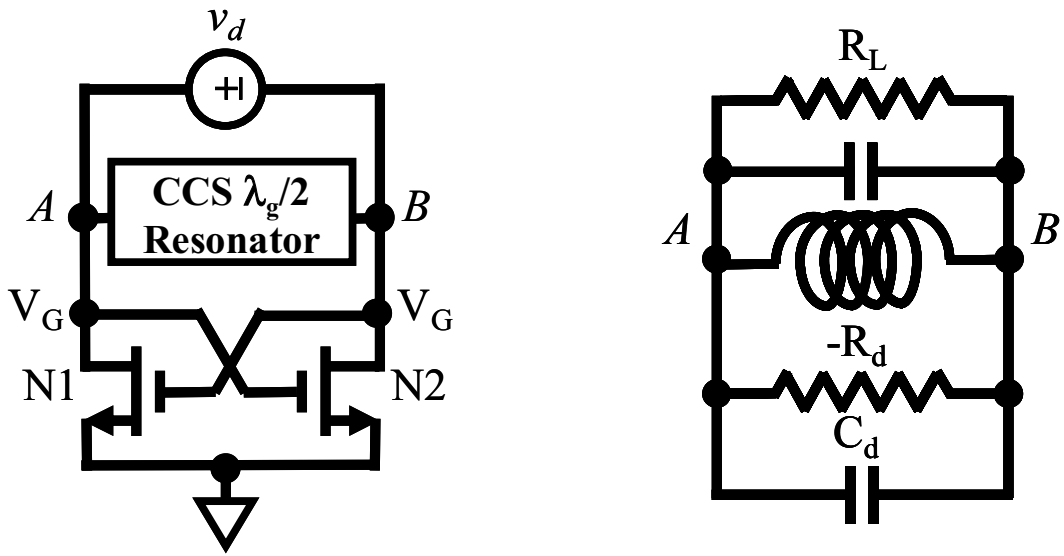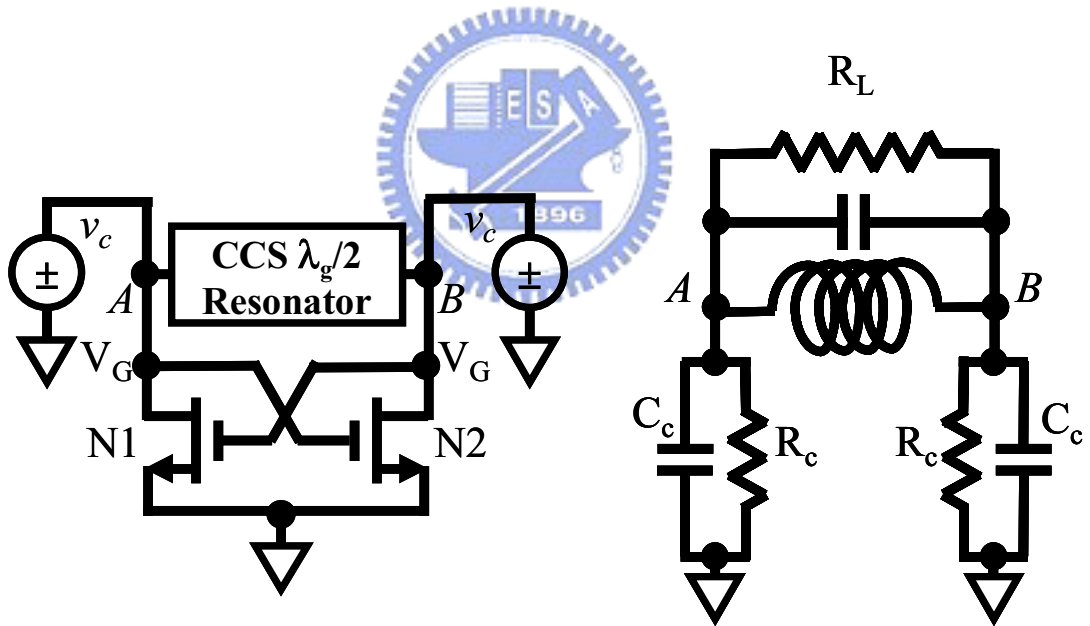
Fig. 4.4 Small signal analyses of the Q-enhanced half-wavelength resonator. (a) Differential-mode analysis. (b) Common-mode analysis.

Then the complex input impedance under differential-mode excitation was theoretically investigated by using the software, Agilent^{TM} ADS2004A. Through the analysis, the length and width of the two transistors were set at 0.18 μm and 80 μm, respectively. And V_G was isolated from the differential RF signal by RF-choke. The results illustrate that the value of C_d and $-R_d$ were nearly constant from 1.0 GHz to 8.0 GHz, revealing a broadband characteristic of the equivalent active RC circuit. And the total equivalent resistance (R_{equ}) of the differentially driven active resonator can be expressed by

$$R_{equ} = \frac{-R_d \cdot R_L}{R_L - R_d} \tag{4}$$

where R_L represents the loss of the CCS half-wavelength resonator. Because the value of the frequency-dependent R_L increases with increasing frequency, the active resonator tends to become more stable at frequency higher than the resonant frequency. Furthermore, the value of $-R_d$ is inversely proportional to the Drain current of the NMOS transistors [73]. Thus, as shown in Fig. 4.5, V_G can be applied to adjust proper negative resistance for realizing a stable half-wavelength resonator.
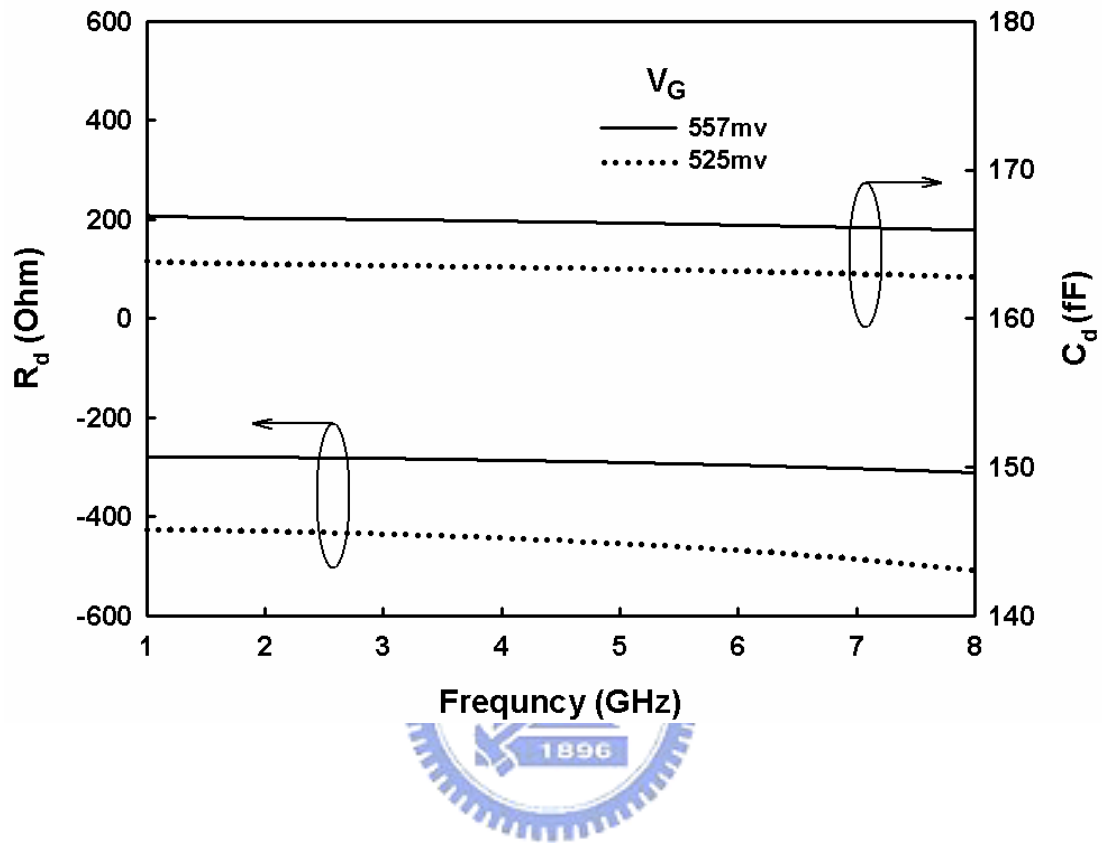
Fig. 4.5. Differential input impedance of a 0.18 μm NMOS cross-coupled pair with length of 0.18 μm and width of 80.0 μm.

The inset in Fig. 4.6 depicts the schematic for extracting the unloaded Q-factor of the active half-wavelength resonator shown in Fig. 4.3. Two tiny capacitors of 0.01 fF formed the electromagnetic coupling between the resonator and loads. Clearly the excitation was single-endedly. The size of the NMOS transistor was the same as that reported in the Fig. 4.6, and the half-wavelength resonator was realized by using the meandered complementary-conducting-strips transmission line (CCS-TL) reported in the Section II.A. As the value of R_L of the CCS half-wavelength resonator and $-R_d$ of the cross-coupled pair biased at 557 mV are 298.4 Ω and -301.34 Ω at 6.53 GHz, respectively. Therefore, according to (1), Fig. 4.6 illustrates a stable active half-wavelength resonator.

The extracted Q-factors shown in Fig. 4.6 follow the definition of the unloaded Q-factor in [74]. Moreover, the magnitudes of the transducer gain of the weakly coupled active resonator are also illustrated in Fig. 4.6. The Q-factor was only 3.40 for the passive CCS half-wavelength resonator. With the active Q-enhanced circuit biased at 525 mV, 538 mV, 549 mV, and 557 mV, the enhanced Q-factors were 9, 15, 39, and 84, respectively. Notably, the resonant frequency of the Q-enhanced resonator was slightly shifted from 6.633 GHz to 6.531 GHz when V_G was increased. Such frequency drift was caused by the increase of C_d shown in Fig. 4.5.
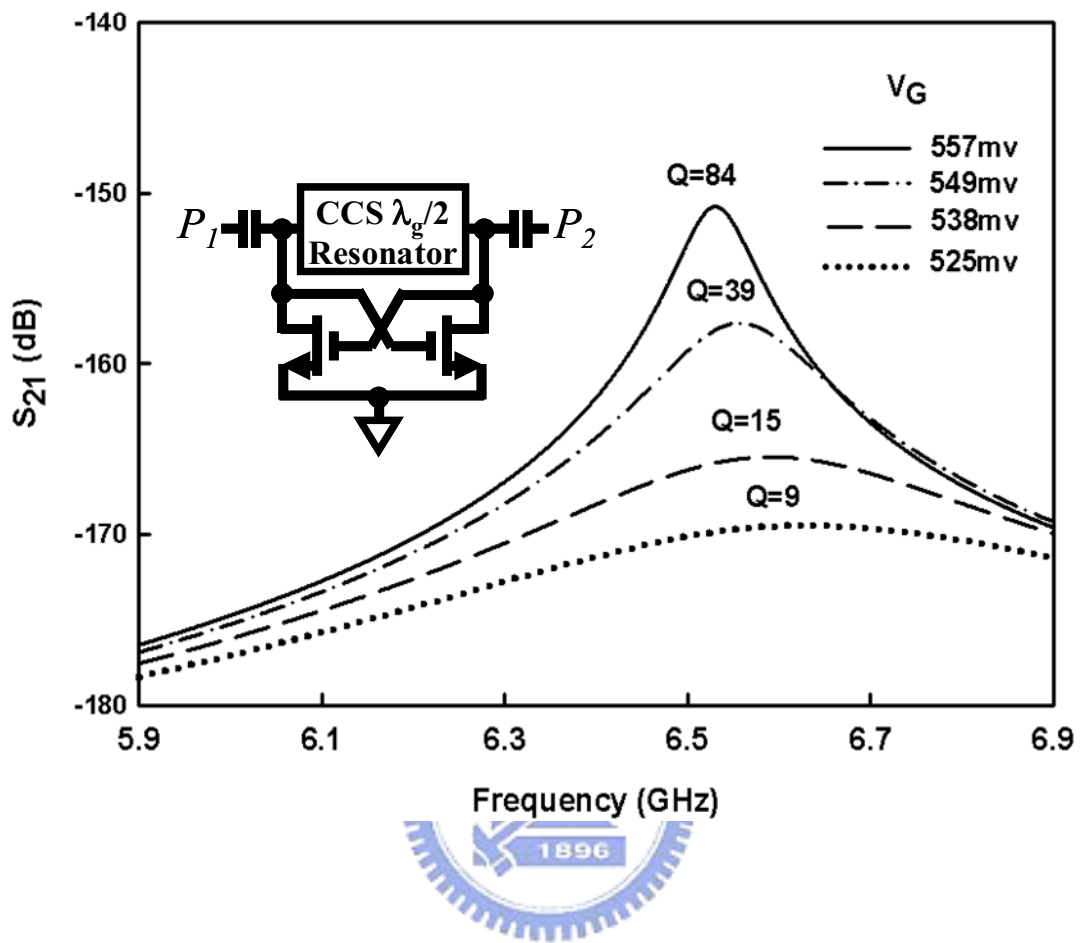
Fig. 4.6 Unloaded Q-factor of Q-enhanced half-wavelength resonator incorporating a 0.18 μm NMOS cross-coupled pair.

4.3 CMOS Transmission-Line based Active Bandpass Filter

Figure 4.7 shows the complete schematic of a second-order bandpass filter (BPF) incorporating the Q-enhanced half-wavelength resonators [29-30]. The J-inverters were realized by series capacitors C_1, C_2, and C_3.The design procedure of the BPF is well documented in [74]. In this practical example, f_c of the BPF was located at 6.02 GHz, and BW was 1.0 GHz with ripple of 0.2 dB. The order of the BPF was two and the reference impedances of two terminals (P_1 and P_2) were 50 Ω. The biasing and tuning networks controlled by V_{tun} provided biasing currents for the NMOS cross-coupled pairs. And these networks were isolated from the CCS-TL resonators by the on-chip spiral inductors as shown in the top of Fig. 4.8. Figure 4.8 also illustrates the die photo of the prototype filter in Fig. 4.7.

The entire active BPF, including the complementary- conducting-strip transmission lines (CCS-TLs), capacitors, inductors, active networks, and pads were fully integrated in a chip area of 1230 µm x 880 µm. The capacitor was realized with the so-called interdigital metal-oxide-metal (MoM) capacitors of top-three metal layers. In the realizations, C_1 was 380 fF with an area of 45.9 µm x 79.8 µm, and C_2 was 220 fF with an area of 41.9 µm x 52.8 µm, respectively. Additionally, the inductance of the on-chip spiral inductors was about 3.0 nH occupied an area of 251 µm x 247 µm.
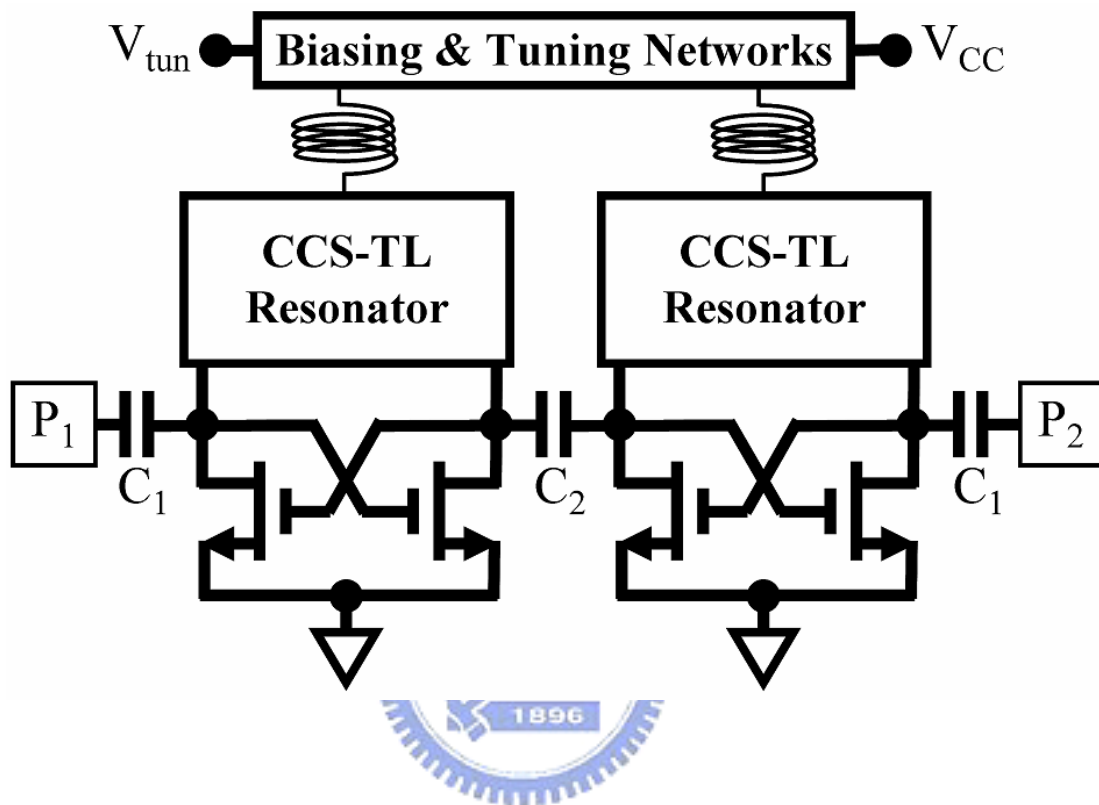
Fig. 4.7 Second-order CMOS transmission-line based bandpass filter.
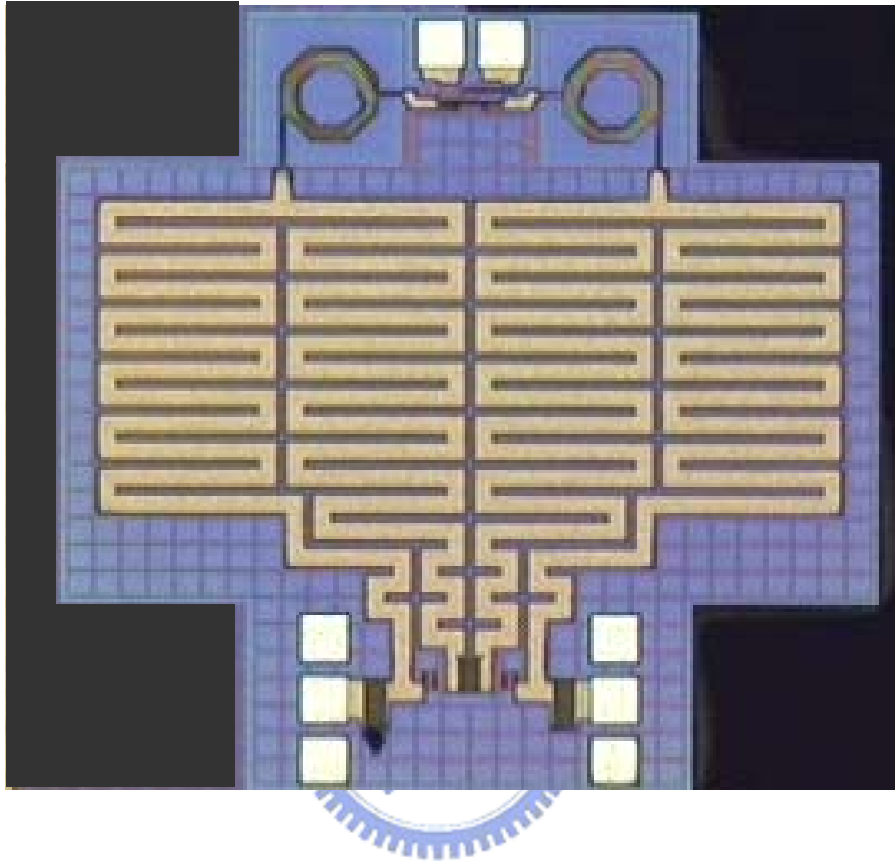
Fig. 4.8 Die photo of the prototype bandpass filter in Fig. 4.7.

The small-signal experiments were performed after the on-wafer short-open-load-through (SOLT) procedures had been conducted by the vector network analyzer (VNA), Agilent[TM] E5091A. In the measurements, the prototype shown in Fig. 4.7 was biased by a supplying voltage (V_{CC}) of 1.8V with a current consumption of 3.0 mA. The value of V_{tun} and the power level of input signals were set at 1.0V and -20dBm, respectively. Additionally, the measured result was compared with simulations performed by Agilent[TM] ADS2004A. Before the simulation, all the passive components including capacitors, inductors, and CCS-TL were characterized by Ansoft HFSS[TM]. The BSIM3 V3.2.4 based RF models used for active devices were provided by the foundry. Figure 4.9(a) shows the comparisons from 3.0 GHz to 8.0 GHz, revealing good agreements between the simulated and measured data. The slight mismatch shows the capacitive coupling between the two Q-enhanced half-wavelength resonators were well controlled through the J-inverter, C_2, and parasitic coupling through the lossy substrate was not server owing to the good electromagnetic shield from the meshed ground plane of CCS TL. On the other words, the CCS-TL can effectively confine the electromagnetic propagations and eliminate the un-wanted coupling of the adjacent signal lines in the compact layout.

The measured results of two-port scattering parameters based on the 50 Ω-system lead the following observations. The center frequency of the second-order BPF is 6.02 GHz, and the insertion-loss is about 2.2 dB from 5.38 GHz to 6.65 GHz. The bandwidth is about 1.14 GHz (5.26 GHz to 6.40 GHz) with a return-loss of 7.64 dB. Two reflection zeros are identified at 5.47 GHz and 6.20 GHz. Additionally, the prototype can reject the low-side signal about 28.18 dB at 4.0 GHz and the high-side signal about 18.33 dB at 8.0 GHz. The superiors-mode of the prototype, which is observed in Fig. 4.9(b), is suppressed about 16.67 dB at 15.25 GHz. The unobvious

superiors-mode reflects that fact that the loss of the composite resonator is not compensated at the corresponding frequency. In other words, for the boundary condition set by the CCS-TL resonator at 15.25 GHz is unable to excite the cross-coupled circuit to generate differential negative resistance for loss compensation.

Based on the same measurement setting with V_{tun} set at 1.2 volt, as illustrate in Fig. 4.10(a), the center frequency of the prototype bandpass filter is 5.97 GHz. The passband gain is about 0.561 dB from 5.38 GHz to 6.56 GHz. The return-loss is 9.55 dB with a bandwidth of 870 MHz, from 5.5 GHz to 6.37 GHz. The two reflection zeros are identified at 5.47 GHz and 6.125 GHz which almost the same as those observed when V_{tun} was set at 1.0 volt. Besides, the stopband rejections also remain the same, 27.95 dB at 4.0 GHz and 18.24 dB at 8.0 GHz, respectively. Fig. 4.10(b) depicts the corresponding superiors-mode suppression is about 20.31 dB at 15.8 GHz. The current consumption increases slightly from 3.0 to 4.0 mA. In summary, the center frequency, 3-dB frequency, and stopband rejections are almost insensitive to the changes of tuning voltage, V_{tun}. Thus, the passband gain of the prototype bandpass filter could be controlled independent form the other filter characteristics.

Comparing the measured and simulate results when V_{tun} set at 1.2 volts, the simulated passband gain is a little bit larger than the measured one at the high side of passband edge. This could due to the insufficiency of the circuit model used for emulating the characteristics of the active devices especially at resonance frequency. Moreover, the measured reflection coefficient is larger than 0 dB from 6.65 to 7.45 GHz which is also observed in the simulated result, from 6.5 to 7.9 GHz. This phenomenon could introduce potentially instabilities and a further analysis would be performed in Section 4.6.

(a)
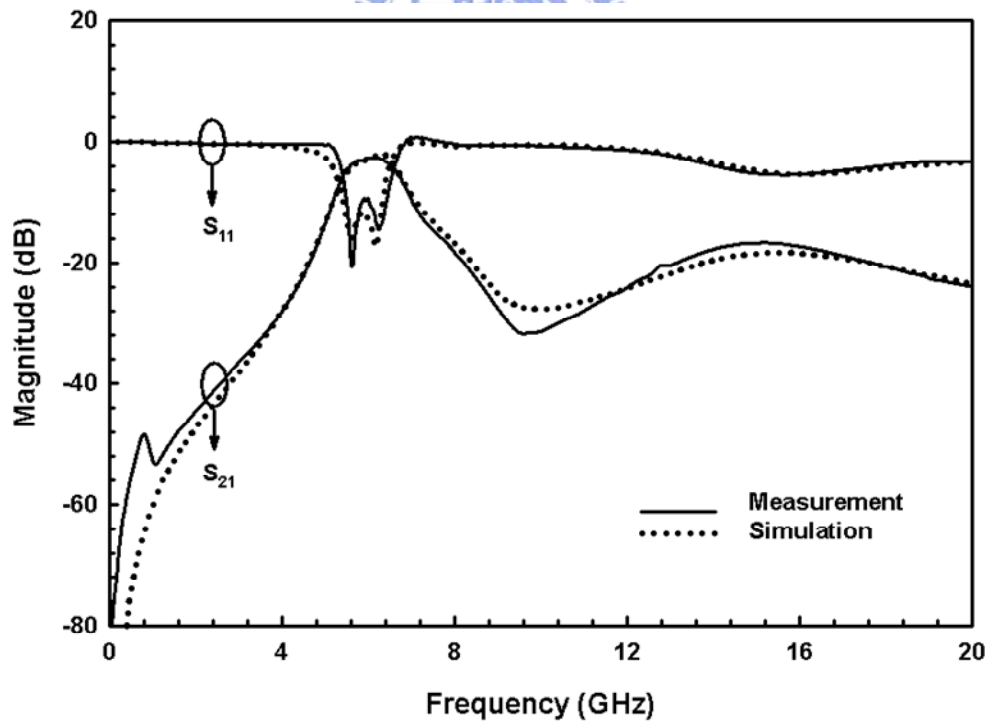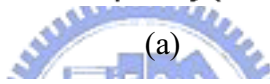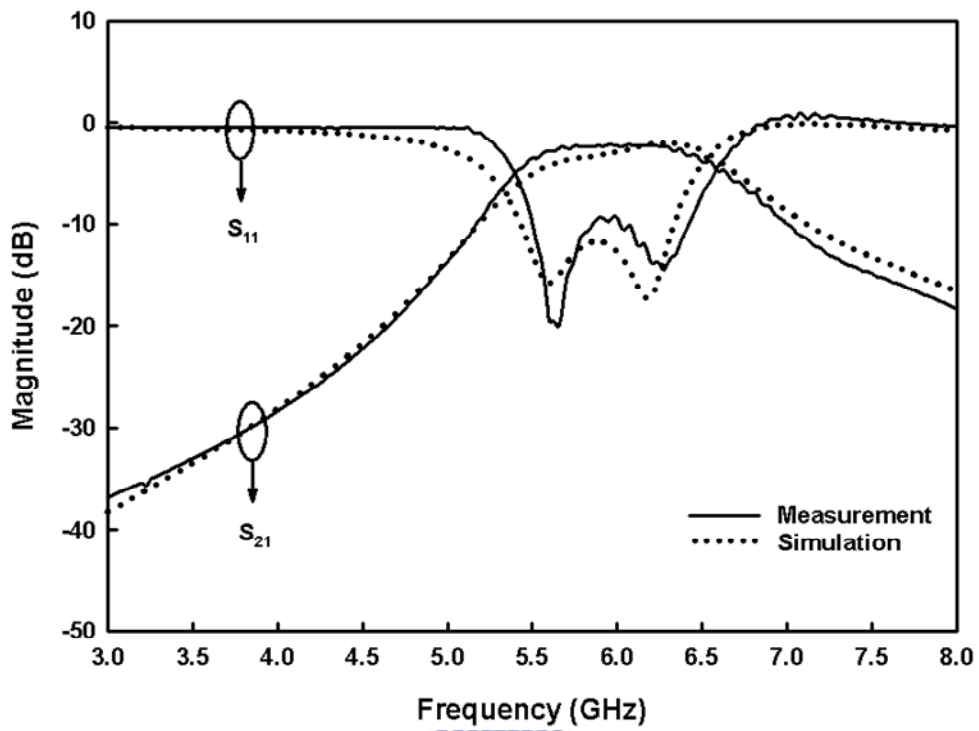
(b)

Fig. 4.9 Comparison of measured and simulated transmission and reflection characteristics of the prototype active bandpass filter when V_{tun} set at 1.0 volt. (a) 3 to 8 GHz. (b) DC to 20 GHz.
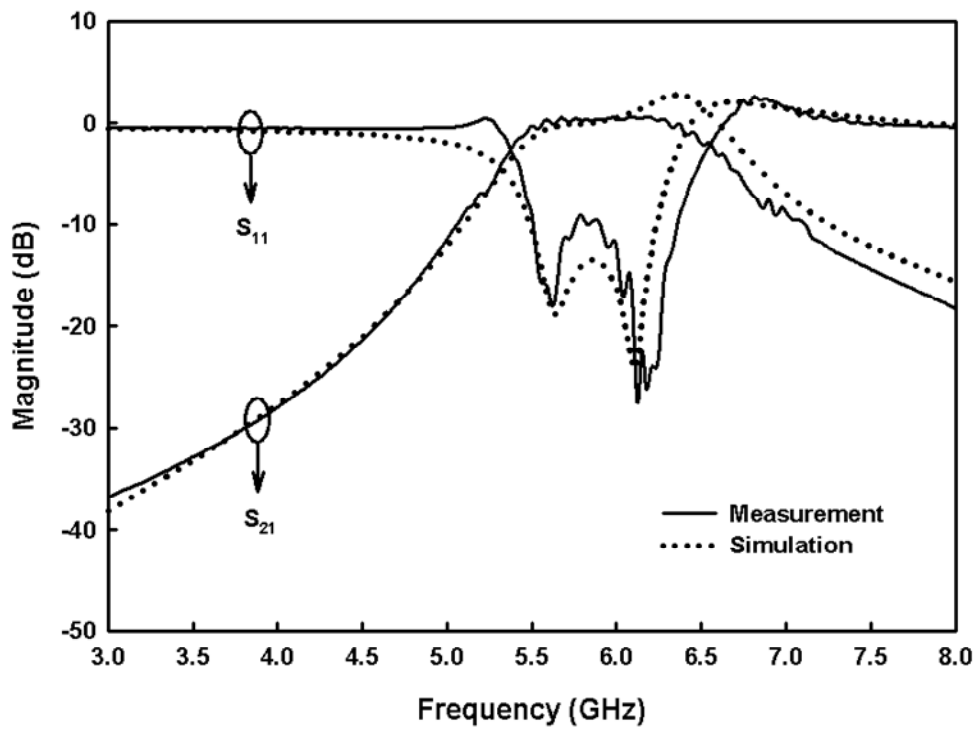
(a)
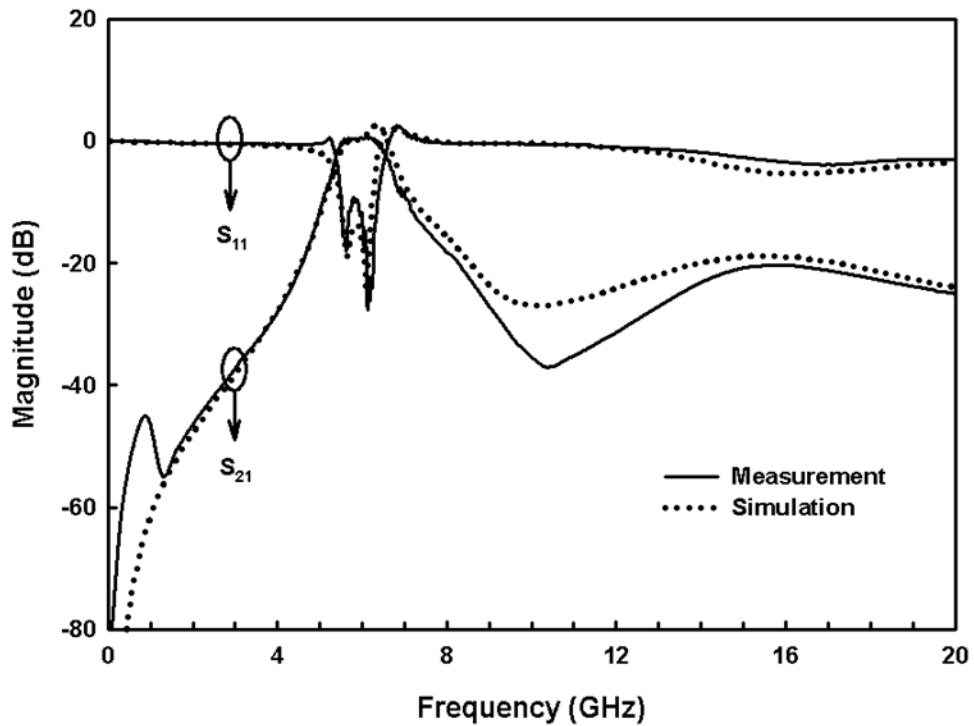
(b)

Fig. 4.10 Comparison of measured and simulated transmission and reflection characteristics of the prototype active bandpass filter when V_{tun} set at 1.25 volt. (a) 3 to 8 GHz. (b) DC to 20 GHz.

4.4 Nonlinear Characteristics

The nonlinear characteristics of the prototype with V_{tun} equal to 1.0 volt had also been investigated by measuring the input third-order intermodulation point (IIP_3) and the 1-dB compression point (P_{1dB}) when the. For the measurement of P_{1dB}, the signal generator, Agilent^{TM} E8267D, provided an input continuous wave (CW) at 6.02 GHz, and the spectrum analyzer, Agilent^{TM} E4440A, was applied to observe the output signals of the prototype. For the measurement of IIP_3, two signal generators were applied to generate two fundamental frequencies of f_1 and f_2 equal to 5.795 GHz and 5.805 GHz, respectively. Before performing the measurements, the testing system which includes the connectors and cables were calibrated. The measured and simulated results, as shown in part (a) and (b) of Fig. 4.11 indicate the measured input power levels for P_{1dB} and IIP_3 are -15.2 and -9.6 dBm. Besides the simulated values are -17.8 dBm and -10.69 dBm revealing an average difference of less than 1.8 dB.

To investigate the IIP_3 characteristics of passband intermodulation distortion (IM_3) caused by stopband signals, the same circuit simulation scheme was adopted. For both the f_1 and f_2 signals originating from upper stopband, f_1 was set at 7.5 GHz and f_2 was swept for 8.5 to 9.7 GHz. Therefore the resultant IM_3 frequency ($2f_1-f_2$) ranged from 5.3 to 6.5 GHz within the passband of the prototype filter. Similarly, for both signals originating from lower stopband, f_2 was set at 7.5 GHz and f_1 was swept for 4.7 to 3.5 GHz, respectively. The simulated IIP_3 caused by upper and lower stopband signals are illustrated in Fig. 4.12(a) and (b). As expected, the trends of both cases illustrate that the interfering signals closer to the passband would introduce a larger intermodulation products with a lower value of IIP_3. The minimum values are -7.71 dBm and -6.6 dBm for the upper and lower cases and are both larger than the one introduced by passband f_1 and f_2 signals. Further increase the distance between f_1 and f_2 signals would

result in a higher IIP_3 value. The highest values are -2.23 dBm and -0.86 dBm for the upper and lower cases. Since the stopband rejection is getting larger when f_1 or f_2 signal is farther away from the passband, therefore the generated intermodulation products would become smaller resulting a higher value of IIP_3 as well.
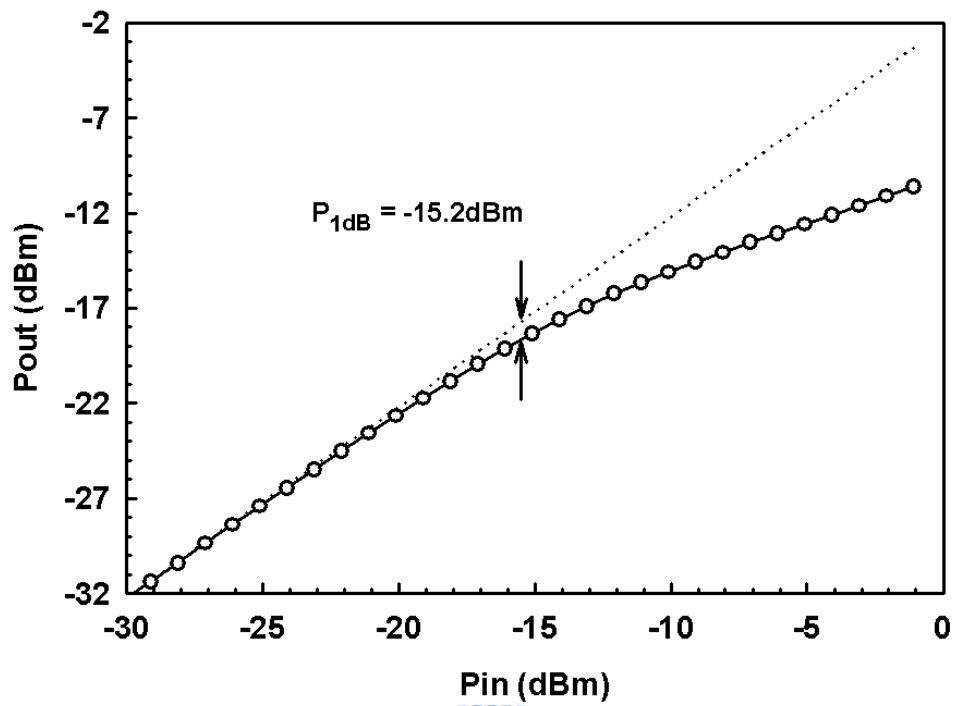
(a)
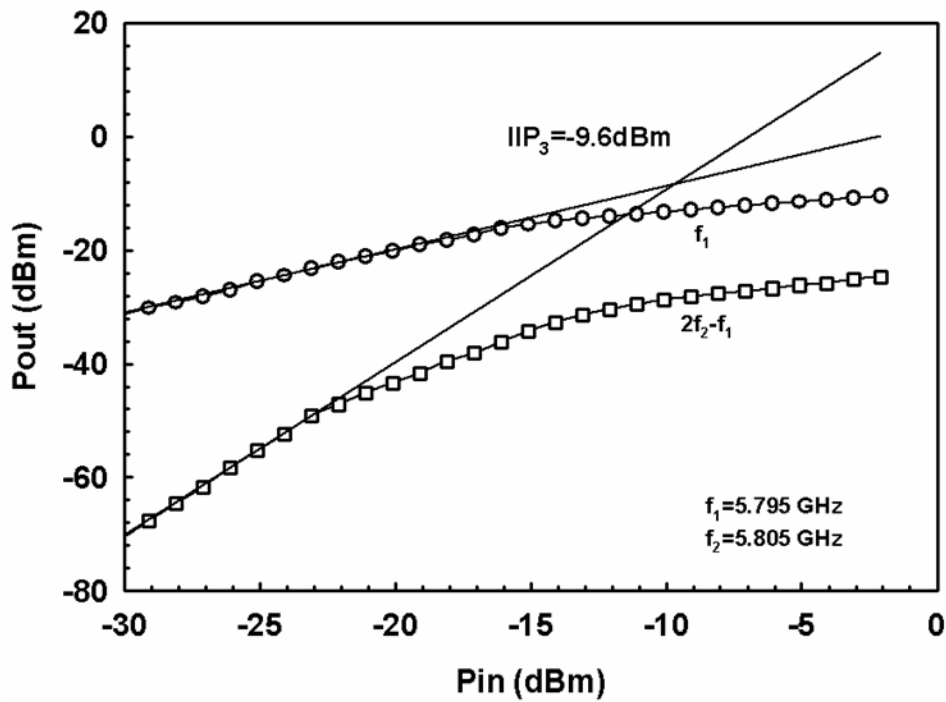
(b)

Fig. 4.11 Nonlinear characteristics of the active bandpass filter prototype. (a) 1-dB compression point measurement of f_0 equal to 5.8 GHz (b) Measured third-order intermodulation distortion of f_1 and f_2 equal to 5.795 GHz and 5.805 GHz, respectively.

(a)
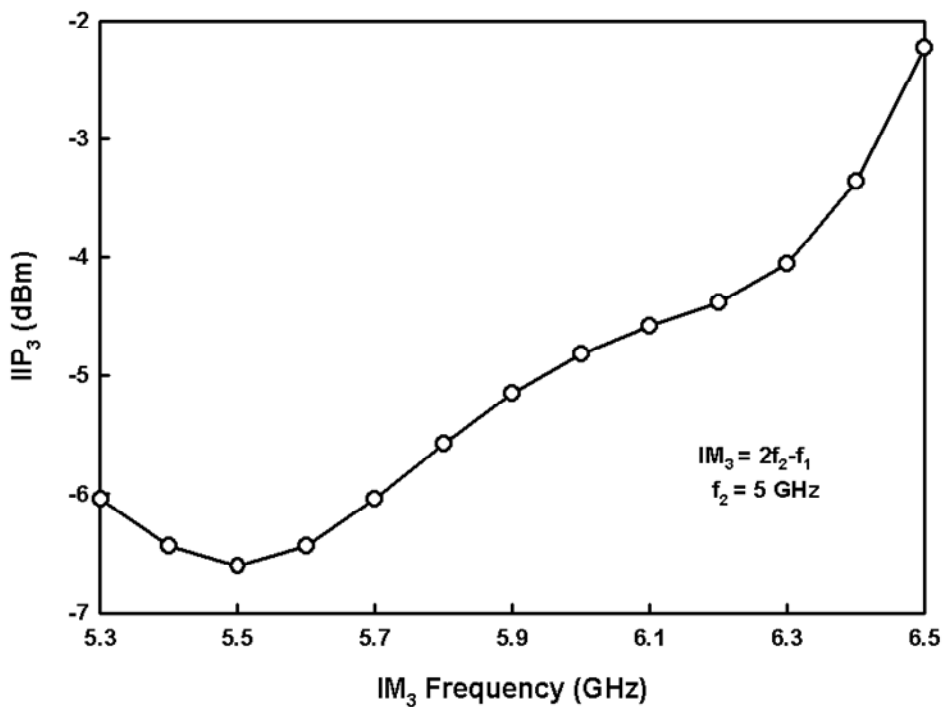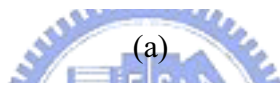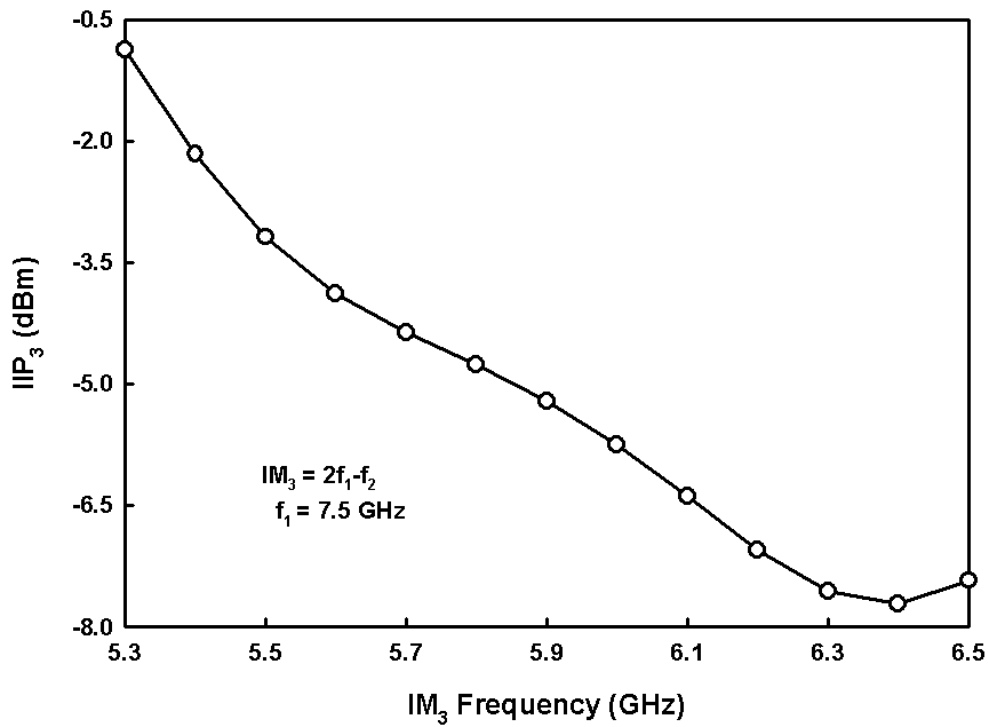
(b)

Fig. 4.12 Input third-order intermodulation intercept point (IIP$_3$) characteristics when passband intermodulation distortion (IM$_3$) cause by signals from (a) upper stopband with f$_1$ fixed at 7.5 GHz, and (b) lower stopband with f$_2$ fixed at 5 GHz.

4.5 Noise Analyses

In this section, the passband noise figure of the prototype active bandpass filter incorporating cross-coupled pair circuit was investigated. An equivalent noisy two port network and analytic expression relating the input referred noise figure are presented and validated. Then the effects of device sizes and operation conditions on the filter noise performance were analyzed as well. Finally a design trade off curve was derived and provides physical explanations in attending minimum noise-figure values of the proposed active filter.

4.5.1 Equivalent Noise Two Port Network

Experimental results in Fig. 4.9 indicate that the prototype filter behaves like a passive one with an insertion loss of 2.2dB. According to the text-book definition, the noise figure of a passive two-port network is equivalent to the inverse of its available power gain [75]. However, the proposed bandpass filter, as depicted in Fig. 4.7, comprises of complementary-conducting-strip transmission lines (CCS-TL) and differential NMOS cross-coupled pairs. The cross-coupled pairs not only provide negative resistance to enhance the quality factor (Q-factor) of the resonators, but also produce the noise simultaneously. Therefore, the noise contributions from the transistors need to be incorporated into the noise figure calculation of the prototype filter. The noise characteristics of a NMOS cross-coupled pair had been well documented in [76-77]. The differential output noise current spectral density of a NMOS cross-coupled pair is equivalent to the summation of thermal noise generated in the channels of two NMOS transistors [77]. Furthermore, the channel noise of a NMOS transistor operating in saturation can be quantified by an equivalent noise

current between the Drain and Source terminals:

$$\bar{i}_n^2 = 4k_0 \mathrm{T} \gamma g_m \tag{5}$$

where k_0, g_m, and γ are Boltzmann's constant, the transconductance, and channel noise coefficient of a NMOS transistor, respectively [78-79].

Figure 4.13 illustrates the two-port noisy network consists of an ideal bandpass filter and a noise current source. The available gain (G_A) of the ideal passive bandpass filter is derived based on the transmission coefficient [80], and the noise current source at the output of the passive filter represents the total noise current generated by the two NMOS cross-coupled pairs. The definition and analytical expression for deriving the input referred noise figure of the proposed noisy two-port network are expressed as following:

$$\mathrm{NF} \equiv \frac{\text{Total available noise power at output}}{\begin{array}{c}\text{Available noise power at output due to thermal noise form}\\ \text{the input termination } \mathrm{R}_{\mathrm{S}}\end{array}} \tag{6}$$

$$\equiv \frac{k_0 \mathrm{T} + (2.0 \times \bar{i}_n^2 \times \mathrm{R_L})}{k_0 \mathrm{T} \times \mathrm{G_A}} \tag{7}$$

where the bandwidth had been normalized to 1 Hz.
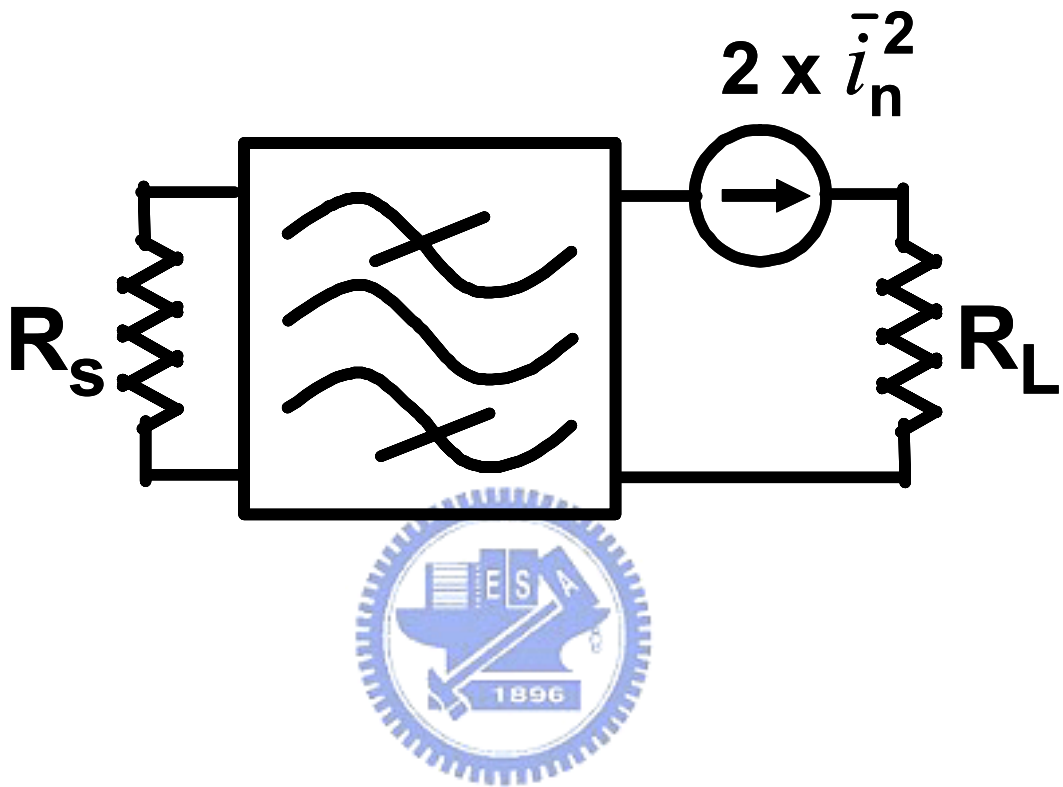
Fig. 4.13 The equivalent noisy two-port network of the prototype bandpass filter with a 2.2-dB insertion loss.

4.5.2 Validity Check and Design Trade-offs

To demonstrate the feasibility of the proposed noisy network, the theoretical analyses were conducted with the two-port network illustrated in Fig. 4.13. The geometrical size of transistor had been reported in Section 3.2, and the corresponding value of g_m derived according to the definition in [79] was 8.872 mS. The γ value extracted from the small signal noise analysis of the NMOS transistor was 1.012 at 6.0 GHz [79]. Thus, the total noise current spectrum density of the NMOS cross-couple pairs was 6.436e-22 A^2/Hz at 298.15 K. The calculated NF of the proposed bandpass filter after following the procedures described in (5) was 11.38dB. Additionally, the calculation results from 5.5 GHz to 6.0 GHz were compared with those of the simulations and experiments, as illustrated in Fig. 4.14, revealing a difference of less than 7.2% on the noise analyses. The measurements, which were undertaken using the Agilent[TM] noise figure analyzer N8974A, reveal that the NF of the prototype was about 12.36 dB at 5.5 GHz, which was slight decreased to 10.92 dB at 5.8 GHz. Simulation results indicate that the NF of the proposed bandpass filer was 12.30 dB and 11.40 dB at 5.5 GHz and 6.0 GHz, respectively. These good agreements indicate that the proposed noisy network is valid for predicting the NF of the bandpass filter shown in Fig. 4.9.

Furthermore, the noise figure (NF) of the proposed bandpass filter with different transistor width was also theoretically analyzed by following the same analytical procedures mentioned above. Through the analyses, the characteristics of the bandpass filter, including the insertion-loss, reflection coefficient, and bandwidth, were identical to those reported in the Fig. 4.9.
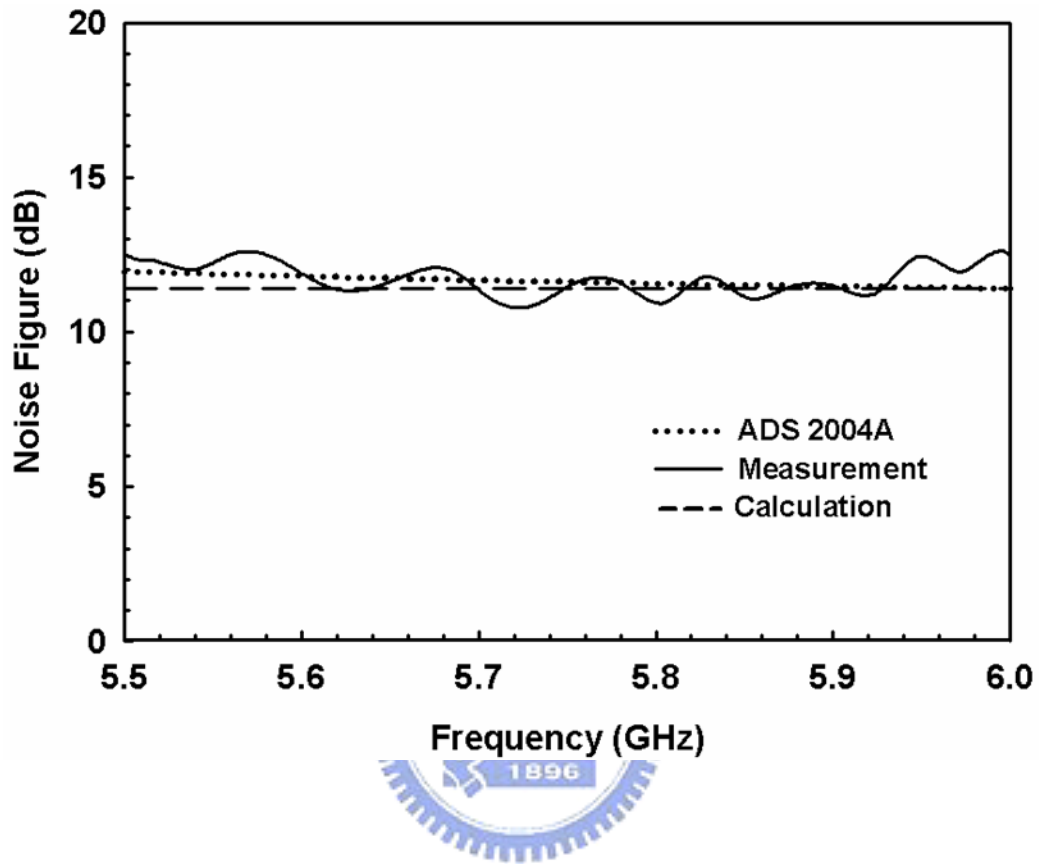
Fig. 4.14 The simulation, measurement, and calculation results of the input referred noise figures of the proposed bandpass filter.

Figure 4.15 and 4.16 plot the statistical results, from which the following observations can be drawn. The value of γ, denoted by the curve with square symbols in Fig. 4.16 is highest at 1.63 with the smallest transistor width of 10.0 µm. However the γ can be reduced and kept with a constant value of 1.10 when the width is larger than 80 µm. Conversely, g_m is increased from 5.52 mS to 11.12 mS, corresponding to the increase of transistor width from 10 µm to 160 µm. Since the equivalent small-signal resistor between the Drain and Source terminals increases due to the Non-quasi-Static (NQS) effect [81], the higher value of g_m is required to reduce the ohmic loss from the CCS-TLs and the resistive loss in the channels of transistors. As depicted in (3), the noise current of the transistor is proportional to the product of g_m and γ. Consequently, the NF, denoted by the curve with triangular symbols in Fig. 3.17, is 11.38 dB, corresponding to the transistor width of 10µm. Increasing the width of the transistor from 10 µm to 20 µm causes the NF linearly reduced to its minimum value of 9.82 dB. However, using the transistor width larger than 20 µm in the bandpass filter increases the resultant NF. These observations demonstrate the design trade-off for minimizing the NF of the proposed bandpass filter.
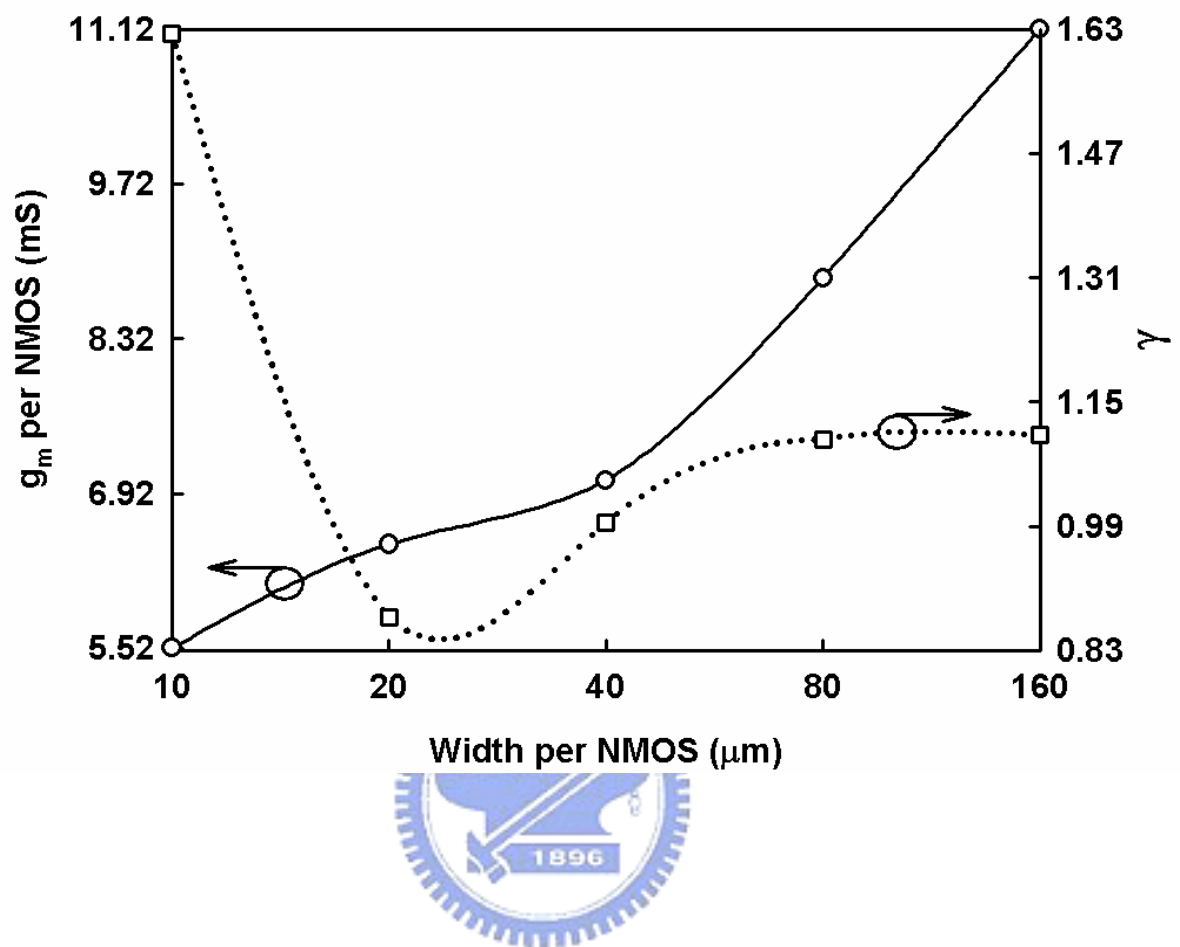
Fig. 4.15   Theoretical values of g_m and γ for each NMOS transistor of different width used for noise prediction for the proposed bandpass filters.
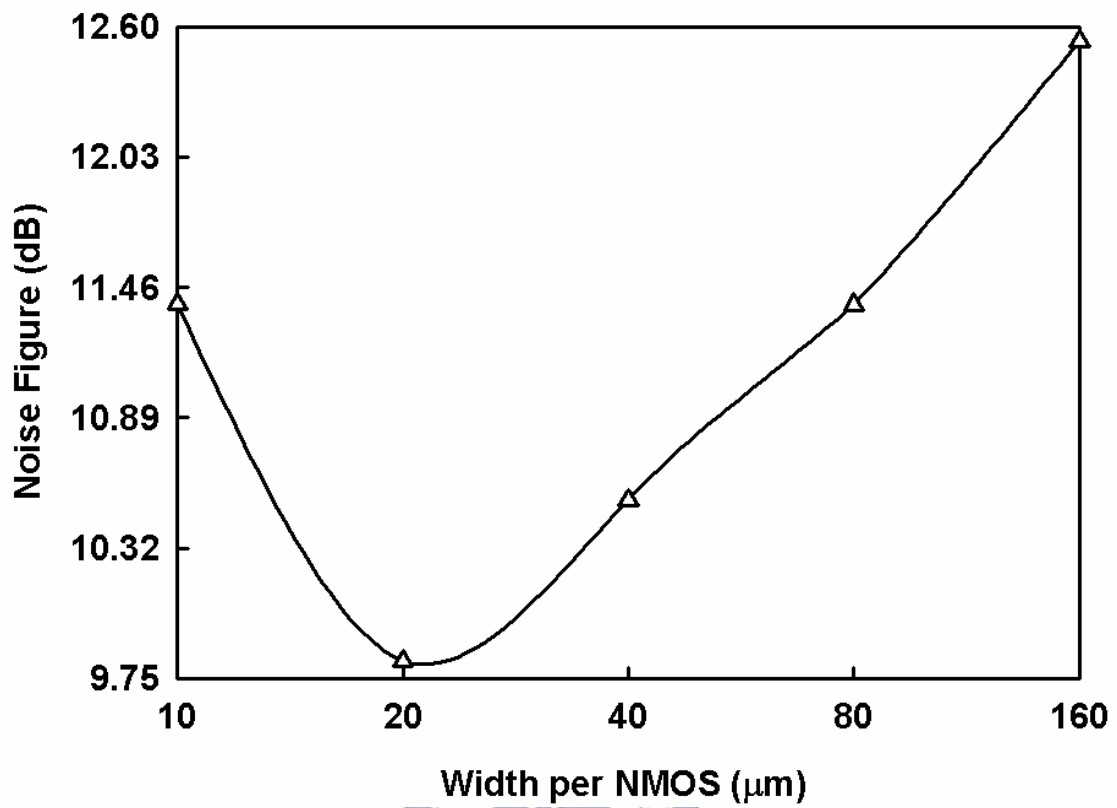
Fig. 4.16   Theoretical predictions of input referred noise figures for the proposed bandpass filters with different transistor widths.

4.6 Stability Analyses

The complete criteria of a unconditionally stable two-port network are : 1) the system be stable or for one specific set of passive terminations (the Rollett's proviso) and 2) the impedances seen looking into either port of the two-port always have a positive real part no matter what passive impedance terminates the other port [82-84]. Many convenient stability parameter tests based on the second requirement have been developed [83, 85-89]. However, applying a stability parameter test without satisfying the proviso could incorrectly predict the result for microwave circuit designs [91-94]. For example, the criteria for oscillation start up among a negative resistance device and a resonator, the magnitude of round-trip reflection coefficient larger than one at resonant frequency, could fail in some cases [93-94]. Since the stability or instability depends on whether the terminate two-port system has right half-plan poles Thus, the analysis of the proviso of the proposed active bandpass filter terminated by a set of 50 Ω resistances was first performed. Then an unconditionally stability test using μ and ν parameters is applied to indicate the geometrical relations between the stability circle and unit smith chart from DC to 20 GHz [86-87].

As demonstrated in [93], the number of the right-half-plan (RHP) poles of a terminated microwave system could be predicted according to the Nyquist theorem, the number of the encirclement of +1 point in a Nyquist plot. In the particular cases, the reference place is chosen at P1 of the proposed active bandpass filter with either port terminated with 50-Ω resistance. The products of the input and output reflection coefficients at the reference plan were evaluated by using the Agilent^{TM} ADS2005A circuit simulator from 1 MHz to 20 GHz. Figure 4.17(a) and (b) illustrate the analyzed results when V_{tun} set at 1.0 and 1.2 volt. Note that these data are only half of the

Nyquist plots for frequencies larger than zero, and the other half for frequencies less than zero could be derived by mirroring the fist part around the x axis. At 1 MHz, both the traces begin around the x axis with radiuses less unity then travel in clockwise direction till 20 GHz. As could be observed, the products of input and output reflection coefficients of both cases not enclose the +1 point from 1MHz to 20 GHz. Thus, when V_{tun} set at 1.0 and 1.2 volt, the proposed active bandpass filer terminated with a set of 50-Ω resistances are free from oscillations.
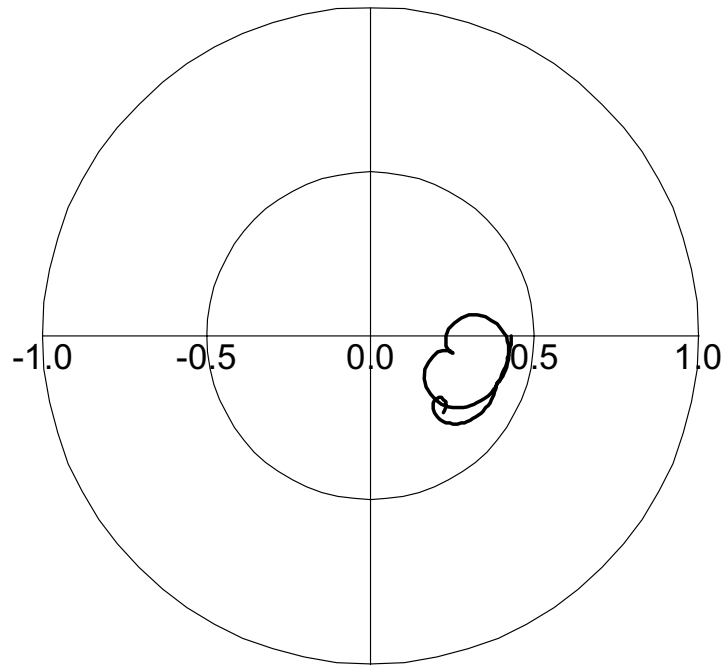
freq (1.000MHz to 20.00GHz)

(a)
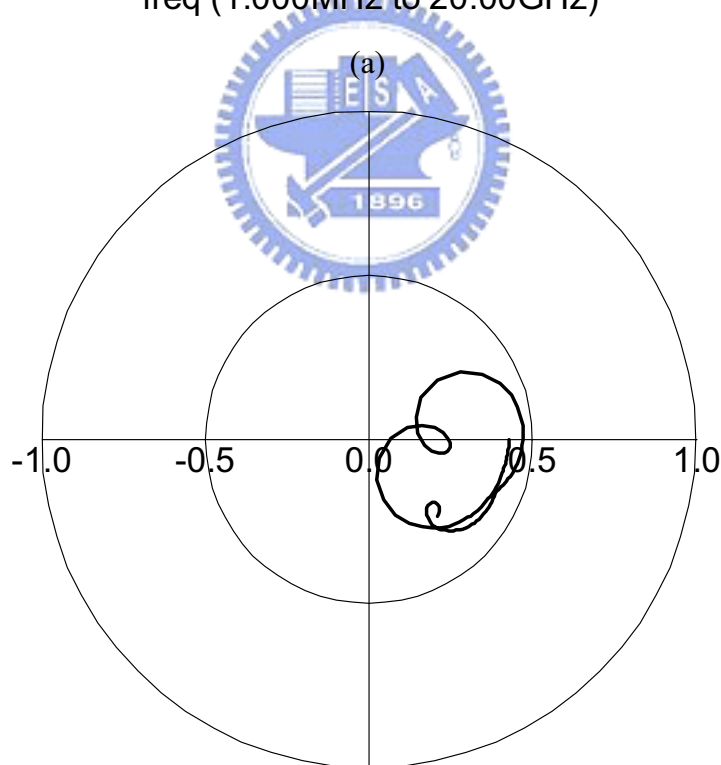
freq (1.000MHz to 20.00GHz)

(b)

Fig. 4.17 The Nyquist plots against frequency from 1MHz to 20 GHz of the prototype active bandpass filter when V_{tun} set at (a)1.0 volt, and (b) 1.2 volt.

Since there is no RHP poles within the two network terminated with a set of 50 Ω resistances, the unconditionally stable test of $\mu > 1$ against frequency from DC to 20 GHz could be further applied. The μ parameter test results of the prototype active bandpass filter with V_{tun} set at 1.0 and 1.2 volt are shown in Fig. 4.18 and 4.19. In addition, the ν parameter is also calculated for indicating the geometrically relation between the stability circle (SC) and unit smith chart (USC) based on the method described in [95]. For clearness, the magnitude of both μ and ν parameter from 5 to 10 GHz are shown as the insets of Fig 4.18 and 4.19 and the accompanying table summarizes the relation between μ and ν over a specific range of frequency. Regarding the prototype filter with V_{tun} set at 1.0 volt, the unconditional stable spectrum ranges from DC to 6.5 GHz, containing the entire passband of the filter, and upper stopband from 8.7 GHz to 20 GHz. When $0< \mu <1$, the stable region of Γ_s covers most of the unit smith chart including the 50 Ω, as further illustrated in part (a) and (b) of Fig. 4.20. Regarding V_{tun} set at 1.2 volt, the unconditionally stable spectrum shrinks but the condition of absolutely unstable never occurs. When $-1< \mu <0$, the 50 Ω termination is excluding from the stable region in Γ_s from 6.5 to 7.9 GHz, exterior to the passband of the particular design. The corresponding input stability circles are shown in Fig. 4.21. Which reflects the fact that the simulated reflection coefficients are larger than 0 dB over the specific range of frequency. However, the Nyquist plot of this design demonstrates the circuit is stable under a set of 50-Ω terminations. Because the stability parameter tests only determine whether or not the input impedance of the network are positive real, and this is not sufficient for insuring whether the system has RHP poles. Nevertheless, in practice care should be exercised as not to cause any potentially instability by properly choosing a set of terminations within the stable region.

70

Frequency (GHz)	Condition		Stability	50Ω ∈ Stable Region
< 5.4	|v|>|µ|>1	µ>0, v<0	Unconditional	Yes
5.4 ~ 6.5	|v|>|µ|>1	µ>0, v>0	Unconditional	Yes
6.5 ~ 7.4	|v|>1>|µ|	µ>0, v>0	Conditional	Yes
7.4 ~ 8.7	|v|>1>|µ|	µ>0, v<0	Conditional	Yes
> 8.7	|v|>|µ|>1	µ>0, v<0	Unconditional	Yes

Fig. 4.18 The µ and v stability parameters against frequency from DC to 20 GHz of the prototype active bandpass filter when V_{tun} set at 1.0 volt.
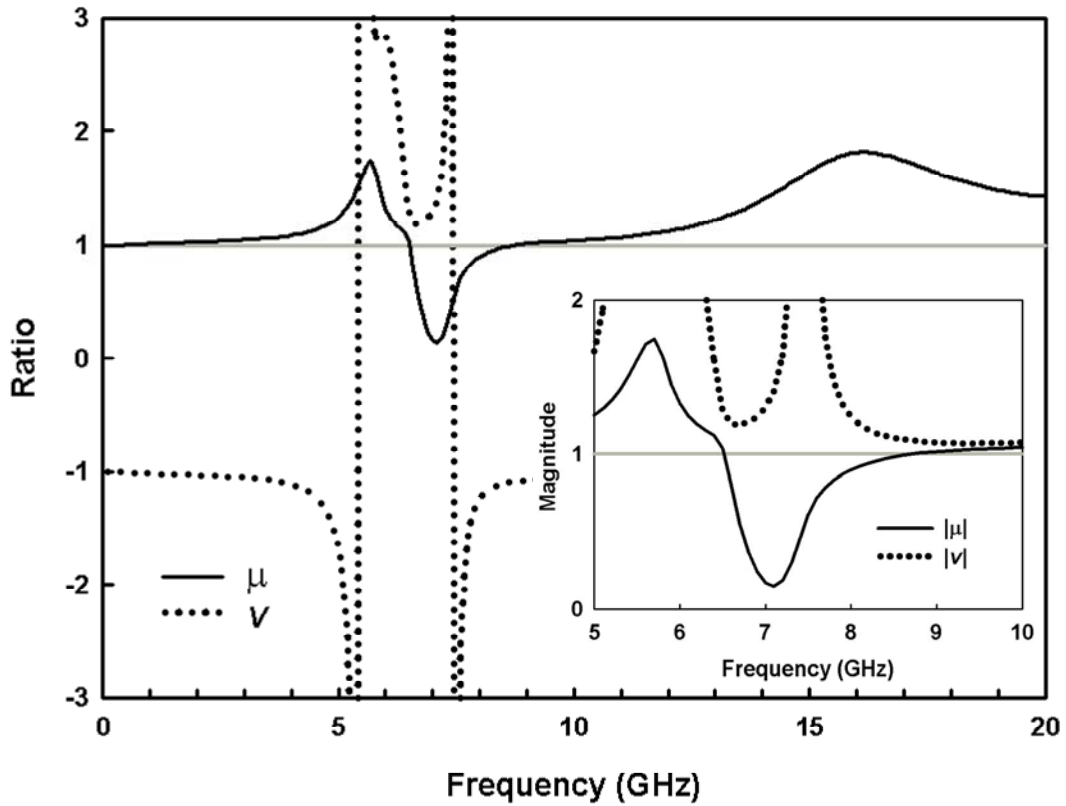
Frequency (GHz)	Condition		Stability	$50\Omega \in$ Stable Region
< 5.3	$\lvert\nu\rvert>\lvert\mu\rvert>1$	$\mu>0, \nu<0$	Unconditional	Yes
5.3 ~ 5.6	$\lvert\nu\rvert>\lvert\mu\rvert>1$	$\mu>0, \nu>0$	Unconditional	Yes
5.6 ~ 6.0	$\lvert\nu\rvert>1>\lvert\mu\rvert$	$\mu>0, \nu>0$	Conditional	Yes
6.0 ~ 6.5	$1>\lvert\nu\rvert>\lvert\mu\rvert$	$\mu>0, \nu>0$	Conditional	Yes
6.5~ 6.9	$1>\lvert\nu\rvert>\lvert\mu\rvert$	$\mu<0, \nu>0$	Conditional	No
6.9 ~ 7.9	$\lvert\nu\rvert>1>\lvert\mu\rvert$	$\mu<0, \nu>0$	Conditional	No
7.9 ~ 9.9	$\lvert\nu\rvert>1>\lvert\mu\rvert$	$\mu>0, \nu<0$	Conditional	Yes
> 9.9	$\lvert\nu\rvert>\lvert\mu\rvert>1$	$\mu>0, \nu<0$	Unconditional	Yes

Fig. 4.19 The μ and ν stability parameters against frequency from DC to 20 GHz of the prototype active bandpass filter when V_{tun} set at 1.2 volt.
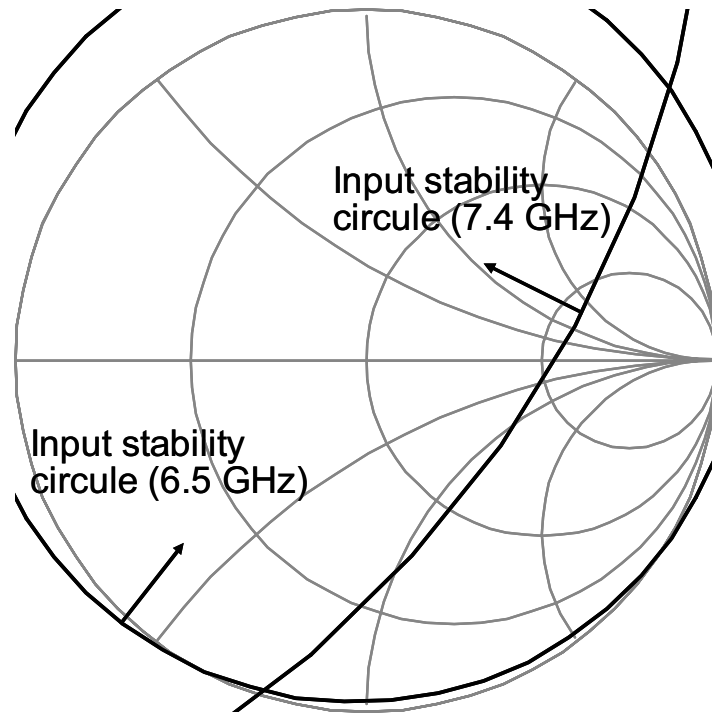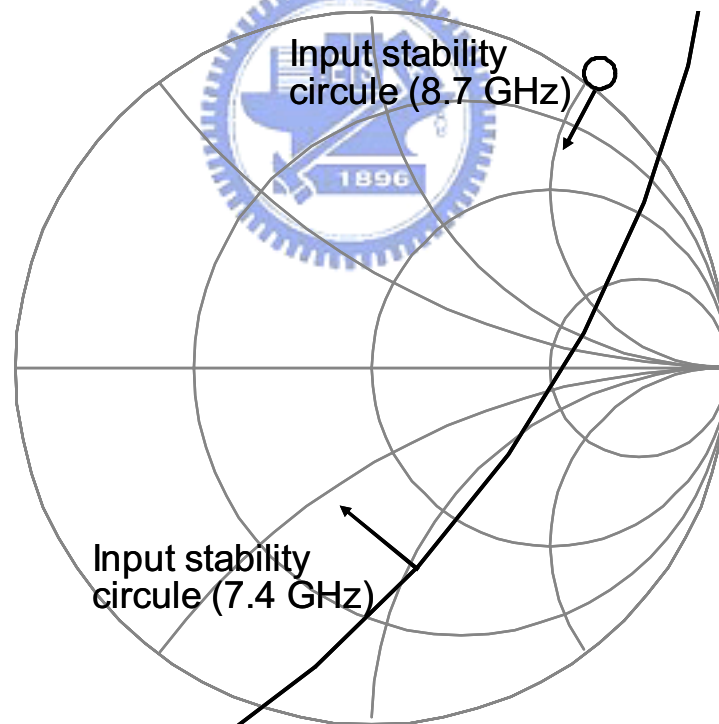
Fig 4.20 The input stability circles of the prototype active bandpass filter design with V_{tun} set at 1.0 volt. The stable region is indicated by the "→" sign. (a) 6.5 GHz and 7.4 GHz. (b) 7.4 GHz and 8.7 GHz.
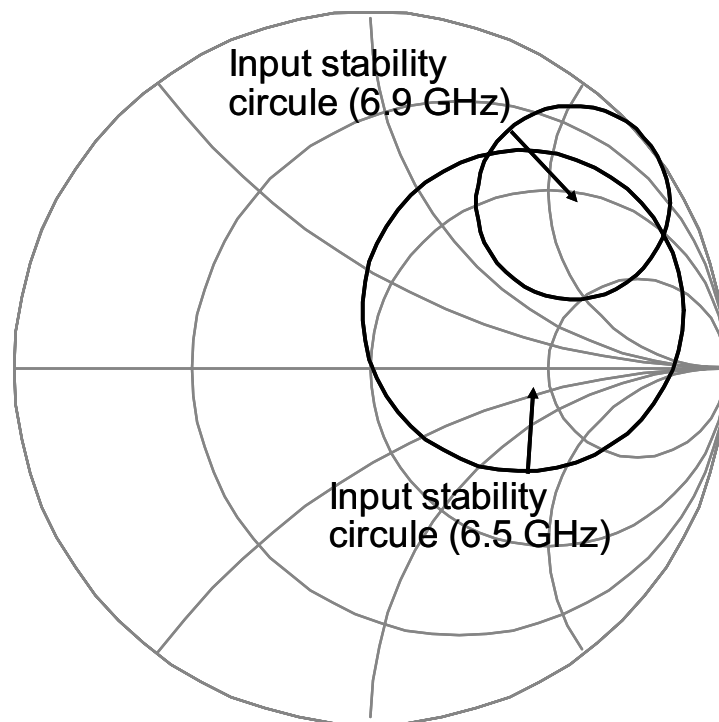
(a)
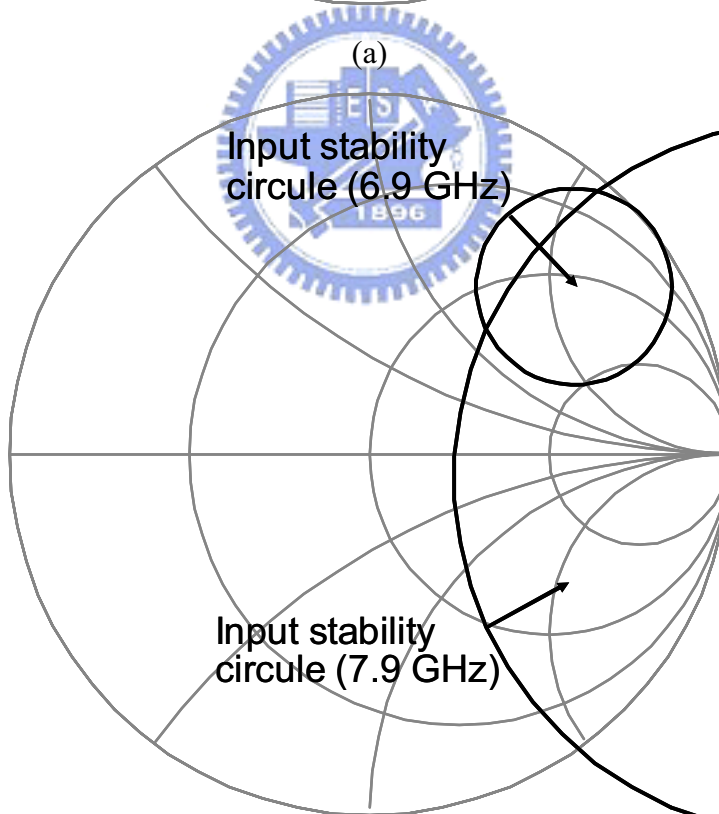
(b)

Fig. 4.21 The input stability circles of the prototype active bandpass filter design with V_{tun} set at 1.2 volt. The stable region is indicated by the "→" sign. (a) 6.5 GHz and 6.9 GHz. (b) 6.9 GHz and 7.9 GHz.

4.7 Figure of Merit

Literature survey on the normalized chip area ($\text{Area}_{\text{Norm}}$) of 25 published monolithic active filter designs in CMOS, SiGe, and GaAs technologies from 1 to 100 GHz is given in Fig. 4.22. Where $\text{Area}_{\text{Norm}}$ is the ratio between the chip area and the order of the active bandpass filter normalized to the square of the equivalent free-space wavelength $(\lambda_0)^2$ at the filter's center frequency. Apart from the process technology, the applied circuit technique is also classified to give a clear impression. As could be observed, active resonator of lumped LC element with negative resistance (–R) circuit is the mostly used techniques. As expect, the method of distributed transmission lines (TLs) with –R circuit demands the most normalized chip area. The proposed method applying meander CCS TLs with –R circuit in CMOS technology, however, occupies only four-thousandths of the counterpart in [56] applying CPW TL with –R circuitry in GaAs technology. Notably, the propose method achieves a similar level in $\text{Area}_{\text{Norm}}$ as those using the lumped LC element with –R circuit approach at C-Band.

Traditionally, the noise and linearity property of a receiver front end is limited by the performance of low noise amplifiers (LNA) and mixers. To make filtering function properly, the performance of an active filter should be reasonably comparable to those of the LNAs. For example, typical CMOS or SiGe monolithic LNAs designed for commercial applications across C-Band, like 802.11a and UWB, achieve a noise figure from 4.3 to 4.5 dB with P_{1dB} from -10 to -1.5 dBm, respectively [10, 59, 96-97]. Hence, in comparing circuit techniques of active bandpass filters, a figure-of-merit (FOM) similar to those in [96-97] is defined as

$$\text{FoM} = \frac{|S_{21}|[1] \times BW\,[\text{MHz}] \times P_{1dB}\,[\text{mW}]}{P_{DC}\,[\text{mW}] \times (NF-1)[1] \times \sqrt{\text{Area}_{\text{Norm}}}\,[1]} \qquad (8)$$

In addition to 3-dB bandwidth (BW), the transmission coefficient (S_{21}), the excess noise figure (NF-1), and the power consumption (P_{DC}), the input 1-dB compression point (P_{1dB}) and the square root of the normalized chip area ($\sqrt{\text{Area}_{\text{Norm}}}$) were included to evaluated an active bandpass filter aimed for small chip area, low noise, low power, low loss, and high linearity applications. Notably, the noise characteristic of an active filter is often quoted as the noise power spectrum density in the passband. To avoid confusion, these reported data are transformed to the equivalent input referred noise figure based on (6).

In Table 4.1, a set of representative designs from Fig. 4.22 are compared based on the FoM defined in (8). As could be observed, most CMOS lumped LC approaches have the inherent advantage of small chip area. But, their bandwidth, noise figure, and P_{1dB} characteristics are restricted as well. On the other hand, the same circuit techniques applied in GaAs technology, a minimum noise figure of 7.5 dB is reported in [53]. Though, its power consumption is relative large, but an excellent linearity of a +11-dBm input third-order intermodulation point (IIP_3) is achieved. Nevertheless, the proposed approach in this study achieves an active bandpass filter with a small chip area, low power consumption, modest noise figure, and modest P_{1dB} in CMOS technology for the first time. However, the noise and P_{1dB} characteristics of this prototype appear insufficient for commercial applications. It is expected that the required linearity and noise properties could be achieved by advances in device fabrication and circuit techniques.

1e-1

[56]

1e-2
[62]
[63]
[47]

1e-3
[66]
[38] [53]
[67] [65]
[23]

Area$_{Norm}$ $(\lambda_0)^2$

[48]

[18] [43]
[40] [7]

[51] [50] This Study

[39]

[21]
[24]
[19] [22]
[20]

GaAs   Gyrator
GaAs   Recursive
CMOS -R + CCS TL
GaAs   -R + CPW TL
CMOS -R + Lump
GaAs   -R + Lump
SiGe   -R + Lump
GaAs   Active Inductor

1e-4

1e-5

1e-6
1   10   100
Frequency (GHz)
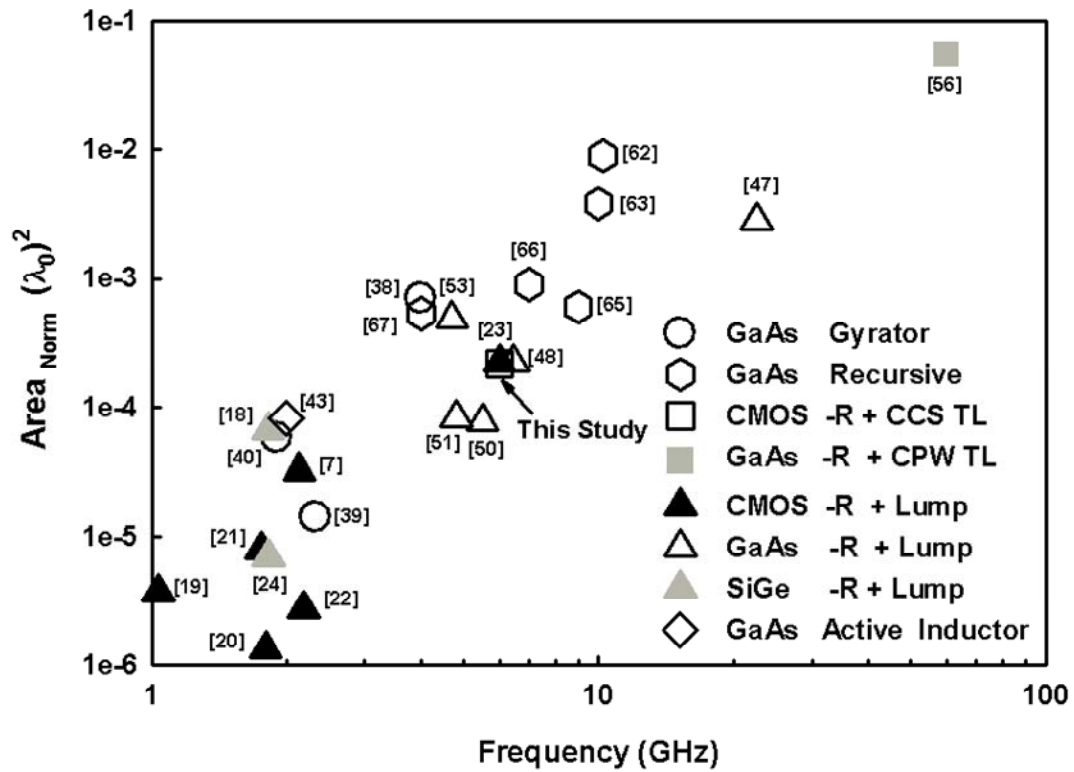
Fig. 4.22 A survey of 25 published works on monolithic active bandpass filter design from 1 to 100 GHz.

Table 4.1 A comparison of representative monolithic active filters in Fig. 4.22.

Design	[53]	[18]	[22]	[20]	[7]	[23]	This Study
Technology (μm)	GaAs 0.5	SiGe 0.5	CMOS 0.35	CMOS 0.5	CMOS 0.25	CMOS 0.18	CMOS 0.18
Order	2	4	2	4	3	4	2
f_0(GHz)	4.7	1.7	2.19	1.8	2.14	6.0	6.0
BW(MHz)	400	102	53.8	80	60	100	1140
S_{21}(dB)	0	0	-5	-15	0	0	-2.2
Return Loss(dB)	9	N.A.	N.A.	N.A.	12.0	N.A.	7.64
P_{1dB} (dBm)	1.4*	-6.9	-30	-21	-13.4	-27.5	-15.2
Area$_{Norm}$ $(\lambda_0)^2$	4.90E-4	6.58E-5	2.77E-6	1.35E-6	3.20E-5	2.25E-4	2.16E-4
P_{DC}(mW)	150	150.12	5.2	43.2	5	43.5	5.4
Output Noise (dBm/Hz)	N.A.	-141	N.A.	-180	-155	-150.5	N.A
NF(dB)	7.5	32.8	26.8	9.3	18.9	23.3	11.4
FOM	35.93	0.01	0.01	1.87	5.09	0.01	20.3

* approximated by P_{1dB} =IIP$_3$ -9.6dB

4.8 Discussion

This chapter has discussed the innovating approach of a 6.02 GHz second-order active bandpass filer utilizing Q-enhanced complementary-conducting-strips (CCS) half-wavelength resonators in a standard CMOS 0.18 μm technology. The loss compensation mechanism is valid only when the cross-coupled pair circuit is differentially operated. Accompanying even mode signals within the Q-enhanced half-wavelength resonator will be attenuated automatically. Through experimental results and theoretical analysis, the insertion loss of the proposed architecture could be independently controlled from the filter's center frequency, 3-dB bandwidth, reflection zeros, and outband rejections. The filter's stability had also been theoretically investigated. When the transmission gain was 0.56 dB, the active filter was free from oscillation. Regarding the noise property, both an equivalent noisy two-port network and an analytic expression are presented and give physical explanation of the noise contributions within the active filter. Comparing with other published works in GaAs, CMOS, and SiGe technologies, the realized design shows advantages in terms of small chip area, low power consumption, modest noise figure, and modest P_{1dB}. In addition, it is for the first time that CCS TL is used for realizing monolithic active bandpass filter at C-Band in CMOS technology. The insufficient noise and linearity characteristics need to be further improved for practical applications.

CHAPTER 5

Conclusion

In this dissertation the design and application of the meandered CMOS monolithic complementary-conducting-strips transmission line (CCS TL) have been presented which has made CCS-TLs based active filter at low microwave frequency range possible. Two innovating approaches adopting negative resistance circuits for realizations of C-Band active bandpass filters were experimentally and theoretically investigated. This chapter summarizes the contributions and recommendations for future researches.

5.1 Contributions

1. Three advantageous guiding properties of the meandered CCS TL compared to the meandered microstip have been theoretically demonstrated in standard CMOS technology. In addition, meandered CCS TL with unequal connecting arms (S) and central patch (W) has even better characteristics than the one with equal S and W also in the same perspective.

2. Various techniques of active inductor, active resonator, and negative resistance circuitry have been surveyed for suitability of realizations in standard CMOS technology.

3. Loss-free active CMOS meandered CCS TL from 1 to 5.5 GHz has been developed with an enhanced slow wave guiding property owing to the increase of unit-length capacitance introduced by Λ-type MOSFETs.

4. An active-filter architecture incorporating Q-enhanced half-wavelength CCS TL

resonator has been experimentally and theoretically investigated. The loss compensation mechanism is only activated when the phase difference across the composite half-wavelength resonator satisfies the requirement of the cross-coupled pair circuit for generating negative resistance.

5. Insertion loss of the proposed filter architecture could be controlled independent from other filer characteristics, such as 3-dB bandwidth, outband rejections, and center frequency. Good superiors-mode suppressions are also observed thanks to the loss compensation technique.

6. The noise contribution from the cross-coupled pair circuitry at the passband for the proposed active bandpass filter has been analyzed and useful formula has been given. Stability analyses for the proposed filter with transmission gain and insertion loss have also been carried out.

7. The required chip area is comparable to other monolithic active filers employed lump LC elements with negative resistance circuit at C-Band both in CMOS and GaAs technologies. Also, this is the fist time that the meandered CCS TL has been applied in monolithic CMOS active bandpass filter design at C-Band.

5.2 Future Researches

The nonlinearity introduced by the cross-coupled pair circuit and its effect on the prototype active bandpass filter is not covered in this dissertation. An investigation at these effects may help to lower the distortion of the proposed filer. Development of Q-enhanced CCS TL based resonators of low resonance frequencies may extend the application of the proposed filter architecture at even lower microwave frequencies. Furthermore, design optimization for insertion loss and noise characteristic by employing high-Q passive CCS TLs can be investigated in order to produce low noise

and low insertion loss filter characteristics. Finally, application of the proposed filter architecture to radio receivers or transmitters is the ultimate goal of this dissertation.

REFERENCE

[1] C.-H. Lee, A. Sutono, S. Han, K. Lim, S. Pinel, E. M. Tentzeris, and J. Laskar, "A compact LTCC-based Ku-band transmitter module," *IEEE Trans. Adv. Packag.*, vol. 25, no. 3, pp. 374–384, Aug. 2002.

[2] J. Ryckaert, S. Brebels, B. Come, W. Diels, D. Hauspie, S. Stoukatch, K. Vaesen, W. De Raedt, and S. Donnay, "Single-package 5 GHz WLAN RF module with embedded patch antenna and 20 dBm power amplifier," *IEEE MTT-S Int. Microwave Symp. Dig.*, pp. 1037–1040, 2003.

[3] Y.-S. Lin, C.-C. Liu, K.-M. Li, and C. H. Chen, "Design of an LTCC tri-band transceiver module for GPRS mobile applications," *IEEE Trans. Microw. Theory Tech.*, vol. 52, no. 12, pp. 2718–2724, Dec. 2004.

[4] M. M. Tentzeris, J. Laskar, J. Papapolymerou, S. Pinel, V. Palazzari, R. Li, G. Dejean, N. Papageorgiou, D. Thompson, R. Bairavasubramanian, S. Sarkar, and J.-H. Lee, "3-D-integrated RF and millimeter-wave functions and modules using liquid crystal polymer (LCP) system-on-package technology," *IEEE Trans. Adv. Packag.*, vol.27, no. 2, pp. 332–340, May 2004.

[5] A. Chernyakov, K. Markov, D. Orlenko, P. Heide, and C. Ruppel, "Miniature fully-integrated WLAN frontend-modules based on LTCC technology," in *IEEE MTT-S Int. Microwave Symp. Dig.*, 2004, pp.139–142.

[6] A. C. W. Lu, K. M. Chua, L. L. Wai, S. C. K. Wong, J. J. Wang, and Y.P. Zhang, "Integrated antenna module for broad-band wireless applications," in *Electronics Packaging Tech. Conf.*, 2004, pp. 240–243.

[7] Theerachet Soorapanth and S. Simon Wong, "A 0-dB IL 2140±30MHz bandpass filter utilizing Q-enhanced spiral inductors in standard CMOS," *IEEE J. Solid-State Circuits,* vol. 37, pp. 579-586, May 2002.

[8] Xin He and William B. Kuhn, "A 2.5-GHz low-power, high dynamic range, self-tuned Q-enhanced LC filter in SOI," *IEEE J. Solid-State Circuits,* vol. 40, no. 8, pp. 1618-1628, Aug. 2005.

[9] Aparin V., Gazzerro P., Jianjun Zhou, Bo Sun, Szabo S., Zeisel E., Segoria T., Ciccarelli S., Persico C., Narathong C., Sridhara R., "A highly-integrated tri-band/quad-mode SiGe BiCMOS RF-to-baseband receiver for wireless CDMA/WCDMA/AMPS applications with GPS capability," in *IEEE Int. Solid-State Circuits Conf. (ISSCC)*, San Francisco, Feb. 2002, pp. 234-235.

[10] Thomas H. Lee, Hirad Samavati, and Hamid R. Rategh, "5-GHz CMOS wireless lans," *IEEE J. Solid-State Circuits,* vol. 50, no. 1, pp. 123-127, Jan. 2002.

[11] Stroet P. M., Mohindra R., Hahn S., Schuur A., and Riou E., "A zero-IF single-chip transceiver for up to 22 Mb/s QPSK 802.11b wireless LAN," in *IEEE Int. Solid-State Circuits Conf. (ISSCC)*, San Francisco, Feb. 2001, pp. 204-205.

[12] Kluge W., Dathe L., Jaehne R., Ehrenreich S., and Eggert D., "A 2.4GHz CMOS transceiver for 802.11b wireless LANs," in *IEEE Int. Solid-State Circuits Conf. (ISSCC)*, San Francisco, Feb. 2003, pp. 360-361.

[13] Duvivier E., Cipriani S., Carpineto L., Cusinato P., Bisanti B., Galant F., Chalet F., Coppola F., Cercelaru S., Puccio G., Mouralis N., and Jiguet J. C., "A fully integrated zero-IF transceiver for GSM-GPRS quad band application," in *IEEE Int. Solid-State Circuits Conf. (ISSCC)*, San Francisco, Feb. 2003, pp. 274-275.

[14] Filiol N., Birkett N., Cherry J., Balteanu F., Gojocaru C., Namdar A., Pamir T., Sheikh K., Glandon G., Payer D., Swaminathan A., Forbes R., Riley T., Alinoor S. M., Macrobbie E., Cloutier M., Pipilos S., and Varelas T, "A 22 mW Bluetooth RF transceiver with direct RF modulation and on-chip IF filtering," in *IEEE Int. Solid-State Circuits Conf. (ISSCC)*, San Francisco, Feb. 2001, pp. 202-203.

[15] Tadjpour S., Cijvat E., Hegazi E., and Abidi A., "A 900 MHz dual conversion low-IF GSM receiver in 0.35 μm CMOS," in *IEEE Int. Solid-State Circuits Conf. (ISSCC)*, San Francisco, Feb. 2001, pp. 292-293.

[16] Leeuwenburgh A. J., Laak J. W. F., Mulders A. G., Hoogstraate A. J., van Laarhoven P. J. M., Nijrolder M., Prummel J. G., Kamp P. J. M., "A 1.9GHz fully integrated CMOS DECT transceiver," in *IEEE Int. Solid-State Circuits Conf. (ISSCC)*, San Francisco, Feb. 2003, pp. 450-452.

[17] Cojocaru C., Pamir T., Balteanu F., Namdar A., Payer D., Gheorghe I., Lipan T., Sheikh K., Pingot J., Paananen H., Littow M., Cloutier M., MacRobbie E., "A 43mW Bluetooth transceiver with -91dBm sensitivity," in *IEEE Int. Solid-State Circuits Conf. (ISSCC)*, San Francisco, Feb. 2003, pp. 90-91.

[18] Dandan Li and Yannis Tsividis, "Design techniques for Automatically tuned integrated gigahertz-range active LC filters," *IEEE J. Solid-State Circuits,* vol. 37, no. 8, pp. 967-977, Aug. 2002.

[19] Sotiris Bantas and Yorgos Koutsoyannopoulos, "CMOS active-LC bandpass filters with coupled-inductor Q-enhancement and center frequency tuning," *IEEE Trans. Circuits Syst. II*, vol.51, pp.69-76, Feb. 2004.

[20] Ahmed Nader Mohieldin, Edgar Sanchez-Sinencio, and Jose Silva-Martinez, "A 2.7-V 1.8-GHz fourth-order tunable LC bandpass filter based on emulation of magnetically coupled resonators," *IEEE J. Solid-State Circuits,* vol. 38, pp. 1172-1181, Jul. 2003.

[21] Yi-Cheng Wu and M. Frank Chang, "On-chip RF spiral inductors and bandpass filters using active magnetic energy recovery," in *Proc. IEEE Custom Integrated Circuits Conf.*, Orlando, May 2002, pp. 275-278.

[22] Fikert Dulger, Edgar Sanchez-Sinencio, and Jose Silva-Martinez, "A 1.3-V 5-mW fully integrated tunable bandpass filter at 2.1 GHz in 0.35um CMOS," *IEEE J. Solid-State Circuits,* vol. 38, pp. 918-928, Jun. 2003.

[23] Shaorui Li, Nebojsa Stanic, Krishnamurthy Soumyanath, and Yannis Tsividis, "An Integrated 1.5 V 6 GHz *Q*-Enhanced LC CMOS Filter with Automatic Quality Factor Tuning Using Conductance Reference," *2005 IEEE Int. Radio Frequency Integrated Circuits Symp. Dig.*, pp. 621-624, July 2005.

[24] S. Pipilos, Y. P. Tsividis, J. Fenk, and Y. Papananos, " A Si 1.8 GHz RLC filter with tunable center frequency and quality factor," *IEEE J. Solid-State Circuits,* vol. 31, no. 10, pp. 1517-1525, Oct. 1996.

[25] Chinh H. Doan, Sohrab Emami, Ali M. Niknejad, and Robert W. Brodersen, "Design of CMOS for 60GHz Applications," in *IEEE Int. Solid-State Circuits Conf. (ISSCC)*, San Francisco, Feb. 2004, pp. 440-441.

[26] Hung-Ta Tso and Chien-Nan Kuo, "40GHz miniature bandpass filter design in standard CMOS process," in *Topical Meeting on Silicon Monolithic Integrated Circuits in RF Systems*, Atlanta, Sep. 2004, pp. 239-242.

[27] Kamran Entesari, Tauno Vaha-Heikkila, and Gabriel M. Rebeiz, "Miniaturized differential filters for C- and Ku-band applications," in *Proc. Eur. Microwave Conf.*, Munich, Germany, 2003, pp. 227-230.

[28] C.-C. Chen and Ching-Kuang C. Tzuang, "Synthetic quasi-TEM meandered transmission lines for compacted microwave integrated circuits," *IEEE Trans. Microw. Theory Tech.*, vol. 52, no. 6, pp. 1637–1647, Jun. 2004.

[29] Ching-Kuang C. Tzuang, Hsien-Hung Wu, Hsien-Shun Wu, and Johnsea Chen, "A CMOS miniaturized C-Band active bandpass filter," in *IEEE MTT-S Int. Microwave symp. Dig.*, San Francisco, Jun. 2006, pp. 772-775.

[30] Ching-Kuang C. Tzuang, Hsien-Hung Wu, Hsien-Shun Wu, and Johnsea Chen, "CMOS active bandpass filter using compacted synthetic quasi-tem lines at C-band," to be appeared in *IEEE Trans. Microw. Theory Tech.*, Sep. 2006.

[31] W. R. Eisenstadt and Y. Eo, "S-parameter-Based IC interconnect transmission line characterization," *IEEE Trans. On Components, Hybrids, and Manufacturing Tech.*, vol. 15, pp. 483-490, Aug. 1992.

[32] Hsien-Shun Wu, Houng-Jay Yang, Ching-Juang Peng, and Ching-Kuang Tzuang, "Miniaturized microwave passive filter incorporating multilayer synthetic quasi-TEM transmission line," *IEEE Trans. Microw. Theory Tech.*, vol.53, no. 9, pp. 2317-2720, Sep. 2005.

[33] H. J. Orchard, "Inductorless filter," *Electron Letters,* vol. 2, pp. 224-225, Jun. 1966.

[34] H. J. Orchard and Desmond F. Sheahan, "Inductorless bandpass filter," *IEEE J. Solid-State Circuits,* vol. sc-5, no. 3, pp. 108-118, Jun. 1970.

[35] J. O. Voorman, W.H. A. Bruls, and P. J. Barth, "Integration of analog filters in a bipolar process," *IEEE J. Solid-State Circuits,* vol. sc-17, no. 4, pp. 713-722, Aug. 1982.

[36] Yun-Ti Wang and AsAd A. Abidi, "CMOS active filter design at very high frequencies," *IEEE J. Solid-State Circuits,* vol. 25, no. 6, pp. 1562-1573, Dec. 1990.

[37] Bram Nauta, Analog CMOS filters for very high frequencies. MA: Kluwer Academic Publishers, 1993, ch. 3.

[38] S. P. Marsh and R. G. Arnold, "MMIC gyrator bandstop filter with ultra-wideband tuning," in *Gallium Arsenide Integrated Circuit (GaAs IC) Symp. Dig.*, 1994, pp. 39-40.

[39] R. Kaunisto, P. Alinikula, K. Stadius, and V. Porra, "A low-power HBT MMIC filter based on tunable active inductor," *IEEE Microwave Wireless Compon. Lett.*, vol. 7, no. 8, pp. 209-211, Aug. 1997.

[40] F. Giannini, E. Limiti, G. Orengo, and P. Sanzi, "High-Q gyrator-based monolithic active tunable bandstpop filter," in *IEEE MTT-S Int. Microwave Symp. Dig.*, 1997, pp. 809-812.

[41] Shinji Hara, Tsuneo Tokumitsu, Toshiaki Tanaka, and Masayoshi Aikawa, "Broad-band monolithic microwave active inductor and its applications to miniaturized wind-band amplifiers," *IEEE Trans. Microwave Theory Tech.*, vol. 36, no. 12, pp. 1920-1924, Dec. 1988.

[42] Shinji Hara, Tsuneo Tokumitsu, and Masayoshi Aikawa, "Lossless broad-band monolithic microwave active inductor," in *IEEE MTT-S Int. Microwave Symp. Dig.*, 1989, pp. 955-958.

[43] Stepan Lucyszyn and Ian D. Robertson, "Monolithic narrow-band filter using ultrahigh-Q tunable active inductor," *IEEE Trans. Microwave Theory Tech.*, vol. 42, no. 12, pp. 2617-2622, Dec. 1994.

[44] Stepan Lucyszyn and Ian D. Robertson, "High performance MMIC narrow band filter using tunable active inductor," in *IEEE MTT-S Int. Microwave Symp. Dig.*, 1994, pp. 91-93.

[45] E. M. Bastida, G. P. Donzelli, and L. Scopelliti, "GaAs monolithic microwave integrated circuits using broadband tunable active inductors," in *Proc. 19th European Microwave Conf.*, Sept. 1989, pp. 1282-1287.

[46] Jin-Su Ko and Kwyro Lee, "Low power tunable active inductor and its applications to monolithic VCO and BPF," in *IEEE MTT-S Int. Microwave Symp. Dig.*, 1997, pp. 929-932.

[47] Kang-Wei Fan, Ching-Chih Weng, Zou-Min Tsai, Huei Wang, and Shyh-Kang Jeng, "K-band MMIC active band-pass filter," *IEEE Microwave Wireless Compon. Lett.*, vol. 15, no. 1, pp. 19-21, Jan. 2005.

[48] K. W. Kobayashi, L. T. Tran, D. K. Umemoto, A. K. Oki, and D. C. Streit, "A 6.45 GHz active bandpass filter using HBT negative resistance elements," in *Gallium Arsenide Integrated Circuit (GaAs IC) Symp. Dig.*, Nov. 1998, pp. 143-146.

[49] Bernd P. Hopf, Ingo Wolff, and Marco Gugiielmi, "Coplanar MMIC active bandpass filters using negative resistance circuits," in *IEEE MTT-S Int. Microwave Symp. Dig.*, 1994, pp. 1183-1185.

[50] Bernd P. Hopf, Ingo Wolff, and Marco Gugiielmi, "Coplanar MMIC active bandpass filters using negative resistance circuits," *IEEE Trans. Microwave Theory Tech.*, vol. 42, no. 12, pp. 2598-2602, Dec. 1994.

[51] Yonh-Ho Cho, Song-Cheol Hong, and Young-Se Kwon, "A low-power monolithic GaAs FET bandpass filter based on negative resistance technique," *IEEE Microwave Guided Wave lett.*, vol. 8, no. 4, pp. 161-163, Apr. 1998.

[52] Ulun Karacaoglu and Ian D. Robertson, "MMIC active bandpass filters using negative resistance elements," in *IEEE Microwave and Millimeter-Wave Monolithic Circuit (MMWMC) Symp. Dig.*, 1995, pp. 171-174.

[53] Ulun Karacaoglu and Ian D. Robertson, "MMIC active bandpass filters using varactor-tuned negative resistance elements," *IEEE Trans. Microwave Theory Tech.*, vol. 43, no. 12, pp. 2926-2932, Dec. 1995.

[54] M. R. Moazzam, I. D. Robertson, A. H. Aghvami, and Marco Gugiielmi, "S-band monolithic active filter using actively-coupled resonator techniques," in *Proc. 22nd European Microwave Conf.*, Aug. 1992, pp. 729-734.

[55] Chi-Yang Chang and Tatsuo Itoh, "Microwave active filters based on coupled negative resistance method," *IEEE Trans. Microwave Theory & Tech.,* vol. 38, no. 12, pp. 1879-1884, Dec. 1990.

[56] Masaharu Ito, Kenichi Maruhashi, Shuya Kishimoto, and Keiichi Ohata, "60-GHz-Band Coplanar MMIC Active Filter," *IEEE Trans. Microwave Theory & Tech.,* vol. 52, no. 3, pp. 743-750, March 2004.

[57] Ulun Karacaoglu, Ian D. Robertson, and M. Guglielmi, "A dual-mode microstrip ring resonator filter with active devices for loss compensation," in *IEEE MTT-S Int. Microwave Symp. Dig.*, 1993, pp. 189-192.

[58] Ulun Karacaoglu, Ian D. Robertson, and M. Guglielmi, "Microstrip bandpass filters using MMIC negative resistance circuits for loss compensation," in *IEEE MTT-S Int. Microwave Symp. Dig.*, 1994, pp. 613-616.

[59] R. R. Bonetti, A. E. Williams, T. Duong, R. Gupta, and R. Mott, "An MMIC active filter with 60-dB rejection," in *IEEE MTT-S Int. Microwave Symp. Dig.*, Jun. 1992, pp. 1195-1198.

[60] Nhat M. Nguyen and Robert G. Meyer, "A Si bipolar monolithic RF bandpass amplifier," *IEEE J. Solid-State Circuits,* vol. 27, no. 1, pp. 123-127, Jan. 1992.

[61] Hossein Hashemi and Ali Hajimiri, "Cocurrent multiband low-nose amplifiers-theory, design, and applications" *IEEE Trans. Microwave Theory Tech.*, vol. 50, no. 1, pp. 288-301, Jan. 2002.

[62] Manfred J. Schindler and Yusuke Tajima, "A novel MMIC active filter with lumped and transversal," *IEEE Trans. Microwave Theory Tech.*, vol. 37, no. 12, pp. 2148-2153, Dec. 1989.

[63] M. Danestig, H. Johansson, A. Ouaha, and S. Rudner, "Low-noise active recursive MMIC filters," in *IEEE MTT-S Int. Microwave Symp. Dig.*, Denver, CO, Jun. 1997, pp. 705-708.

[64] H. Ezzedine, M. Delmond, L. Billonnet, B. Jarry, and P. Guillon, "Optimization of noise performance for various topologies of microwave active recursive filters," in *IEEE MTT-S Int. Microwave Symp. Dig.*, 1998, pp. 1173-1176.

[65] M. Delmond and L. Billonnet, "Microwave tunable active filter design in MMIC technology using recursive concepts," in *IEEE Microwave and Millimeter-Wave Monolithic Circuit (MMWMC) Symp. Dig.*, 1995, pp. 105-108.

[66] W. Mouzannar, L. Billonnet, B. Jarry, and P. Guillon, "Highly selective novel MMIC microwave active recursive filter," in *IEEE Radio Frequency Integrated Circuit (RFIC) Symp. Dig.*, 1998, pp. 39-42.

[67] A. Cenac, H. Ezzedine, L. Billonnet, B. Jarry, and P. Guillon, "Low noise and frequency tunable microwave active recursive filters using power summation principles," in *IEEE MTT-S Int. Microwave Symp. Dig.*, 1999, pp. 1227-1230.

[68] D. K. Asams and R. Y. C. Ho, "Active filters for UHF and microwave frequencies," *IEEE Trans. Microwave Theory Tech.*, vol. MTT-17, pp. 662-670, Sep. 1969.

[69] C. R. Poole, "The effect of device configuration on GaAs MESFET negative resistance behavior," in *Int. Circuit and System Conf.*, Shenzhen, China, Jun. 1991, pp. 427-430.

[70] Jae-Ryong Lee, Young-Hoon Chun, and Sang-Won Yun, "A novel bandpass filter using active capacitance," in *IEEE MTT-S Int. Microwave Symp. Dig.*, 2003, pp. 1747-1750.

[71] Young-Hoon Chun, Jae-Ryong Lee, Sang-Won Yun, and Jin-Koo Rhee, "Design of an RF low-noise bandpass filter using active capacitance circuit," *IEEE Trans. Microwave Theory Tech.*, vol. 53, no. 2, pp. 687-694, Feb. 2005.

[72] Ching-Yuang. Wu and Khun-Nan Lai, "Integrated Lambda differential negative resistance MOSFET device," *IEEE J. Solid-State Circuits,* vol. 14, no. 6, pp. 1094-1101, Dec. 1979.

[73] Behzad Razavi, *RF Microelectronics*. NJ: Prentice-Hall, 1998, pp. 228.

[74] George L. Matthaei, Leo Young, and E.M.T. Jones, *Microwave Filters, Impedance Matching Networks, and Coupling Structures*, MA: Artech House, 1980, ch. 8.

[75] George D. Vendelin, Anthony M. Pavio, and Ulrich L. Rohde, *Microwave Circuit Design using Linear and Nonlinear Techniques*. New York: Wiley, 1990, pp. 103.

[76] Paul A. Layman, and Savvas G. Chamberlain, "A compact thermal noise model for the investigation of soft error rates in MOS VLSI digital circuits," *IEEE J. Solid-State Circuits*, vol. 24, pp. 79-89, Feb. 1989.

[77] Emad Hegazi, Henrik Sjoland, and Asad A. Abidi, "A filtering technique to lower LC oscillator phase noise," *IEEE J. Solid-State Circuits*, vol. 36, no. 12, pp. 1921-1929, Feb. 2001.

[78] Derek K. Shaeffer and Thomas H. Lee, *The Design and Implementation of Low-Power CMOS Radio Receivers*. MA: Kluwer Academic Publishers, 1999, pp.52-53.

[79] Behzad Razavi, *Design of Analog CMOS Integrated Circuits*. New York: McGraw-Hill, 2001, pp. 212-213.

[80] Guillermo Gonzalez, *Microwave Transistor Amplifiers: Analysis and Design*. 2nd ed., NJ: Prentice-Hall, 1997, ch. 4.

[81] Yuhua Cheng and Chenming Hu, *Mosfet Modeling & Bsim3 User's Guide*. MA: Kluwer Academic Publishers, 1999, ch. 10.

[82] F. B. Lewellyn, "Some fundamental properties of transmission systems," *Proc. IRE*, vol. 40, no. 3, pp. 271-283, Mar. 1952.

[83] J. M. Rollet, "Stability and power gain invariants of linear two ports," *IRE Trans. Circuit Theory*, vol. CT-9, no. 3, pp. 29-32, Mar. 1962.

[84] Robert W. Jackson, "Rollet Proviso in the stability of linear microwave circuits-a tutorial," *IEEE Trans. Microwave Theory Tech.*, vol. 54, no. 3, pp. 993-1000, Mar. 2006.

[85] M. Ohtomo, "Proviso on the unconditional stability criteria for linear two ports," *IEEE Trans. Microwave Theory Tech.*, vol. 43, no. 5, pp. 1197-1200, Mar. 1995.

[86] Marion Lee Edwards and Jeffery H. Sinsky, "A new criterion for linear 2-port stability using a single geometrically derived parameter," *IEEE Trans. Microwave Theory Tech.*, vol. 40, no. 12, pp. 2303-2311, Dec. 1992.

[87] Marion Lee Edwards and Jeffery H. Sinsky, "New simple proofs of the two-port stability criterion in terms of the single stability parameter μ," *IEEE Trans. Microwave Theory Tech.*, vol. 49, no. 6, pp. 1073-1076, Jun. 2001.

[88] K. Kurokawa, *An Introduction to the Theory of Microwave Circuits*. New York: Academic, 1969.

[89] Guillermo Gonzalez, *Microwave Transistor Amplifiers: Analysis and Design*. 2nd ed., NJ: Prentice Hall, 1997, pp.217-227.

[90] Giancarlo Lombardi and Bruno Neri, "Criteria for the evaluation of unconditional stability of microwave linear two-ports: a critical review and new proof," *IEEE Trans. Microwave Theory Tech.*, vol. 47, no. 6, pp. 746–751, Jun. 1999.

[91] D. Woods, "Reappraisal of unconditional stability criteria for active 2-port networks in terms of S-parameters," *IEEE Trans. Circuit Syst.*, vol. CAS-23, no. 2, pp. 281-283, Feb. 1976.

[92] A. Platzker, W. Struble, and K. T. Hetzler, "Instabilities diagnosis and the role of K in microwave circuits," in *IEEE MTT-S Int. Microwave Symp. Dig.*, Jun. 1993, pp. 1185-1189.

[93] Robert W. Jackson, "Criteria for the onset of oscillation in microwave circuits," *IEEE Trans. Microwave Theory Tech.*, vol. 40, no. 3, pp. 566-569, Mar. 1992.

[94] Robert W. Jackson, "Comments for the onset of oscillation in microwave circuits," *IEEE Trans. Microwave Theory Tech.*, vol. 40, no. 9, pp. 1850-1851, Sep. 1992.

[95] C. C. Meng and H. Y. Ni, "Determining stability circle using two geometrically derived parameters," in *Asia-Pacific Microwave Conf.*, Dec. 2000, pp. 1101-1104.

[96] Frank Ellinger, David Barras, Martin Schmatz, and Heinz Jackel, "A low power DC-7.8 GHz BiCMOS LNA for UWB and optical communication," in *IEEE MTT-S Int. Microwave Symp. Dig.*, 2004, pp. 13-16.

[97] David Barras, Frank Ellinger, Heinz Jackel, and Walter Hirt, "A low supply voltage SiGe LNA for ultra-wideband frontends," *IEEE Microwave Wireless Compon. Lett.*, vol. 14, no. 10, pp. 469-471, Oct. 2004.

博士候選人資料

姓　名 ： 吳憲宏

性　別 ： 男

出生年月日 ： 民國 64 年 11 月 4 日

籍　貫 ： 江西省萍鄉縣

學　歷 ：

國立交通大學電子工程系畢業（82 年 9 月~86 年 7 月）

國立交通大學電子研究所畢業（86 年 9 月~88 年 7 月）

國立交通大學電信研究所博士班（92 年 9 月~95 年 7 月）

經　歷 ：

工業技術研究院系統晶片科技中心（88 年 10 月~92 年 8 月）

論文題目 ：

單晶互補式金屬導線傳輸線 CMOS 主動濾波器設計

Complementary-Conducting-Strips Transmission Line CMOS

Active Filter Design

Publication List

Journal Paper

1. Ching-Kuang C. Tzuang, <u>Hsien-Hung Wu</u>, Hsien-Shun Wu, and Johnsea Chen, "CMOS active bandpass filter using compacted synthetic quasi-TEM lines at C-Bnad," *IEEE Transactions on Microwave Theory and Techniques*, accepted and to be appeared in Sep. 2006.

Conference Paper

1. <u>Hsien-Shun Wu</u>, Hsien-Hung Wu, Ching-Kuang C. Tzuang, and Ta-Sung Lee, "Transmission Line Based CMOS RF SOC from Microwave to Millimeter-Wave," *Proc. Of the CDC2004 - 2004 Communication Design Conference*, San Francisco, CA, March 29-April 1, 2004.

2. <u>Hsien-Hung Wu</u>, Hsien-Shun Wu, and Ching-Kuang C. Tzuang, "Synthesized high-impedance CMOS thin-film transmission line," *Topical Meeting on Silicon Monolithic Integrated Circuits in RF Systems*, Atlanta, 2004, pp. 302-304.

3. Ching-Kuang C. Tzuang, <u>Hsien-Hung Wu</u>, Hsien-Shun Wu, and Johnsea Chen, "A CMOS miniaturized C-Band active bandpass filter," *IEEE MTT-S Int. Microwave symp. Dig.*, San Francisco, Jun. 2006, pp. 772-775.

4. <u>Hsien-Hung Wu</u> and Ching-Kuang C. Tzuang, "Ground-signal-ground guiding phenomena of noise coupling in CMOS substrate," *accepted by Topical Meeting on Silicon Monolithic Integrated Circuits in RF Systems2007*.

Pattern
    莊晴光、<u>吳憲宏</u>，主動式帶通濾波器，中華民國專利申請中。